2019

INTEGRATED COMPUTATIONAL MATERIALS ENGINEERING (ICME) INVESTIGATION OF ELECTRICAL CONDUCTIVITY AND THERMODYNAMIC STABILITY FOR PRECIPITATION STRENGTHENED Al-Zn-Zr AND Al-Zn-Ni TERNARY ALLOYS

Oladeji Fadayomi
Michigan Technological University, otfadayo@mtu.edu

INTEGRATED COMPUTATIONAL MATERIALS ENGINEERING (ICME) INVESTIGATION OF ELECTRICAL CONDUCTIVITY AND THERMODYNAMIC STABILITY FOR PRECIPITATION STRENGTHENED Al-Zn-Zr AND Al-Zn-Ni TERNARY ALLOYS

By

Oladeji Fadayomi

A DISSERTATION

Submitted in partial fulfillment of the requirements for the degree of

DOCTOR OF PHILOSOPHY

In Materials Science and Engineering

MICHIGAN TECHNOLOGICAL UNIVERSITY

2019

This dissertation has been approved in partial fulfillment of the requirements for the Degree of DOCTOR OF PHILOSOPHY in Materials Science and Engineering.

Department of Materials Science and Engineering

Dissertation Co-Advisor: *Gregory M. Odegard*

Dissertation Co-Advisor: *Paul G. Sanders*

Committee Member: *Stephen Hackney*

Committee Member: *S. Gowtham*

Department Chair: *Stephen Kampe*

Contents

Preface

This dissertation includes two chapters from my publication drafts. Chapter 4 has been accepted for publication at the Materials Science and Engineering: A journal (https://doi.org/10.1016/j.msea.2018.11.111), while chapter 5 is yet to be submitted to the Journal of Alloys and Compounds.

In terms of contributions to this work, Professor Gregory Odegard was very helpful with getting me up to speed with density functional theory simulation included in chapter 4. He also gave me useful information that helped make my simulations data more accurate. Many useful recommendations for additional analysis and literature reviews were also given by Prof. Paul Sanders. Denise, Rachel and Violet are credited with the initial heat treatment of Al-Zn-Zr alloy. Prof. Hackney, Pinaki and Prof. Milligan assisted with transmission electron microscopy and scanning electron microscopy images, diffraction patterns and energy dispersive x-ray spectroscopy included in chapter 4 and 5. All other data in this study was collected and analyzed by the author.

Acknowledgements

Most importantly, I will like to thank God Almighty for his many intervention, favor, mercy, guidance, love and compassion. I will not be where I am today without Him.

This work would not have been possible without the financial, moral and technical support from the following agencies, faculties, staff, graduate students, family and friends.

NSF I/UCRC on Novel High Voltage/Temperature Materials and Structures (Grant IIP-1362040)

General Cable Corporation

SUPERIOR, a high-performance computing cluster at Michigan Technological University

S/TEM – NSF MRI fund (Grant #1429232)

Prof. Gregory Odegard, Prof. Paul Sanders, Prof. Stephen Hackney, Prof. S. Gowtham, Prof. Walt Milligan, Dr. Pinaki, Dr. Joe Licavoli and Dr. Dan Seguin

Tom Wood, Owen Mills, Jerry, Paul Fraley, Shenjia, CJ

Denise, Rachel, Violet, Akhila, Prasad, Ninad, Olumide Winjobi, Kyle Deane

Dad, Mum, siblings (Dele, Foluso, and Tosin Fadayomi), Ayotunde Fadayomi, Leke Adegbulugbe, Uncles and Aunts (Kola, Biodun and Oye Fadayomi, Lemmy Akintomide and Jumoke Bademosi), Onyeka Emili and family

Special thanks to my twin Kehinde Fadayomi

Edgar Kosgey, Lukmon Aminu, Ope Fatokun, LJ, Harry Orih, Wole Adebiyi, Jesse Balami, Dr. Tajuan Wilson, Ekong, Azih Onyeka, Oziegbe

Finally, Mr. Charles Anyansi, you have been heaven sent and I will never forget your act of kindness toward me. Continue to rest in peace (RIP) sir.

Abstract

High electrical conductivity Al-Zn-TM (TM=Transition metals) alloys with improved mechanical properties and thermal resistance are developed with an integrated computational material engineering (ICME) strategy. From a series of *ab initio* density functional theory (DFT) simulations assessing combinations of ternary alloys, Al-Zn-Ni and Al-Zn-Zr are determined as alloys with relatively high electrical conductivity compared to several other ternary Al alloy combinations. The zero-temperature stable structure of precipitates formed in these alloys are determined from computed enthalpy of formation as $L1_2$, with particular focus of examining the influence of Zn on stabilizing the desired $L1_2$ precipitate phase.

Scanning transmission electron microscopy (STEM) is used to examine the role of Zn addition on the morphology and phase transformation of precipitates formed in the alloys. Elemental mapping and energy-dispersive X-ray spectroscopy (EDX) in STEM mode demonstrate the enrichment of Zn, Zr and Ni in the precipitate phases. Moreover, mechanical and electrical properties of the alloys are determined. The results indicate that Zn addition improves microhardness and strength but reduces electrical conductivity, creep and thermal resistance of Al-Zr and Al-Ni alloys. Zn also has the potential to enhance the ductility of Al-Zr alloy by increasing work hardening through reduction of the alloy stacking fault energy.

Chapter 1: Introduction

1.1 Motivation

The main motivation for this research is to develop Al-Zn-Zr and Al-Zn-Ni alloys that has a more balanced, electrical, thermal and mechanical properties for high strength and electrical applications such as overhead and underground power transmission.

The first generation of cables used for power transmission were developed from Cu. However, due to its higher specific strength, high electrical conductivity, lighter weight and lower cost, Al has steadily phased out the use of Cu as the demand of electric power transmission increased[1, 2].

After early 1960s, 1350 Al alloy (containing 99.5% Al) became widely used. For instance, aluminum conductor steel-reinforced cables (ACSR) is made from strands of Al 1350-H19 (strain hardened) with steel core, Figure 1. The 1350-H19 Al alloy has a high electrical conductivity of 34.9 MS/m but low strength. The tensile strength of the alloy ($\sim 172\ MPa$) is majorly derived from dislocation entanglement, as a result of extra-hard cold work. This limits its continuous operating temperature to 90℃ (194°F), which is close to the temperature at which Al anneals. The low continuous operating temperature is due to dislocation recovery that occurs during extended use. The lack of dislocation pinning makes annihilation easier. This results in extensive softening and subsequent termination failure of the alloy[3]. One of the disadvantages of ACSR is the high sag during hot weather, due to the low thermal resistance and expansion of the 1350-H19 and steel core use.

To address the low continuous operating temperature observed in ACSR, aluminum conductor steel supported (ACSS) was developed with fully annealed 1350-O Al alloys. Annealing the alloy before using it for power line cable increases its continuous operating temperature to 250℃, due to its enhanced thermal stability. However, the alloy becomes very soft ($\sim 83\ MPa$), hence, the cable derives almost all its tensile strength from the steel

reinforcement, Figure 1. It is therefore necessary to increase the number of steel strands used in the core to improve the overall tensile strength of the cable. This leads to increased cable weight (lbs/1000 ft) compared to ACSR[4, 5]. Similarly, ACSS experiences high sag at increased temperature, due to the high thermal expansion of aluminum and steel. The electrical conductivity of 1350-O Al alloy is 35.7 MS/m, which is slightly higher than that of 1350-H19.

Aluminum conductor composite core (ACCC) was developed as the solution to the combined challenge of high sag and low continuous operating temperature experienced by ACSR. This cable is made from a hybrid carbon and glass fiber core, wrapped by 1350-O Al alloy. It has a much lower coefficient of thermal expansion (1.6 $ppm/℃$) than ACSR 11.6 $ppm/℃$, which reduces the thermal sag when operated at significantly higher temperature. However, it experiences ice loading sag due to the elastic nature of the composite core. Several other types of cable exist, however, none has a good balance between conductivity and mechanical properties.

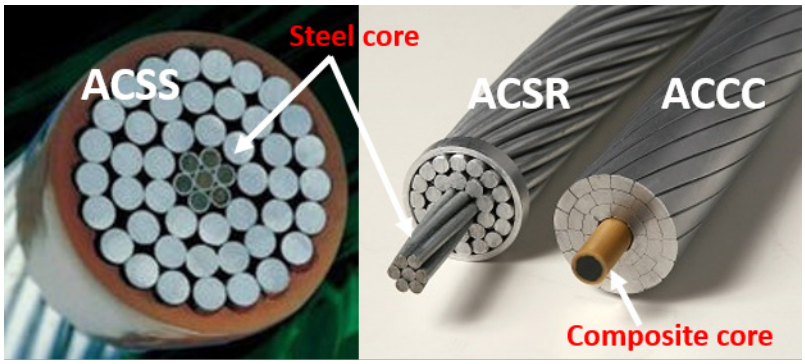

Figure 1. The steel core present in ACSR is wrapped by Al alloy 1350-H19, while ACSS and ACCC are surrounded by fully annealed Al alloy 1350-O.

1.2 Literature review

As stated in the previous section, Al alloy 1350 (H19 or O) does not have a desirable combination of high thermal resistance, mechanical and electrical conductivity. Therefore, there is need to develop an aluminum alloy that have a better balance between mechanical and electrical properties at low cost. Precipitation strengthened Al-Zr-TM and Al-Sc-TM (TM = transition metal) alloys have been studied over the years and shown to have potential for high electrical conductivity, thermal stability and enhanced strength. To achieve relatively higher electrical conductivity and enhanced strength compared to their as-cast conditions, precipitation technique was used to form secondary phases (dispersoids).

Knipling et al., studied the precipitation and high-temperature mechanical properties of isochronally aged Al-Sc, Al-Zr, Al-Zr-Sc and Al-Zr-Ti alloys. From their results, the addition of 0.1Sc (at%) to Al to form binary alloy yielded a higher peak microhardness of 668 MPa, relative to the peak microhardness achieved when 0.1Zr (410 MPa) was added. No microhardness data was found in the literature for Al-0.1Ti binary alloy, hence direct microhardness comparison could not be made with Al-0.1Sc and Al-0.1Zr. Though, Sc has a better strengthening potential than Zr, it achieves peak aging at 350℃, a lower temperature than Zr (450℃). Al-Sc starts experiences softening and overaging at a lower temperature, indicating that Al-Zr has better thermal stability. Hence, Zr is an excellent candidate for thermal stability and coarsening resistance purpose[6-9].

Due to the excellent coarsening resistance potential of Zr in Al alloys, Knipling et al. studied Al-Sc-Zr ternary alloys with the aim of improving the microhardness and coarsening resistance of the alloy relative to binary Al-Sc. Similarly, Marsha et al. also improved the coarsening resistance of Al-Sc alloys by Ti addition. This is due to the slower diffusivities of Ti and Zr, relative to Sc in Al[10].

Knipling was able to show that by increasing the combined solute concentration (Sc, Zr, and Ti) in the cast alloys to within their individual maximum solubility limit, the volume fractions of the corresponding precipitates was enhanced, thereby, yielding higher peak strengths. For instance, by increasing the solute concentration from 0.06Zr0.06Sc to

0.1Zr0.1Sc (at.%), the peak strength of the alloy increased from 610 – 782 MPa after undergoing similar isochronal aging at 25℃ temperature step size.

Naturally, the electrical conductivity of Al alloys reduces per at. % (or wt. %) solute added to the solution of the cast alloy. This indicates that increasing the solute concentration to achieve better strength would negatively affect the electrical conductivity of the alloy at as-cast. Even after precipitation of the solutes out of solution into the secondary phase, the negative effect of increased solute on electrical conductivity is still observed at peak conductivity condition. According to Knipling, the electrical conductivity measured for 0.06Zr0.06Sc was 29.4 and 34.2 at as-cast and peak aged conditions, respectively. These values were 26.4 and 33.2 MS/m for 0.1Zr0.1Sc. The measured electrical conductivity of Al-0.1Zr-0.1Ti was 26.6 and 29.2 MS/m at as-cast and peak aged conditions. This indicates that Sc does not degrade the electrical conductivity as much as Zr and Ti.

In summary, Sc is one of the most promising candidate for improving the combined mechanical and electrical properties of Al alloys, however, the high cost of Sc makes it less appealing for commercial production. Zr and Ti are also promising candidates but slightly expensive too. According to Chemicool, the approximate prices for pure Sc, Zr, and Ti are $1,400, $157 and $661 per 100 grams[11].

In order to develop ternary alloys that have improved balance between mechanical and electrical properties, while maintaining a low-cost, Al-Zn-Zr and Al-Zn-Ni alloys were studied. These alloy combinations were selected as promising candidates because of the low impact of Zn, Ni and Zr on electrical conductivity[12, 13] and their ability to form desirable coherent precipitate structure ($L1_2$)[12, 14, 15]. According to Hatch, Zn, Ni and Zr rank among the elements with the lowest impact on electrical conductivity when in or out of solution. Zr and Ni have low solid solution solubility and diffusivity in Al, which helps to retard coarsening rate. In terms of cost, the approximate prices for pure Zn and Ni are $5.30 and $7.70 per 100 grams[11].

1.3 Research goal

The goal of this research study was to develop precipitation strengthened ternary Al-Zn-Zr and Al-Zn-Ni alloys that has improved balance between mechanical (tensile strength, coarsening resistance, microhardness and ductility) and electrical properties, relative to AA1350, while maintaining a lower cost than the currently studied Al-Zr-Sc, Al-Zr-Ti, Al-Sc-Ti alloys (Group IIIB, IVB and VB transition metals).

Second, the desired secondary phase structure, formed during precipitation is $L1_2$ (which is coherent with Al matrix), because it helps to reduce the precipitate/matrix mismatch. The reduced lattice mismatch is partially responsible for improved thermal/coarsening resistance and retention of strengthening phases. This reduces softening of the alloy after annealing at elevated temperature.

To achieve this, several ternary alloy combinations were first assessed for high electrical conductivity and thermodynamic phase stability using ICME, before fabrication and testing. Electrical conductivity screening was used to determine which alloy combinations have less impact on electrical conductivity of aluminum, while the thermodynamic phase stability assessment was used to determine the zero-temperature precipitate phase structures formed in the alloys.

Chapter 2: Background

2.1 Vienna *ab-initio* simulation package – density functional theory

2.1.1 Overview

At the ICME stage, Vienna *Ab initio* Simulation Package – Density Functional Theory (VASP-DFT) was the preferred tool used to perform a quick screening of binary and ternary alloys for electrical conductivities and thermodynamic stability. The relevant output data to this study include electrical conductivity tensors, energy/atom, lattice parameters and unit cell volume. Though, due to no available experimental values in the literature, for the ternary alloys considered in this research, it is difficult to verify some of the predicted results.

In general, electrical conductivity is a complicated parameter to determine, since it is affected by temperature as well as impurities. The thorough approach is to use ab initio molecular dynamic simulations with the Kubo-Greenwood method[16, 17]. Because this approach simulates the effect of atomic movement directly, it provides for a good estimate of the temperature influence on the electrical conductivity. However, ab initio molecular dynamic simulation can be very time consuming, and a more efficient approach, such as DFT, is needed for material screening.

Ab-initio DFT computations can also be used to compute the enthalpy of formation ΔH_f (kJ/mol) from the total free energy per atom outputs. In this study the effect of Zn on the relative stability of $L1_2$, $D0_{11}$, $D0_{22}$ and $D0_{23}$ phase structures of Al_3TM, Zn_3TM and intermediate compositions are examined. For each atomic fraction of Zn in the intermetallic, whichever phase structure has the lowest ΔH_f, is considered to be the most stable structure for that particular composition[18].

2.1.2 Input and output files

To begin simulation, four (4) input files, named INCAR (simulation command codes), POSCAR (atomic positions), POTCAR (pseudo-potentials) and KPOINTS (*k-point* spacings) – see appendix for details on all the file names mentioned – are developed before uploading to VASP. These files contain the VASP set of commands, atomic positions within the unit cell, exchange-correlation functionals and number of *k-point* spacing mesh (Γ-centered Monkhorst-Pack grids) in the reciprocal space, respectively. The most relevant output files to this research study are the CONTCAR, OSZICAR and OUTCAR. They contain the final atomic positions after relaxation of the atoms from simulation, energies for every ionic step until convergence is achieved and detailed output of VASP run, respectively. Examples of the files can be found in appendix A section.

2.1.3 Optimization

Usually, the first step of the ICME process is to optimize POTCAR, *k-point* spacing and ENCUT (energy cut-off) for consistent free energy, lattice parameters and electrical conductivities computation for the individual elements (e.g. Al, Zr, Zn and Ni). Generally, optimization is performed using convergence test to see the minimum parameter required for consistent output data[19]. First, *k-point* spacing is optimized at a much higher ENCUT, before varying the energy cut-off using the optimized *k-points*. The optimized values are determined as *k-point* 70 and ENCUT 500 eV.

Once the ENCUT and *k-point* spacing are optimized using convergence test, these values are used with several pseudo-potential (POTCAR) files for a number of relevant elements to examine which file gives the most accurate free energy and lattice parameters data, relative to experiment. During convergence test, only electrical conductivity displays a slightly higher degree of scatter of its data set. The optimized POTCAR is determined as Perdew-Burke-Ernzerhof exchange-correlation functionals (PAW-PBE_52). No spin orbital coupling is used during these simulations.

2.2 Strengthening mechanism

Several strengthening mechanisms can be used to improve the strength of an alloy through restriction of dislocation motion. Only the various strengthening mechanisms employed in this study are discussed in this section.

2.2.1 Solid solution strengthening

For pure solid solution strengthening to occur, the solute concentration must not exceed its solubility limit in the solvent at a specific temperature. This mechanism occurs by solute atoms distorting the lattice structure of the solvent. The difference between the atomic size of solute and solvent atoms is responsible for the existing lattice distortion. These distortions generate several stress fields within the solvent, which impede dislocation motion. The stress fields imparted on lattice by the presence of the solute atoms can either be compressive or tensile, depending on the solute size (size effect).

According to Fleischer equation, the shear stress required to move dislocations past the solutes in a material is[20]:

$$\Delta\tau = \frac{G\epsilon^{\frac{3}{2}}\sqrt{c}}{700} \qquad (1)$$

ϵ can be defined as the total strain caused by lattice and modulus mismatch below:

$$\epsilon = |\epsilon'_G - \beta\epsilon_a| \qquad (2)$$

the lattice misfit strain is proportional to local change in lattice parameter:

$$\epsilon_a = \frac{\Delta a}{a\Delta c} \qquad (3)$$

while the equation describing the modulus mismatch:

$$\epsilon'_G = \frac{\frac{\Delta G}{G\Delta c}}{1+\frac{1}{2}\left|\frac{\Delta G}{G\Delta c}\right|} \qquad (4)$$

where c is concentration of solute atoms in atomic fraction, G is shear modulus of the solute atom and ϵ is the lattice strain due to solute. The ϵ'_G captures the local modulus change, ϵ_a

is lattice distortion term, a is lattice parameter of the material, β is a solute atom dependent constant. To be able to use this model for solid solution strengthening prediction, the β constant needs to be known.

In order to achieve significant material strengthening from solid solution strengthening, the solute atoms included in the alloy must have higher shear modulus, thereby, increasing the local shear modulus in the alloy. Another factor that could have major impact on solid solution strengthening of the alloy is the difference between the lattice parameters of solute and solvent atoms. This indicates that the bigger the lattice mismatch, the higher the local stress and lattice strain fields induced in the alloy. In summary, solid solution strengthening magnitude depends on concentration, shear modulus, size and vacancy of the solute atoms.

Solid solution strengthening negatively impacts the electrical conductivity of Al alloy, due to the induced strain fields from the solutes present in the alloy. The strain fields hinder the flow of electrons in the presence of electric field. Since electrical conductivity is directly proportional to the mobility of charge carriers (electrons or holes), adding more solutes to an alloy decreases the flow of electron and corresponding electrical conductivity.

2.2.2 Precipitation strengthening

Precipitation strengthening is one of the most effective methods for achieving increased mechanical and electrical properties of Al alloys[21]. This technique is essentially used to nucleate and grow nanosize precipitates that are effective in obstructing dislocation motion, thereby, improving the strength of the alloy. As the solutes come out of solution to form precipitate phase within the solvent, the lattice distortion of the solvent, due to the presence of the solutes is reduced. Thereby, increasing the electrical conductivity of the alloy. These precipitates are formed in the alloy by aging at a temperature within the two-phase region of the alloy phase diagram. This mechanism is diffusion dependent.

The size of the precipitates increases as the aging temperature and/or time increases. The degree of strengthening achieved from precipitation is determined by the volume fraction and particle-dislocation interaction. Whereby, the particle-dislocation interaction is

dependent on particle size, crystal structure, shear modulus, precipitate-matrix lattice mismatch.

When a precipitation hardened metal alloy is stressed, each individual secondary phase precipitate has a force, *F*, that resists the movement of dislocation as shown in the schematic, Figure 2[22].

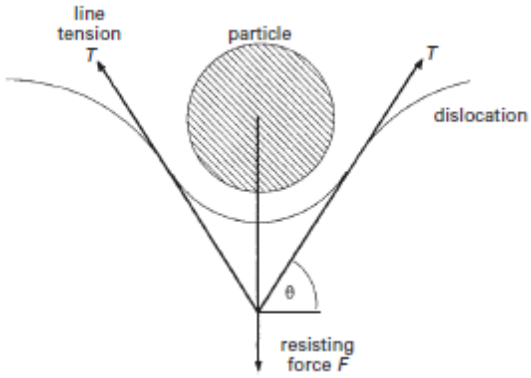

Figure 2. Interaction between spherical precipitate and dislocation line tension[23]. Depending on the magnitude of the resisting force, the dislocation decides to either loop or shear the precipitate.

The line of tension T, of the dislocation, is proportional to the resisting force of the particle according to equation (5):

$$F = 2Tsin\theta \qquad (5)$$

where θ is the angle of dislocation bowing. *F*, increases with precipitate size, indicating that as the precipitate size increases, it becomes harder for the dislocation to shear. The line of tension is maximum when $\theta = 90°$ and $sin\theta$ is 1. Therefore, when the maximum value of dislocation line of tension $2Tsin\theta >$ particle resisting force F, where *F* is proportional to the shear modulus of the precipitate, the particle will shear as a result of the dislocation cutting through. This indicates that the energy required to shear the particle is less than the

energy required to loop through the dispersed precipitates. The higher the precipitate volume fraction the more difficult it is for dislocations to loop around due to small interparticle spacing. Hence, the strength of the alloy is dependent on the precipitate volume fraction and shear modulus, and is maximum when the particles are sheared by dislocation. If, however, $F > 2T sin\theta$ (maximum line of tension), which usually occurs for bigger particles (with wider average interparticle spacing), dislocations will rather bypass the precipitates, either by Orowan looping or cross slip (equation for Orowan strengthening can be found in chapter 4 and 5)[22]. When this happens, it means that lower energy is required to bow the particles.

The preferred crystal structure of the precipitate formed in this study is coherent $L1_2$, due to its similarity to FCC aluminum matrix phase. The purpose of forming a precipitate phase that is coherent with the matrix is to reduce precipitate-matrix lattice mismatch and subsequently slow down coarsening rate. Coherent particles also generate surrounding strain fields associated with stretching bonds – these have the potential to impede dislocation motion through coherency strain strengthening.

2.2.3 Strain hardening

This strengthening mechanism is a process in which materials are made stronger by plastic deformation. When the material is plastically deformed, the number density of dislocations are multiplied, which leads to dislocation pile up and enhanced dislocation entanglement. Increasing the percentage reduction area ($\%RA = \frac{A_o - A_i}{A_0}$) yields a corresponding higher dislocation density. Further permanent deformation is prevented after severe strain hardening due to possible brittleness of the alloy.

Strain hardening is divided into cold work and hot work. Hot working is a process whereby metals are plastically deformed above their recrystallization temperature, whereas, cold work occurs below the recrystallization temperature. From microstructural observation, the uniaxial grains in a cold worked metal are elongated in the direction of the work hardening. In this study, the alloys are cold worked using swaging and wire-drawing techniques.

Chapter 3: Experimental techniques

3.1 Alloy casting and specimen preparation

The procedure of metal alloy fabricating involved, cutting the elements charge before melting and mixing in the chamber. After melting inside the graphite crucible placed in the vacuum chamber, the alloys were poured into the mold before allowing them to solidify and cool down. Before taking measurements, mechanical testing and acquisition of microstructure data, specimens were prepared. Specimen preparations used in this study could be divided into cutting, surface treatment and deformation. Band saw, wet cutter and wire EDM are classified into cutting, while surface treatment includes grinding, auto-polishing and electropolishing. Swaging and wire drawing were used to deform the alloy rods for tensile experiments.

3.1.1 Band saw and wet cutter

After determining the mass quantity (in grams) of individual elements and master alloys in the alloy composition, the ingots were cut using a horizontal band saw with sufficient coolant. The band saw was first used due to the size of the initial cut out from the ingot; using the wet cutter would lead to breakage of the SiC abrasive cut-off disc.

The wet cutter was used to cut the larger pieces into smaller sections that could fit into the crucible. The wet cutter abrasive cut-off disc was also used to cut all the buttons and rod specimens in this research before polishing, swaging or wire-drawing. The disc (Allied High-Tech Products, 35.56 cm diameter, 80-10025) was bolted to a LECO CM-24 cut-off machine. While in operation, integrated coolant recirculation occurred. Figure 3 shows the image of the cutter used.

The cut-out pieces were all placed in ultrasonic acetone bath for at least 5 minutes to remove all burs and cutting fluid. The face of each piece was washed with soapy water and cotton ball before rinsing in running water and ethanol.

Figure 3. Wet cutter used to cut all ingot into rods and button specimens. The specimens were cut with 80-10025 abrasive cut-off disc (Allied High-Tech Products) screwed to the cutter.

3.1.2 Vacuum induction melter

This is a vacuum chamber used to fabricate cast alloys. This chamber has a coil that can hold the graphite crucible (60 mm dia. by 170 mm height) and can melt up to 600 g of alloying materials. A water chiller, rough mechanical and a diffusion pump are connected to the vacuum chamber to achieve a vacuum level of up to 1×10^{-5} Torr. An argon tank connected to the chamber is used to backfill. This is mostly done to prevent a lot of elements with high vapor pressure from leaving the melt in the crucible. During melting, alternating current (AC) power was gradually ramped to increase the temperature inside the chamber. The temperature inside the chamber was measured with Accufiber HF-3 optical pyrometer. The VIM unit is shown in Figure 4.

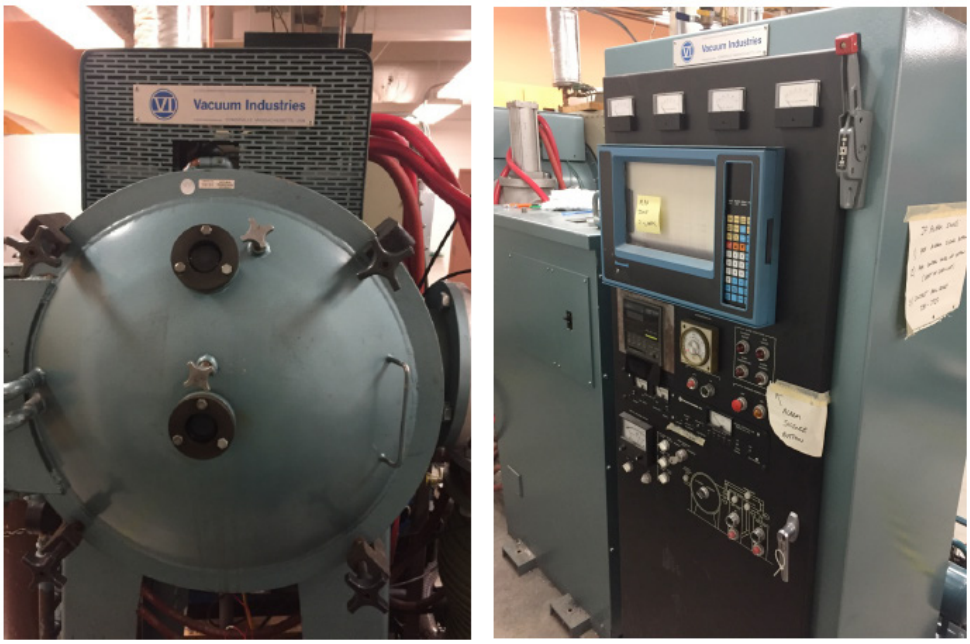

Figure 4. Vacuum induction meting unit, used to cast all alloy used in this study.

3.1.3 Wire EDM

The JAPAX LUX3 Wire Electrical Discharge Machining (Wire EDM) shown in Figure 5 uses spark erosion to cut through a specimen with bronze wire. EDM was used to cut thin cross-section of the specimen before grinding and electropolsihing for TEM experiment.

Figure 5. Wire EDM equipment for cutting thin alloy specimens. The thickness in the X direction was set to 500 on the machine. This corresponds to ~250 mm specimen thickness before auto-polishing to 100 mm.

To begin operation, the following settings were selected, and codes inserted:

- $T_{\text{off}} = 10$
- $T_{\text{on}} = 4$
- $I_{\text{o}} = 3$
- $V = 4$
- $V_{\text{s}} = 4$
- $\% = 100$
- $Feed = 10$
- $Tension = 6$
- F varies with thickness (sheeting = ~8)
- Basc II for uniform thickness, Basc I for non-uniform

G-Code was set-up to define the cutting path and speed of the wire (details about the code can be found in the laboratory):

$N01\ G21\ G91\ X0.Y0.$

$N02\ G01$. Y-30.

$N03\ M02$

/Store

The conducting specimen is secured to the motorized stage in a way that it is grounded. The spook of Bedra Bercocut bronze wire is continuously unwound from the JAPAX JAPT 3F, as it gradually cuts through the specimen in the y-direction. Simultaneously, distilled water runs as the wire cuts through the specimen. This helps cool the specimen. The JAPAX #PW20X wire EDM filtration unit is responsible for maintaining the conductivity of the distilled water.

3.1.4 Swaging and wiredrawing

Through swaging and wire drawing, the 19 mm diameter rod specimens were reduced to 4.6 mm diameter. This amounts for 94% CW. The cold work process was divided into two (2) stages:

- Swage specimens from 19 to 9.5 mm using the FENN 765 swager.
- Wire-draw from 9.5 to 4.6 mm, while using the Swager to reduce the near end of the rods before each step of wire-drawing. Wire drawing was performed with the MEC MACBEE (230 V; 60 Hz) machine.

Swaging the tip before wire drawing made it possible to pass the rods through the wire-drawing machine. As the rods got thinner in dimension, they became prone to breakage, especially the heat treated specimens. Most of the Al-Ni and Al-Zn-Ni alloys were able to go through the whole cold work process without experiencing breakage, relative to Al-Zr and Al-Zn-Zr, due to their higher ductility. To prevent breakage of the alloys with Zr, the step size of the die was 10 – 15 % reduction.

Another factor that could lead to specimens breaking is friction between the rod specimen and the die. Hence, during swaging and wire-drawing, proper lubrication of the dies was ensured so as to reduce the friction that occurred when passing the specimens through. The swaging and wire drawing equipment set up is shown in Figure 6.

Figure 6. (Left) Swaging and (right) wire drawing unit. The swager was used for cold work of the rod specimens, thereby reducing their diameters from 19 to 9.5 mm, before wiredrawing to a smaller diameter (4.6 mm). Before each die step of wire drawing process, the swager was used to first reduce the tip end of the rods to enable it pass through the wiredrawing die.

3.1.5 Grinding and auto-polishing specimens

Before proceeding to the grinding and polishing stage, the button specimens that were cut out of the ingots were placed inside several 3.175 cm diameter-mounting cups. The button specimens were mark-labelled with a Wen Power Tool electric engraver, so they could be distinguished after mounting. An epoxy containing 2:1 Quickset Acrylic Powder (#185-10005) to Acrylic Liquid Hardener (#185-10010) volume ratio were thoroughly mixed, before pouring on top of the button specimen, placed in the mounting cup, ensuring that the specimen was covered. The epoxy was allowed to solidify after approximately 10 minutes.

After solidification the mounted specimens were removed from the mount cup. Hand grinding operation were performed on the specimens, with the following grinding steps:

180, 320, 600 and 1500 SiC paper grit. The samples were rinsed with cotton balls, soap and running water between each grinding step to remove any grit particles on the specimen surface.

The next step was to progress to the auto-polishing stage, with the use of Leco Polisher Grinder. The polishing steps included red or green lube with 6 and 1 micron diamond paste plus pads. Finally, the Allied 0.04 micron Colloidal Silica Suspension plus pad was used to get a mirror-like shiny surface. The specimens were washed with cotton balls, soap and running water before placing in ethanol solvent, in ultrasonic bath for approximately 5 minutes. See image in Figure 7 for autopolisher tool, button specimen and mounting cup.

Figure 7. Auto-polishing equipment used to polish button specimens after mounting, using the mounting cup on the right.

3.1.6 Electropolishing

All specimens examined with S/TEM and SEM were electro-polished. The thin sheets (~200 micron thickness) cut-out from the button specimens, with Wire EDM, were first auto-polished to ~100 micron thickness sheet, using 400, 800 and 1200 SiC grit papers.

After, ~3 mm diameter TEM foils were punched from the auto-polished sheets. The thin foils were carefully arranged in a labelled TEM grid storage box.

The actual electro-polishing process was done with an FTS System Multicool chiller connected to the Jet Electropolisher. The Jet polisher included a Metalthin digital instrument connected to the polishing cell, specimen holder and electrolytic solution tank. A thermometer was placed in the tank to read the temperature of the electrolyte. See Figure 8 for electropolisher set-up.

Figure 8. Electropolisher set-up used to polish the TEM specimens. (Top left) The FTS System Multicool chiller used to maintain the cold temperature of the electrolyte. (Top right) The tank that contains the mixture of nitric acid and methanol electrolyte, used to remove surface layer of the specimens during polishing. The polishing cell (including specimen holder) is placed on-top of the tank. (Bottom) Metalthin digital instrument used to control polishing parameters.

The following operation settings were used for the Metalthin instrument:

- Sensitivity: 4-8
- Voltage: 12-20 V
- Current: Corresponds to the voltage used but varied from 65-200 mA, depending on how well polished the prior auto-polish was performed.

3.2 Heat treatment

All heat treatments of the specimens were performed in box furnaces. After setting the temperature on the PID controller, the furnace was gradually heated up to the set temperature. The temperature was allowed to stabilize at the set temperature before placing the specimens inside. The PID controller on the furnace reads the temperature from internal thermocouples mounted on the top of the furnace. The specimens were quenched in cold/room temperature water after each temperature and time step. The box furnace is shown in Figure 9.

Figure 9. Box furnace used for isochronal and isothermal heat treatments of the specimens before water quenching.

3.3 Measurements

3.3.1 Vickers microhardness

This experiment was performed using the LECO M-400-G1 instrument. To begin microhardness measurements, auto-polished button specimens were drilled out of the epoxy and secured to the specimen holder. A diamond (quadrilateral pyramidal) indenter was pressed on the polished surface of the specimen. The settings used for the experiments were:

- Load weight: 50 – 100 g
- Dwell time: 15 seconds
- Objective lens: 50×

The microhardness value is proportional to the size of the indent and displaced volume. The microhardness value recorded by the instrument was converted to microhardness in MPa by multiplying by 9.8 MPa. See Figure 10 for Vickers microhardness tester.

Figure 10. LECO M-400-G1 Vickers microhardness equipment.

3.3.2 Electrical conductivity

Two different electrical conductivity setups were used throughout this research. For the polished buttons, measurements were taken with a Fisher Technologies Sigmascope SMP10 device and probe. While, the electrical conductivities of the wire drawn specimens were taken with a Keithley setup.

The Fisher SMP10 device has a surface contact probe with a probe size is ~12.7 mm (0.5 inch) diameter. Therefore, the specimen to be tested have to be wider in surface area to fully accommodate the end of the probe. It is essential to have at least the first couple of grinding (> 400 SiC grit size) performed on the specimens to achieve flat surface. This is necessary so that the probe makes a complete contact with the specimen surface. Calibrations of the probe is performed before measurements are taking, by first inserting the accurate temperature of the specimens. Temperature calibrations (measured by an integrated thermocouple) are done by placing the probe on the specimen surface for at least 30 seconds, until the temperature reading stabilizes. Figure 11 shows the image of Fisher SMP10 tool used to measure the electrical conductivity of the button specimens.

Figure 11. Fisher SMP10 device used to measure eddy current conductivity. The probe size (~12.7 mm diameter) is placed on the surface of the button specimen in order to take conductivity measurements.

As for the Keithley setup, the current and 2182A nanovoltmeter (voltage) source are connected to the wire/rod specimens through a knife-edge voltage contact stage designed at the machine shop. It is important for the voltage contacts to be very sharp, so as to eliminate inaccuracies when measuring the voltage length (V_L) between the contacts. V_L is a very important parameter in calculating electrical conductivity. The average diameter of the specimens were taken with a digital micrometer Vernier caliper. The equation below was used to calculate the electrical conductivity.

$$\sigma = \frac{V_L}{RA} \qquad (6)$$

where R is resistance and A is the cross-section area of the wire specimen. Figure 12 shows the Keithley set-up used to measure wire specimens.

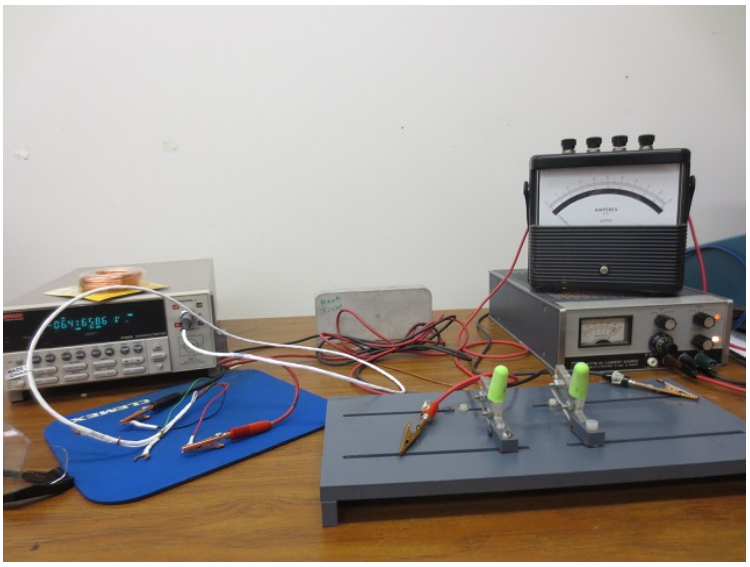

Figure 12. The Keithley conductivity set-up consist of 2182A nanovoltmeter, current source, alligator clips and a knife edge contact stage, all connected to the wire specimens. Voltage readings were taken from the nanovoltmeter at a specific set current (500 mA).

3.3.3 Tensile test

In this research, Instron tensile test equipment with Futek (Model # LCF455) maximum load capacity of 10,000 lbs was used for all mechanical test experiments except creep test. The setup consisted of two radial grip fixtures connected to the base and the load cell, they were used to clamp the material that was tested. The radial diameter of the grip is between 3.2 – 8.4 mm (0.125 – 0.25 inch).

TestWork software on the computer connected to the system was used to configure the Epsilon 1" extensometer and 10,000 Futek tension load used. This is essential for accurate data output. The position and load on the grips was zeroed before placing the specimen and tightening the grips. The extensometer was zeroed after attaching it to the gage length of the specimen. Before starting the experiment, the diameter of the rod/wire specimen, test speed and strain rate were inserted. For a specific gage length of 2 inch, the test speed was set at 0.24 in/min. This corresponds to a strain rate of $2 \times 10^{-3}\ s^{-1}$ used for all tensile tests performed.

Initially the specimen tested were 101 mm (4 inches) in length and uniform diameter of 4.6 mm (0.182 inch) – specimen tensile bar design A. A 50.8 mm (2 inch) gage length was used for all specimens, while an Epsilon extensometer (1 inch) attached to the equipment was clamped to the gage length. Most of the elongation test performed, using this design, broke inside the grid. Preventing the uniform diameter wire specimens from breaking near or inside the grip was one of the major challenges faced during tensile testing. Whenever the specimen break within the grip, it leads to error in the elongation data. However, the tensile and yield strength remain accurate. With a uniform wire specimen diameter, breakage inside the grip occurred when the force applied while tightening the two grips were unequal. Since it was impossible to measure the force applied on each grip during tightening, preventing such breaks became impossible.

To prevent specimen break, the diameter of the gage length region of the tensile specimen was lathed. The new diameter and length of the lathed region was approximately 3.8 mm (0.150 inch) and 38.1 mm (1.5 inch), respectively (specimen tensile bar design B). This

new wire specimen design allowed the breakage to occur within the gage length and Epsilon extensometer. See Figure 13 for the tensile test grid set-up and tensile specimen.

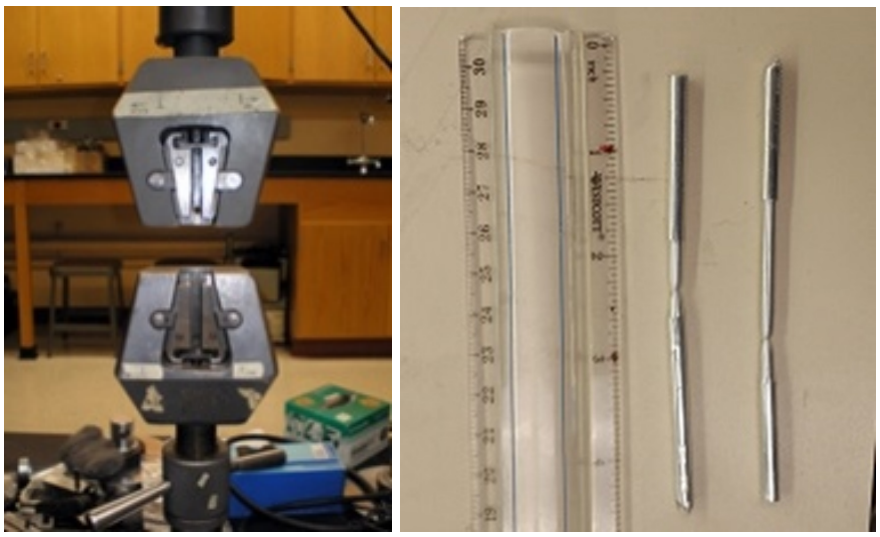

Figure 13. (Left) Tensile test grid set-up with wire specimen tensile bars, (shown on the right). The lathed gage length and diameter are 38.1 mm and 3.8 mm respectively.

3.3.4 Creep strain

Creep test was performed on as-wiredrawn and thermal aged wire specimens, using an Instron screw-driven tensile testing frame. A three-zone open-ended vertical tube furnace was used to maintain a constant temperature of 250ºC over the entire length of test specimens. During creep test, stress was first ramped to the target stress of 40 MPa within 15 seconds, held constant over the length (2.5hrs) of the creep test, and then dropped to zero. Figure 14 shows the creep test set-up.

Figure 14. Instron screw-driven tensile testing frame was used to apply a constant stress of 40 MPa on the specimens. The ambient temperature of the specimens was kept at 250°C using a three-zone open-ended vertical tube furnace.

Total strain at the end of the creep test (ϵ_{total}) and initial strain as stress ramping completes ($\epsilon_{initial}$) were used to calculate creep strain:

$$\epsilon_{creep} = \epsilon_{total} - \epsilon_{initial} \qquad (7)$$

Figure 15 shows an example of strain development of the duration of creep test.

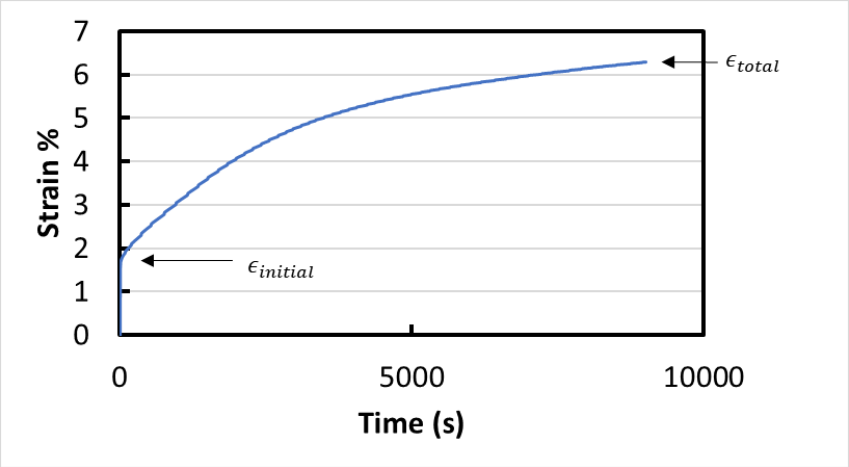

Figure 15. Sample strain over the duration of the load-controlled creep test.

Creep strain rate was calculated as:

$$\dot{\epsilon}_{creep\ strain\ rate} = \frac{\epsilon_{creep}}{2.5hr} \qquad (8)$$

3.4 Microstructure analysis

3.4.1 Scanning transmission electron microscope

All transmission electron microscopy (TEM) imaging were performed with the FEI Titan Themis S-TEM, operating at 200 kV. The Themis has a full complement of state of the art accessories, including six (6) specialized specimen holders that extend the S-TEM utilities. Energy Dispersive X-ray Spectroscopy (EDX) analysis is performed on the elemental mapped specimens. Figure 16, shows the S-TEM set-up used for microstructure study.

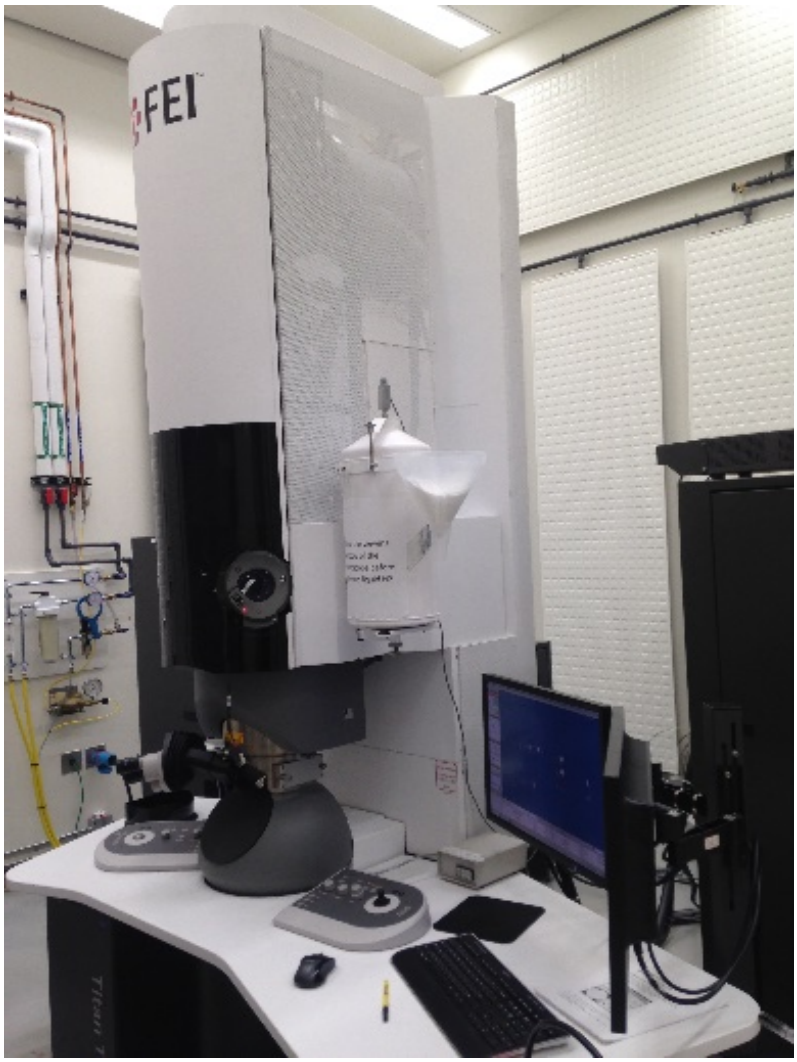

Figure 16. FEI Titan Themis Scanning Transmission Electron Microscope, operating at 200 kV, used for microstructural analysis. The double tilt holder was used while examining each specimen.

To begin, the electropolished thin foil specimen was placed on the double tilt holder and clamped gently to prevent a loose specimen falling off inside the chamber. The specimen holder including the specimen were cleaned under plasma plume to remove any form of oxide layers or contamination. Plasma cleaning took a minimum of 5 minutes before inserting the specimen holder inside the chamber.

The startup setting included the following:

- Octagon pressure 16
- Gun was always set to 1 and on
- LN was 15 – 54%
- Col Valve close = yellow color: This meant there was a covering of the gun beam
- When the Col Valve was clicked, and the button turned grey: This meant the valve protecting the gun was open
- Under HT/FEG/Vacuum tab, FEG Registers was selected and the instrument setting was changed from S-TEM to TEM mode or vise-versa
- 200kV TEM – was selected and set button was clicked
- SA 72000× TEM: The magnification was reduced to 4000× to make the beam visible if it is not visible on the stage

The Z-height, beam tilt, beam shift and objective aperture alignments were performed to improve the quality of the image acquired. To examine the diffraction pattern of the matrix or precipitate phase, the magnification was set to 28000 – 36000× before the specimen was tilted by adjusting the α and β. The tilt was performed to find a specific zone axis of interest.

3.4.2 Environmental scanning electron microscope

The FEI Philips XL 40 Environmental Scanning Electron Microscope is a large chamber scanning electron microscope (SEM) with advanced accessories that include a thin window energy dispersive spectrometer (EDS). It was used to perform SEM experiments on electropolished thin foils.

To load the specimen, a double-sided carbon conducting sticky tape was laid down on the specimen pin mount. The edge of several specimens examined were placed on the sticky tape to hold and prevent it from falling inside the vacuum chamber during the experiment. The specimen pin mount has a big enough diameter to hold between 5 – 10 specimens, as long as they are labelled properly for identification purpose. After placing the specimens on the pin mount, it was placed on the mounting platform that slides onto the SEM stage.

Generally, for SEM imaging, the specimen needs to be either conductive or coated with metal for grounding purpose. This is done to prevent electron beams from charging the specimen and distorting the images. After loading the specimen inside the chamber and the chamber door was closed, vacuum was created inside the chamber before running the experiment. The Scanning Electron Microscope used for this research is shown in Figure 17.

Figure 17. FEI Philips XL 40 Environmental Scanning Electron Microscope used for acquiring backscattered images of Al-Zr and Al-Zn-Zr precipitate morphologies after aging at 600°C.

The column valve was opened so the electron beam from the gun's tungsten filament could pass through the column. The image from the specimen was focused and aligned in secondary imaging mode, before capturing the microstructure features in backscatter electron imaging mode to enhance the visibility of the precipitates formed in the specimens. Backscatter electron imaging mode allows only elastically scattered, high energy electrons, reflected out of the specimen, after interaction with the atoms of the specimen, to be detected. On the other hand, secondary imaging is derived from secondary electrons emitted by excited atoms due to interaction with electron beam.

Chapter 4: Investigation of Al-Zn-Zr and Al-Zn-Ni alloys for high electrical conductivity and strength application

Accepted for publication in Materials Science and Engineering A

4.1 Abstract and introduction

4.1.1 Abstract

Al-Zn-TM (TM=Transition metals) alloys are developed with an integrated computational material engineering (ICME) strategy. Al-Zn-Ni and Al-Zn-Zr are determined to have promising electrical conductivities via a series of *ab initio* density functional theory (DFT) simulations assessing combinations of Al-TM and Al-Zn-TM. The computed enthalpies of formation are used to identify the zero-temperature equilibrium precipitate phase in both alloys with increasing levels of Zn content, with a particular focus of finding Zn content levels that result in a precipitate $L1_2$ structure. The corresponding microhardness and electrical conductivity measurements of both alloys are evaluated. Transmission Electron Microscopy (TEM) is used to examine the morphology of the $Al_{3-x}Zn_xNi$ and $Al_{3-x}Zn_xZr$ precipitates formed in the respective alloys and their structures were confirmed as $L1_2$ by selected area electron diffraction (SAED). Through qualitative chemical analysis, it is demonstrated that Ni and Zr are not present in the matrix but are completely used up in forming the respective precipitate phases in both alloys.

4.1.2 Introduction

The Integrated Computational Materials Engineering (ICME) approach involves the use of computational simulation tools to facilitate the materials development process for targeted high strength and electrical conductivity engineering applications[24], thus reducing the number of design iterations and overall development time and cost. The ICME approach

is well suited for the development of new aluminum alloy systems because of the presence of a well-defined metric (e.g. electrical conductivity and energy of formation) and a corresponding structure-property simulation tool for this purpose. For the ICME development of new metallic alloys, Density Functional Theory (DFT)[19] is a powerful computational tool for predicting stable crystal structures and estimating electrical conductivities for multi-element alloy systems. DFT has been used extensively for predicting structural, physical, and chemical properties of aluminum alloys and intermetallic compounds. Such properties include elastic constants[3, 4, 25], lattice parameters[26], stable microstructures, and density of states[15, 27, 28]. As the initial step in the ICME process, a broad range of Al alloys was selected for exploration of electrical conductivity and subsequent prediction of precipitate phase structure.

Precipitation strengthening utilized in this study is one of the most effective mechanism for enhancing alloy strength. For improved retention of precipitation hardened Al alloy strength, transition metal (TM) elements were specifically selected as solutes, because of their low rate of diffusivity and favorable solvus line with high solubility at solutionizing temperatures and low solubility at aging temperatures. The low rate of TM diffusivity in aluminum reduces the rate of precipitate coarsening, thus retaining the alloy strength at elevated service temperatures for longer periods of time. The low solubility at aging temperature increases the precipitate volume fraction and corresponding precipitation strengthening, because, majority of the solute atoms precipitate out of solid solution during aging. Low concentrations and solid solubility of alloying elements, especially in solution, are required to minimize their negative impact on the electrical conductivity. Another important benefit of using some transition metals includes resistance to corrosion[13].

Since aluminum has an fcc crystal structure, it is desirable to form precipitates with $L1_2$ crystal structure to minimize lattice mismatch and enhance precipitate/matrix lattice coherency. Coherency strains due to the minimal lattice mismatch is responsible for improved creep resistance and alloy strength through obstruction of dislocation motion by the strain fields surrounding the coherent precipitates[29]. A large lattice mismatch (observed in incoherent and semi-coherent precipitates) can be a driving force for

precipitate coarsening. Therefore, it is expected that coherent $L1_2$ precipitates provide greater strengthening phases than precipitates of other crystal structures. Of all binary Al-TM systems, only Al_3Sc trialuminide has a thermodynamically stable $L1_2$ structure. Though, several studies have shown that metastable $L1_2$-Al_3Zr precipitate structures form in Al-Zr alloys during aging. However, some of these $L1_2$ precipitates transform back to their equilibrium $D0_{23}$ structure at high temperatures (> 475 ℃)[30, 31]. Precipitates formed in binary Al-Ni alloys have a stable orthorhombic $D0_{11}$–Al_3Ni phase[32], which is incoherent with the α-Al matrix. Hence, the need for precipitate phase transformation from $D0_{11} \rightarrow L1_2$.

Most TMs have very low solid solubility limit ($< 1\ at.\%$) in the α-Al matrix, which limits the volume fractions of the precipitate formed in binary Al-TM alloys to $\phi < 1\ vol\ \%$ from aging, and their corresponding strengthening from precipitation hardening[29]. Hence, the need to develop ternary Al-TM_1-TM_2 alloys with stable $L1_2$ precipitate phase and increased precipitate volume fraction. Several studies of Al-Zr-Ti and Al-Zr-Sc ternary alloys have shown improved $L1_2$ precipitate volume fractions and corresponding microhardness values relative to Al-Zr, but their electrical conductivities are severely impacted[30, 31]. For instance, Knipling determined the electrical conductivities of Al-0.1Zr-0.1Ti and Al-0.1Zr-0.1Sc (at.%) as 26.6 and 26.4 MS/m at as-cast and 29.2 and 32.8 MS/m at peak condition, respectively[30, 33].

To form a suitable ternary aluminum alloy with high electrical conductivity, a natural choice of TM element is Zn. As shown in Figure 18, Zn has a minimal impact on electrical conductivity of Al, relative to other metals. However, it is generally more soluble in aluminum than other TM elements, hence, most of the added Zn remains in solid solution during the aging process[29]. It has been shown that the addition of Zn to aluminum results in minimal improvement of tensile strength through solid solution strengthening[29]. Thus, it follows that binary Al-Zn alloys are not suitable for achieving both high conductivity and strength. When in solid solution, solutes have significantly more negative impact on the electrical conductivity of the alloys (Figure 18) than when out of solution[13]. Taking advantage of Zn solute's minimal impact on the electrical conductivity of Al, when in or

out of solution, ternary Al-Zn-TM alloys with improved strength could therefore be developed, while still maintaining high electrical conductivity of the alloys[34].

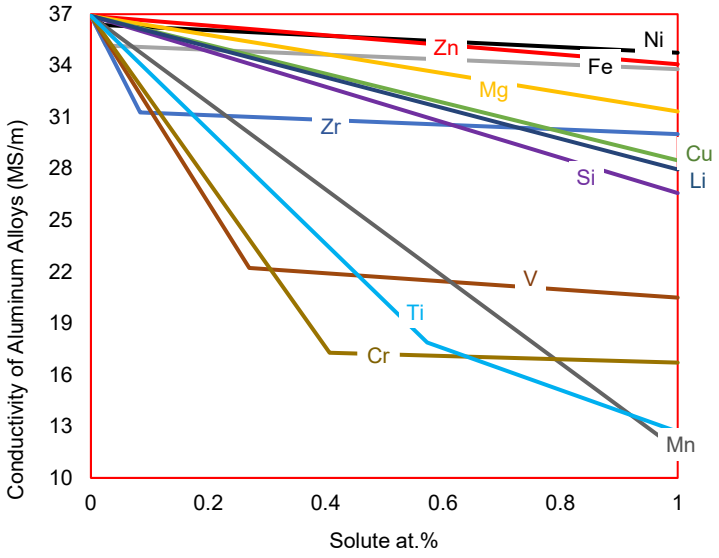

Figure 18. Experimental values of electrical conductivity drop, due to addition of 0-1 wt.% of each TM solute atom to form binary Al-TM alloy. Adapted from Hatch at room temperature 20°C[13]. The change in slope occurs at the solvus line and corresponds to the composition beyond which excess solute precipitates out of solution.

Studies have also shown that adding Zn to certain binary Al-TM alloys to form $L1_2$ ternary Al-Zn-TM compounds are possible. The elements known to stabilize the ternary $L1_2$ crystal structure with respect to non-cubic $D0_{22}$, $D0_{23}$ and $D0_{11}$ all have atomic radii smaller than aluminum and contribute to the reduction of c/a ratio of the $D0_{22}$, $D0_{23}$ and $D0_{11}$ phases[35-37] or the number of d-shell electrons[35, 36]. For these reasons, the addition of Zn could be effective for transforming the non-cubic precipitate structures of Al_3Ni to $L1_2$. According to Fine et al.[34], the use of ab-initio modeling predicts that adding Zn to Al_3Zr improves the stability of metastable $L1_2$ precipitate phase. Which they verified by qualitative comparison of EDX data from the matrix and precipitate.

The objective of this study was to use ICME to facilitate the design, fabrication and testing of new aluminum alloy systems for high electrical conductivity applications, with

improved mechanical properties, such as microhardness and yield strength. One application for these alloys is high-voltage electrical power transmission cables. DFT simulations were used to efficiently screen candidate alloy systems for subsequent experimental testing. Based on DFT results, Al-Zn-Zr and Al-Zn-Ni alloy systems were selected for experimental analysis because of their relatively high electrical conductivity and ability to form stable $L1_2$ precipitate phase required for improved alloy strengthening. In this paper, the computational effort is first described, followed by the experimental fabrication and characterization.

4.2. Computational modeling

This section describes the computational modeling methods and results that were used to efficiently down-select Al-Zn-Zr and Al-Zn-Ni as alloy candidates with optimal properties (electrical conductivity and precipitate phase stability). The pseudo-potential utilized for the simulation of each binary and ternary alloy system was a concatenation of the pseudo-potential of the individual elements present in the specific alloy system simulated. These pseudo-potentials were selected from the PAW-PBE_52 category; they included zn_pv_GW, zr_sv_GW, Ni_sv_GW and Al_sv_GW. For every other transition elements, TM_sv_GW pseudo-potential was selected, because it generated physical properties (e.g. lattice parameter) that were consistent with experimental data of the elements.

4.2.1 Method of electrical conductivity prediction

For the DFT simulations, the generalized gradient approximation (GGA) with Perdew-Burke-Ernzerhof (PBE) functional was used as implemented in the plane-wave Vienna Ab-initio Simulation Package (VASP)[38]. The DFT approach was selected for this study because it efficiently provides a first-order prediction of the electrical conductivity and zero-temperature stability of the $L1_2$ precipitate phase for different alloy systems. In general, the electrical conductivity of metals is affected by the crystal structure, the presence of impurities, and temperature (which causes atomic vibrations that disrupt the transport and energetics of electrons near the Fermi surface). Although all these factors can be simulated using large ab initio Molecular Dynamics simulations (a series of DFT

simulations that include thermal motion) and the Kubo-Greenwood formula[16, 17], this approach can be prohibitively time consuming for material screening efforts such as this. The electrical conductivity of metal alloys is also dependent on whether the alloying elements are in or out of solution (precipitation). The negative impact of alloying elements in solid solution on electrical conductivity is greater than when out of solid solution as secondary phase precipitates[13].

A more efficient approach is to use the semi-classical method[39], which predicts the electrical conductivity with a single DFT simulation at 0 K. Although this approach does not consider the influence of thermal fluctuations on the scattering of electrons, precipitation of secondary phase from solid solution, and the presence of impurities (in this case Zn and TM); it does consider the density of state (DOS) predictions and the influence of temperature on the smoothed Fourier interpolation of the band. Density of state is a function $\rho_{energy}(E)$ that when multiplied by an interval of energy dE between energy states, E and $E + dE$, provides the total concentration of the available states. It however does not provide any information about the number of states occupied by charge carries (e.g. electron). Therefore, the probability that an electron resides at a given energy is denoted by P(E), while the concentration of electrons at a given energy E is given as[19]:

$$n_e(E) = P(E)\rho_{energy}(E)dE \qquad (9)$$

where *P(E)* is the Fermi-Dirac distribution, $P(E)\rho_{energy}(E)$ implies that most of the electrons reside near the conduction band edge. Hence, the total concentration of electrons in the conduction band is given by:

$$n_c = \int_{E_C}^{\infty} P(E)\rho_{energy}(E)dE \qquad (10)$$

E_C is the starting energy of the conduction band. Generally, DFT utilizes the influence of the alloying elements included in Al matrix on the electron charge distribution and DOS of each Al alloy system to determine n_c.

This method has been used previously for prediction of electrical conductivity[40-43]. Though, it is however important to note that what DFT computes is the frequency

dependent electrical conductivity tensor values. For any particular element, these tensor values vary with the number of atoms present in, or symmetry of the simulation cell. Hence, a direct comparison could not be made with experimental electrical conductivity. However, as long as the size of all the simulation cells (or number of atoms in simulation cell) are the same, the electrical conductivity fraction of each alloy system relative to that of pure Al can be plotted. Due to the multiple limitations of DFT, this approach was not used to predict the actual electrical conductivity of Al alloys, rather, it was only used as an efficient screening tool for exploring the electrical conductivity trends for binary and ternary Al alloys. The semi-classical approach calculates the electrical conductivity tensor using the Boltzmann transport equations.

$$\sigma_{ij}(\varepsilon) = \frac{1}{N}\sum_{i,k} e^2 \tau_{i,k} \nu_\alpha(i,k) \left(-\frac{\delta(\varepsilon - \varepsilon_{i,k})}{d\varepsilon}\right) \qquad (11)$$

$$\sigma_{ij}(T,\mu) = \int \sigma_{ij}(\varepsilon) \left(-\frac{\delta f_\mu(T,\varepsilon)}{\delta\varepsilon}\right) d\varepsilon \qquad (12)$$

where $f_\mu(T,\varepsilon)$ is the Fermi-Dirac distribution, i and j are tensor indices, e is the electron charge, N is the number of *k-points* sampled, ν is the band velocity, and τ is the relaxation time. VASP assumes a constant τ for charge carriers, which can be set using the RTIME command (in femtoseconds). The first equation is energy-dependent, while the second is a function of temperature T and chemical potential μ[43]. In VASP, the chemical potential is considered to be the same as the Fermi level.

4.2.2 Effect of spatial arrangement on electrical conductivity

Before DFT simulations were performed to predict the electrical conductivity trends of Al-Zn-TM combinations, a sub-set of alloy supercells were modeled to establish the dependence of the placement of alloying elements within the supercell on electrical conductivity. The following face-centered cubic (FCC) supercells listed in Table 1, consisting of 108 atoms (3×3×3 unit cells) were constructed. For each alloy system (except pure Al) two supercells were constructed, one with clustered alloying elements, and another with dispersed alloying elements. For example, Figure 19 shows the cluster and disperse supercells for the $Al_{106}ZnZr$ alloy system. For the cluster configuration, the two

atoms of the alloying elements were placed at the face center and corner lattice positions in a single FCC unit cell within the supercell (first neighbor positions). In the disperse configuration, an atom of the first alloying element was placed at the eight (8) corners of the super cell (amounting to 1 solute atom/supercell), while an atom of the second alloying element was placed within the supercell. These models represent ~0.926 at. % of each solute atom. This composition is well above practical solid solubility limit of most transition metals (Figure 18) which have solubility limits that are $\ll 1\ at.\%$ in aluminum. However, larger DFT supercells would need to be constructed to get lower concentration levels of solute atoms, which would become prohibitively time-consuming considering the large number of systems considered in this study.

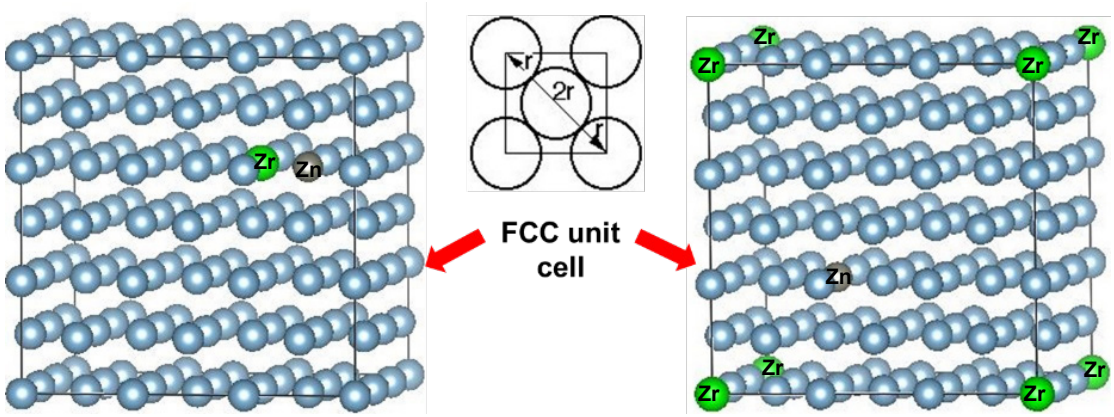

Figure 19. Clustered (left) vs disperse (right) supercell structures, consisting of aluminum (Blue atoms), Zn (grey atoms) and Zr (green atoms). Each supercell has a size of 3x3x3 FCC unit cells consisting of 108 atoms.

The electrical conductivity (MS/m) tensor was calculated for each alloy system using the VASP command "LOPTICS = .TRUE.". The Methfessel-Paxton method (of order 1) was used for smoothing of the energy bands. The energy cutoff was set to 550 eV, while the Brillouin zone sampling was performed using 6 x 6 x 6 k-point Γ-centered Monkhorst-Pack mesh. Table 1 shows the predicted electrical conductivities with respect to the Al_{108}

system for each of the alloy system in the cluster and disperse configurations. In the table, the electrical conductivity of pure Al was normalized to 1. Electrical conductivities of the ternary alloy systems were also normalized as a fraction of the electrical conductivity of pure Al. Hence, σ_C and σ_D are the normalized values, with no unit. The lattice constant included in the Table 1 is the length of the simulation cell after relaxation.

From these data, it is clear that the clustered systems demonstrated a slightly higher electrical conductivity relative to the dispersed systems in all the alloy systems simulated. Due to the difference between the atomic radii of Al and the solute atoms, the distribution of alloying elements within the matrix generated multiple lattice strains and distortions that served as scattering sites for electrons. This was responsible for hindering electron mobility and reducing electrical conductivity. Therefore, when the alloying elements were clustered, the electron scattering sites were localized and thus reduced in number density relative to the disperse configuration. This could be responsible for their slightly higher electrical conductivities relative to their corresponding disperse systems. Since there was no significant change in free energy per atom, between both configurations in all alloy systems considered, the choice of using the clustered configurations for all remaining supercell calculations in this study was made for consistency purposes.

Table 1. Comparison of electrical conductivity and energy per atom in dispersed and clustered Al alloy systems. The percent increase in conductivity is also listed.

	σ_D fraction	E_D/atom (Disperse) (eV/atom)	Lattice constant (Disperse) (Å)	σ_C fraction	E_C/atom (Cluster) (eV/atom)	Lattice constant (Cluster) (Å)	%σ increase
Al_{108}	1.00	-3.76	12.0637	1.00	-3.76	12.0637	-
$Al_{106}Ni_2$	0.43	-3.825	12.0062	0.50	-3.825	12.0461	16.3
$Al_{106}Zr_2$	0.23	-3.900	12.1042	0.25	-3.897	12.0995	8.7
$Al_{106}Zn_2$	0.78	-3.709	12.0786	0.86	-3.709	12.0668	10.3
$Al_{106}ZnZr$	0.33	-3.804	12.0761	0.34	-3.804	12.1097	3.0
$Al_{106}ZnTi$	0.32	-3.786	12.0549	0.33	-3.785	12.0586	3.1
$Al_{106}ZnHf$	0.34	-3.825	12.0764	0.36	3.825	12.0771	5.9
$Al_{106}ZnV$	0.27	-3.772	12.0442	0.28	-3.771	12.0462	3.7
$Al_{106}ZnTa$	0.30	-3.828	12.0611	0.31	-3.821	12.0534	3.3
$Al_{106}ZnCr$	0.26	-3.789	12.0442	0.28	-3.789	12.0483	7.7
$Al_{106}ZnCo$	0.40	-3.765	12.012	0.43	-3.765	12.0262	7.5
$Al_{106}ZnNi$	0.49	-3.767	12.0331	0.55	-3.767	12.0353	12.2
$Al_{106}ZnCd$	0.74	1.913	12.0431	0.78	-1.913	12.0431	5.4
$Al_{106}NiZr$	0.23	-3.861	12.0325	0.27	-3.861	12.0664	17.4
$Al_{106}MgSi$	0.64	-3.879	12.0624	0.65	-3.879	12.0774	1.6

- Conductivity of each configuration is a fraction of bulk aluminum supercell (108 atoms)
- σ_D and σ_C are normalized conductivities of disperse and cluster configurations, respectively
- E_D/atom and E_C/atom are the free energy per atom of disperse and cluster configurations, respectively

4.2.3 Pattern of electrical conductivity across transition elements

DFT simulations of FCC supercells of 108 atoms were constructed for a series of Al-TM binary systems to determine how the individual TMs affect the electrical conductivity in Al-TM binary systems. This information was important for validating the modeling with the experimental data[13]. Each system consisted of 107 atoms of aluminum and 1 atom (approx. 0.926 at. %) of TM. The same simulation parameters as described in the previous sub-section were used to predict the electrical conductivities of each alloy system. In

Figure 20, the electrical conductivities for a series of Al-TM systems are plotted with respect to pure aluminum (thus, the electrical conductivity of pure aluminum is normalized to 1, while those of Al-TM systems are expressed as fractions). Also shown in the figure are two sets of room temperature experimental values, based on the data in Figure 18. The series labeled as "expt-PPT" represents the true experimental result; it considers the effect of precipitation on conductivity once the maximum solubility limit of each transition metal in aluminum has been exceeded. The series "expt-SS" is the extrapolation of the data showing the decrease in conductivity per atomic percent of each transition metal in solid solution with aluminum according to Hatch[13]. The extrapolation of expt-SS ignores the solvus line (precipitation) effect on electrical conductivity, which is consistent with the execution of the DFT simulations. The trend of electrical conductivities computed using DFT agrees well with the experimental data (expt-SS) when precipitation is not considered, and all solutes are assumed to remain in solid solution. The same cannot be said about expt-PPT. This is expected, because DFT simulations does not consider precipitation effects on electrical conductivity. However, similar to expt-SS and DFT curves, the expt-PPT data also shows an overall downward trend for the electrical conductivities of the Al-TM systems considered, though at a higher fraction of aluminum conductivity. Therefore, the overall electrical conductivity reduction observed for expt-PPT is lower than expt-SS. The lower conductivity reduction observed in expt-PPT is because once the composition of the solute atoms exceeds the solubility limit, the solute atoms that form precipitates do not degrade the conductivity as much as when in solution. Ni, Fe and Zr have a much higher electrical conductivity fraction for expt-PPT relative to expt-SS relative to Zn, Cu, V, Cr, Ti and Mn (Figure 20). This is because these elements have very small at.% solid solubility limit in aluminum, Figure 18. Therefore, the precipitation effect on their electrical conductivity values is more dominant since the majority of these solutes will precipitate out of solution.

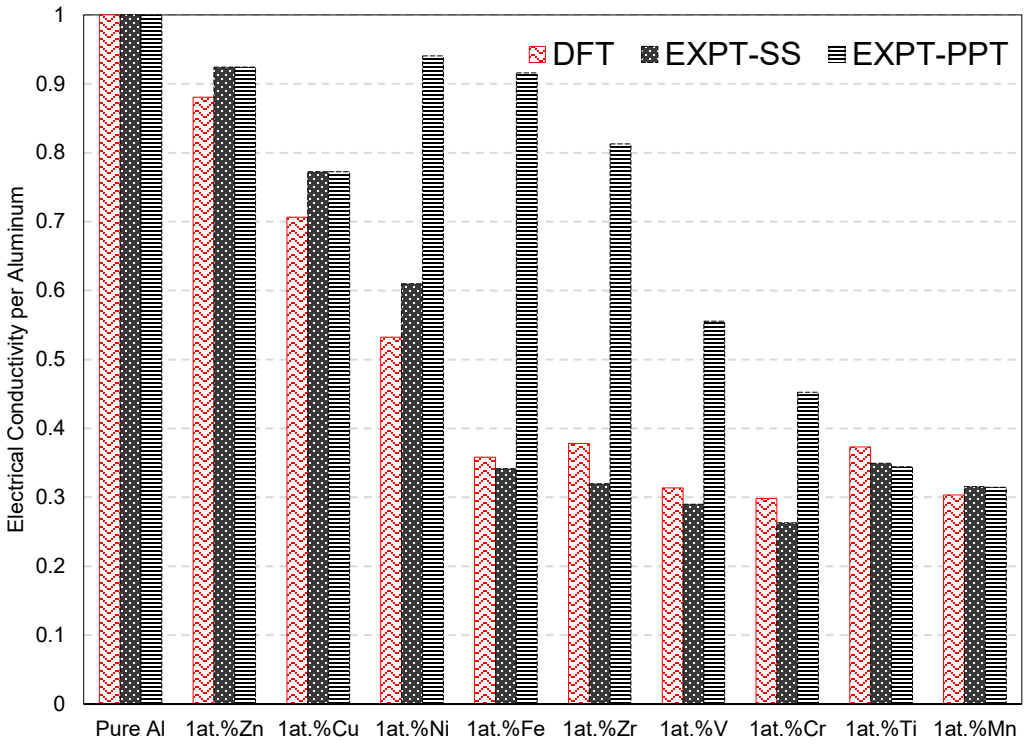

Figure 20. Comparison of electrical conductivity trends between experiment (precipitation and pure solid solution) and DFT. Except for pure Al, the alloy composition for each data point is Al-0.926 at. % TM.

After confirming modeling and experimental agreement in binary systems, fcc supercells (108 atoms) for a series of Al-Zn-TM ternary systems (TM = Sc, Y, Ti, Zr, Hf, V, Nb, Ta, Cr, Mo, W, Mn, Tc, Re, Fe, Ru, Os, Co, Rh, Ir, Ni, Cu, Ag, Au, Zn, Cd, Hg) were constructed and their electrical conductivities were predicted (Figure 21). Each system consisted of 106 atoms of Al and 1 atom each (approx. 0.926 at. %) of Zn and TM. The electrical conductivities are represented in bar chart format so that the overall trend of alloy conductivities within groups and across rows of the periodic table can be compared directly. According to the results shown in Figure 21, the predicted electrical conductivities show little change down each group from IIIB to VIIB, and a significant decrease down each of the groups VIII, IB, and IIB.

The DFT electrical conductivity trend of selected ternary alloys was compared to that of previous binary alloy data in Figure 20, to examine how including a third element (Zn) would alter the electrical conductivity trend of the binary alloys. According to Figure 22, the addition of Zn to binary Al-TM alloys to form ternary Al-Zn-TM showed similar electrical conductivity trends with slightly lesser values. The similarity between electrical conductivity values of Al-TM and Al-Zn-TM indicates that the addition of 1 at.% Zn to the binary Al-TM systems does not have significant negative impact on the electrical conductivities of the alloys. This agrees with the experimental observations shown in Figure 18.

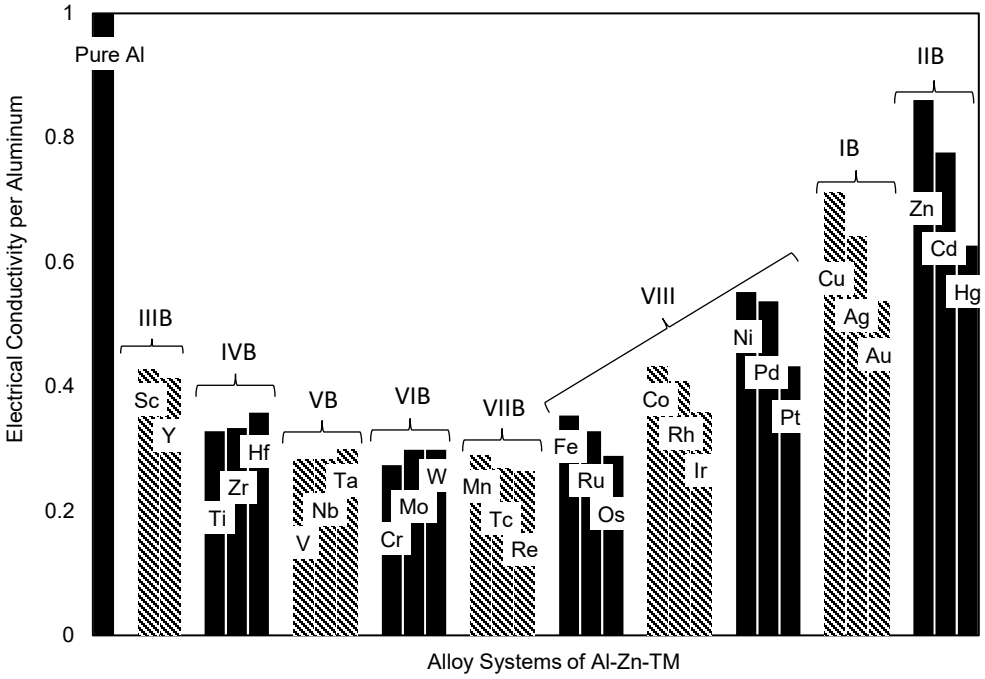

Figure 21. Electrical conductivity per aluminum of Al-Zn-TM formed across transition metals in the periodic table. Each block of solid and stripe pattern represents a group of transition metals.

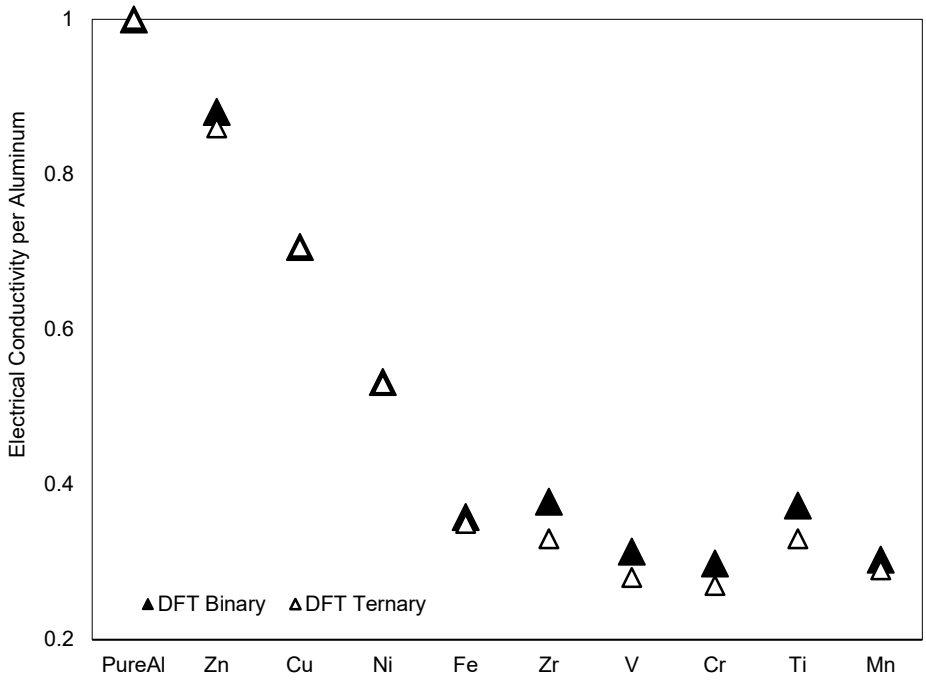

Figure 22. Comparison of the DFT electrical conductivity between binary Al-TM and ternary Al-Zn-TM. Except for pure Al, the alloy composition for each data point is Al-0.926 at.% TM for binary systems and Al-0.926 at.% Zn-0.926 at.% TM for ternary.

From Figure 21, the conductivities can be ranked in order from the highest to lowest as TM = Zn, Cd, Cu, Ag, Hg, Ni, Pd, Au, Co, Pt, Sc, Y, Rh, Ir, Hf, Fe, and Zr (there are still more elements with lower conductivity in Figure 21). In order to down-select TM candidates for further industrial development and commercial use, several factors were considered. First, considering alloy costs in the Al-Zn-TM alloy, relatively expensive elements such as Ag, Pd, Au, Pt, Sc, Rh and Ir were eliminated from consideration. Second, the avoidance of toxicity during fabrication is important, which eliminated Cd and Hg from consideration. Third, elements that do not aid the formation of $L1_2$ precipitate structure in Al-Zn-TM alloys, such as Cu and Co[44, 45], were not considered. Finally, TM = Fe usually does solutionize for subsequent precipitation, and was thus eliminated from consideration. Therefore, the only remaining transition metal candidates considered further were TM =

Ni, Zr, Y and Hf; and from these Ni and Zr were selected for this study because of their lower cost.

4.2.4 Equilibrium precipitate phase of alloy systems

The equilibrium phase structures of Al-Zn-Zr and Al-Zn-Ni aluminum alloy precipitates were investigated with DFT. The DFT approach was first used to simulate the most stable forms (unit cells) of pure Al, Zn, Ni, and Zr to determine their free energy per atom values. The unit cells from these models are shown in Figure 23.

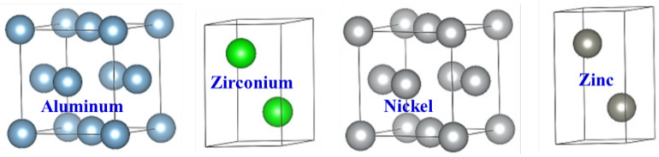

Figure 23. The most stable structures of pure Al (FCC), Zr (HCP), Ni (FCC), and Zn (HCP) from DFT simulation

Figure 24 shows the standard unit cells for the $L1_2$, $D0_{11}$, $D0_{22}$, and $D0_{23}$ structures. Because the $L1_2$ and $D0_{22}$ unit cells have fewer atoms than the $D0_{11}$ and $D0_{23}$ structures, they were scaled up to 16 atoms for direct comparison. Specifically, 1×1×4 and 1×1×2 arrays of $L1_2$ and $D0_{22}$ unit cells, respectively, were used to create supercells with 16 atoms each, to match the size of the $D0_{11}$ and $D0_{23}$ unit cells. For each simulation, an optimized plane-wave cutoff energy of 550 eV was used. Γ-centered Monkhorst-Pack grids were generated and optimized for each structure using the automatic mesh generation scheme implemented in VASP. Partial occupancies for each wavefunction were set using the method of Methfessel-Paxton as implemented in VASP. $D0_{23}$, $D0_{22}$ and $L1_2$ crystal structures were considered for both Al-Zn-Ni and Al-Zn-Zr alloy systems while orthorhombic $D0_{11}$ (which is the initial stable crystal structure of Al_3Ni prior to addition of Zn atoms) was considered only for the Al-Zn-Ni alloy.

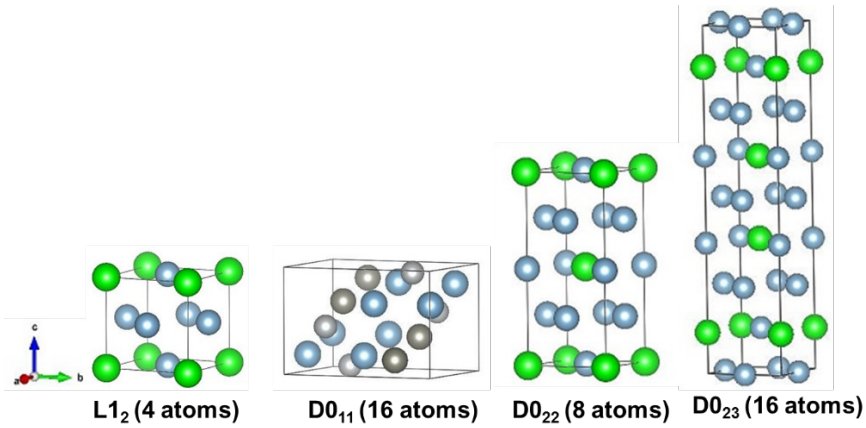

Figure 24. The unit cells of possible stable precipitates, consisting of aluminum (Blue atoms), Zn (grey atoms) and Zr (green atoms). $L1_2$ precipitate structure forms a coherent precipitate within the aluminum matrix, due to similarity in crystal structures and lattice parameters.

In order to determine the relative stability of the $L1_2$, $D0_{11}$, $D0_{22}$, and $D0_{23}$ phases for each Zn level in both systems, the enthalpy of formation at 0K was determined from the energy per atom (energy/atom) values obtained from DFT simulations and the equation:

$$\Delta H(Al-Zn-TM) = E(Al-Zn-TM) - aE(Al) - bE(Zn) - cE(TM) \qquad (13)$$

where ΔH is the enthalpy of formation; *E(Al-Zn-TM), E(Al), E(Zn)* and *E(TM)* are the energies per atom of the intermetallic compound, Al, Zn, and TM, respectively; and a, b and c are mole fractions of the corresponding elements. Each species was relaxed to its equilibrium geometry at zero pressure in the DFT simulations. The enthalpy of formation values for the Al-Zn-Ni and Al-Zn-Zr alloy systems are shown in Figure 25 and Figure 26 respectively, wherein the structure with the lowest enthalpy of formation for a given concentration of Zn is the most stable.

From Figure 25 it is apparent that the lowest energy structure of the Al_3Ni precipitate in the Al-Ni binary matrix is $D0_{11}$, which is incoherent with the matrix. However, there is a possibility of forming a $L1_2$ precipitate by replacing aluminum atoms in the precipitate

structure with Zn atoms. Figure 25 shows that transformation of the $D0_{11}$ structure of Al_3Ni trialuminide to $D0_{23}$ occurs for very low Zn concentrations, and the subsequent transformation to $L1_2$ occurs at approximately 0.17 atomic fraction of Zn (assuming a linear interpolation between data points). The $L1_2$ crystal structure continues to be most probable for Zn concentrations up to 0.5, at which point the $D0_{22}$ phase has a nearly equal enthalpy of formation. Similarly, from Figure 26, the initial Al_3Zr precipitate phase has a theoretical equilibrium $D0_{23}$ crystal structure even though experimentally it has been observed that during heat treatment, the Al_3Zr precipitates formed assume a metastable $L1_2$ structure at temperature < 475 ℃[30]. At a Zn concentration of about ≥ 0.04, the lowest enthalpy of formation and crystal structure of the intermetallic becomes $L1_2$, which remains the most stable and equilibrium structure for higher Zn concentrations as shown in the graph[14]. Thus, it is evident from the simulations that the $Al_{3-x}Zn_xNi$ and $Al_{3-x}Zn_xZr$ precipitates formed in Al-Zn-Ni and Al-Zn-Zr alloy systems respectively, have a coherent $L1_2$ structure, necessary for more effective material strengthening.

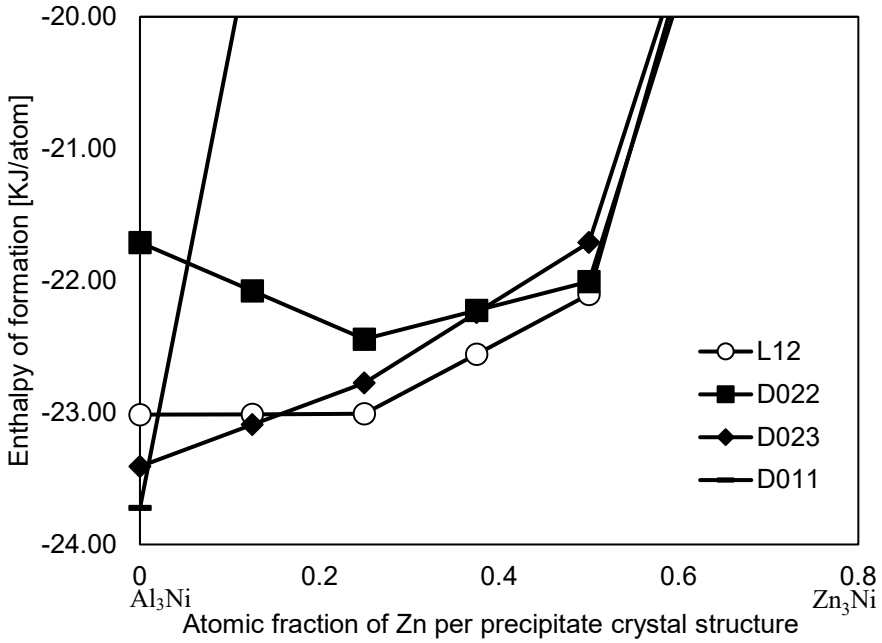

Figure 25. Enthalpy of formation of the Al-Zn-Ni alloy system. The $L1_2$ crystal structure becomes most stable at 0.17 atomic fraction of Zn.

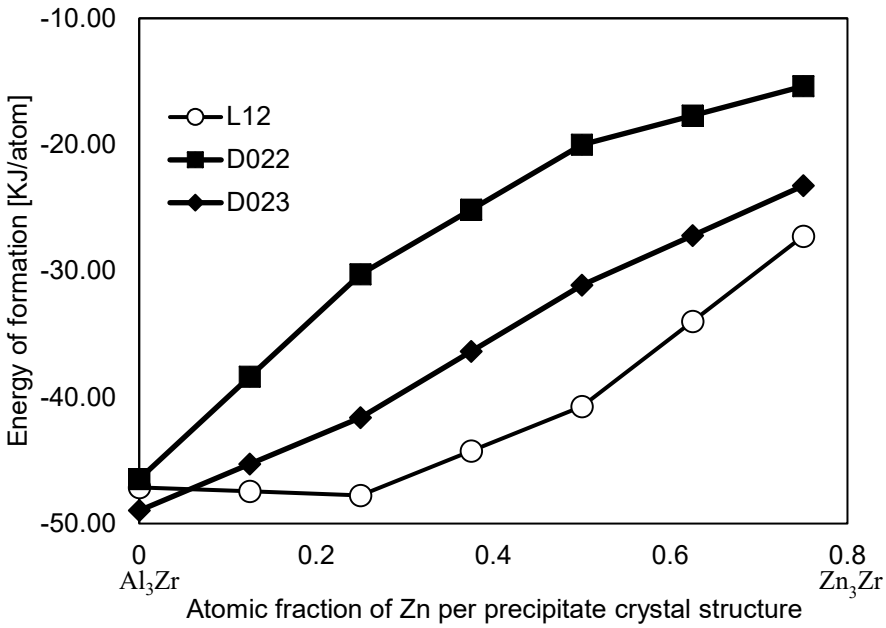

Figure 26. Enthalpy of formation of the Al-Zn-Zr alloy system. The $L1_2$ crystal structure becomes most stable at a 0.04 atomic fraction of Zn.

4.3 Experimental methods

Based on the electrical conductivity and thermodynamic phase stability results from DFT computational simulation discussed above, Al-Zn-Ni and Al-Zn-Zr alloys were identified as having moderate to high conductivities and the ability to form $L1_2$ precipitate structure necessary for improved strength. Additionally, compared to other Al-Zn-TM alloys, Ni and Zr were expected to be inexpensive, not involve any toxic metals, have low diffusivity, and be highly castable. The next step in the ICME process was to fabricate samples of the Al-Zn-Ni and Al-Zn-Zr systems for characterization and mechanical and electrical testing. In this section, the fabrication and testing procedures are described, and the test results for Al-Zn-Ni and Al-Zn-Zr are compared.

4.3.1 Fabrication and testing of Al-Zn-Ni and Al-Zn-Zr

Four different 600-gram ingots of Al-Zn-Ni and two 600-gram ingots of Al-Zn-Zr alloys were fabricated from 99.99 wt.% purity aluminum, Al–20 wt.% Ni and Al–5 wt.% Zr master alloys, and 99.99 wt.% purity Zn ingots in a vacuum induction melter (VIM). Measured quantities of each component were arranged inside a graphite crucible within the VIM chamber. A vacuum pressure of 7.8×10^{-5} Torr was obtained inside the chamber through the use of a diffusion pump to minimize reactive gases before partially backfilling to 558 Torr with 99.999 wt.% Ar gas. The temperature (measured by an optical pyrometer above the crucible) was gradually ramped to 710 ℃, thereby melting the components inside the crucible. The target and nominal compositions of the alloys are listed in Table 2. Small size buttons were cut out of the 19 mm diameter rods of each ingot and their compositions measured using Inductively Coupled Plasma Optical Emission Spectroscopy (ICP-OES). The small buttons from the ingots were polished for optical metallography using 180, 320, 600 and 1500 silicon carbide paper grit followed by 6 μm diamond, 1 μm diamond, and a 0.04 μm silica solutions polishing pads.

Solid solution heat treatments were performed on the Al-Zn-Ni samples for 4 hours at 620 ℃, within the single phase region so as to homogenize the Ni solute, before quenching in cold water. Without prior homogenization of Al-Zn-Ni specimens, a microhardness increase was not observed during aging. The Al-Zn-Zr alloys were not homogenized because prior homogenization of Al-Zr alloy first nucleates primary Al_3Zr precipitates. This reduces the amount of Zr solute left in solid solution for subsequent aging, thereby leading to a corresponding lower peak microhardness from precipitation hardening[33]. A series of multi-step isochronal aging experiments were carried out on the alloy buttons from 150 to 400 $°C$ at 50 $°C$ temperature steps and 150 to 600 $°C$ at 50 $°C$ temperature steps for Al-Zn-Ni and Al-Zn-Zr, respectively. The duration for each temperature step was 3 h in the furnace before quenching in water.

Vickers microhardness measurements were performed on the mechanically polished surface at every temperature step, with a load of 50 g and dwell time of 15 s. A calibrated

Sigmascope SMP10 probe was used for electrical conductivity measurements of each button specimen.

4.3.2 TEM analysis

For TEM analysis, thin foils (200 μm thickness) were cut out from samples of 0.5Zn0.05Ni, 1.0Zn0.05Ni, 1.8Zn0.05Ni and 1.7Zn0.07Zr. These foils were then mechanically polished down to < 100 μm. An FTS System Multicool chiller connected to the Jet Electropolisher was used to maintain the temperature of 150 ml methanol and 60 ml nitric acid mixture (electrolyte) at -35 $°C$ before electropolishing was performed on the samples at 10 V (~ 70 mA). The TEM imaging used an FEI Titan Themis Scanning-Transmission Electron Microscopy (S-TEM) operating at 200 kV. Energy Dispersive X-ray Spectroscopy (EDX) analysis was performed on the samples with the use of Bruker software.

Table 2. Sample labels and composition in at.% (ICP OES)

Sample Label	Al	Target Zn	Actual Zn	Target Ni	Actual Ni	Target Zr	Actual Zr
0.5Zn0.05Ni	Bal	0.5	0.51	0.05	0.05	-	-
1.0Zn0.05Ni	Bal	1.0	1.02	0.05	0.04	-	-
1.8Zn0.05Ni	Bal	1.5	1.80	0.05	0.07	-	-
0.5Zn0.10Ni	Bal	0.5	0.50	0.1	0.08	-	-
1.0Zn0.07Zr	Bal	1.0	1.00	-	-	0.075	0.06
1.7Zn0.07Zr	Bal	1.5	1.70	-	-	0.075	0.06

4.4 Experimental results

The results obtained from the experiments described in Section 4 for the two material systems identified in Section 3 are presented below. The Al-Zn-Ni system is reported first followed by the Al-Zn-Zr system.

4.4.1 Multi-step isochronal aging of Al-Zn-Ni

Figure 27 shows the conductivity and microhardness of multi-step isochronally aged Al-Zn-Ni with 50 $°C$ temperature steps. The peak microhardness values of all the Al-Zn-Ni alloys were observed at an aging temperature of 250 $°C$. Alloys 0.5Zn0.05Ni and 1.8Zn0.05Ni have similar Ni compositions but different Zn levels (see Table 2 for exact composition). An increase of Zn composition from 0.5 to 1.8 at.% improved the alloy microhardness at all aging temperatures. The peak microhardness achieved for 0.5Zn0.05Ni, 1.0Zn0.05Ni, 1.8Zn0.05Ni, and 0.5Zn0.1Ni were 337, 341, 376 and 328 MPa respectively. The average increase in microhardness due to precipitation of Al-Zn-Ni system is approx. 28%. Comparison of 0.5Zn0.05Ni and 0.5Zn0.1Ni, which have the same Zn level but different Ni content (Table 2), indicates that increasing Ni from 0.05 to 0.08 at.% yields a slightly higher microhardness in the as-solutionized state but reduces the peak microhardness at 250 $°C$. Beyond 250 $°C$, the microhardness of all Al-Zn-Ni samples continued to drop until they reached their as-cast/pre-aging microhardness due to over-aging and precipitate dissolution. During over-aging, precipitate mean size increases as a result of growth and subsequent coarsening also known as Ostwald Ripening. This increases the edge-to-edge precipitate spacing, thereby allowing dislocations to move more freely between precipitates.

An increase in Zn level reduced the conductivity from 35.1 (0.5Zn0.05Ni) to 32.3 MS/m (1.8Zn0.05Ni) mostly due to the presence of more Zn solute in solid solution. The effect of increasing Ni composition from 0.05 at.% (0.5Zn0.05Ni) to 0.08 at.% (0.5Zn0.1Ni) on conductivity is negligible (they are both approximately 35.1 MS/m) because Ni has a very minimal negative effect on conductivity of aluminum alloys when precipitated out of solution[13]. For all aging temperatures, the conductivities of Al-Zn-Ni alloys remained almost constant.

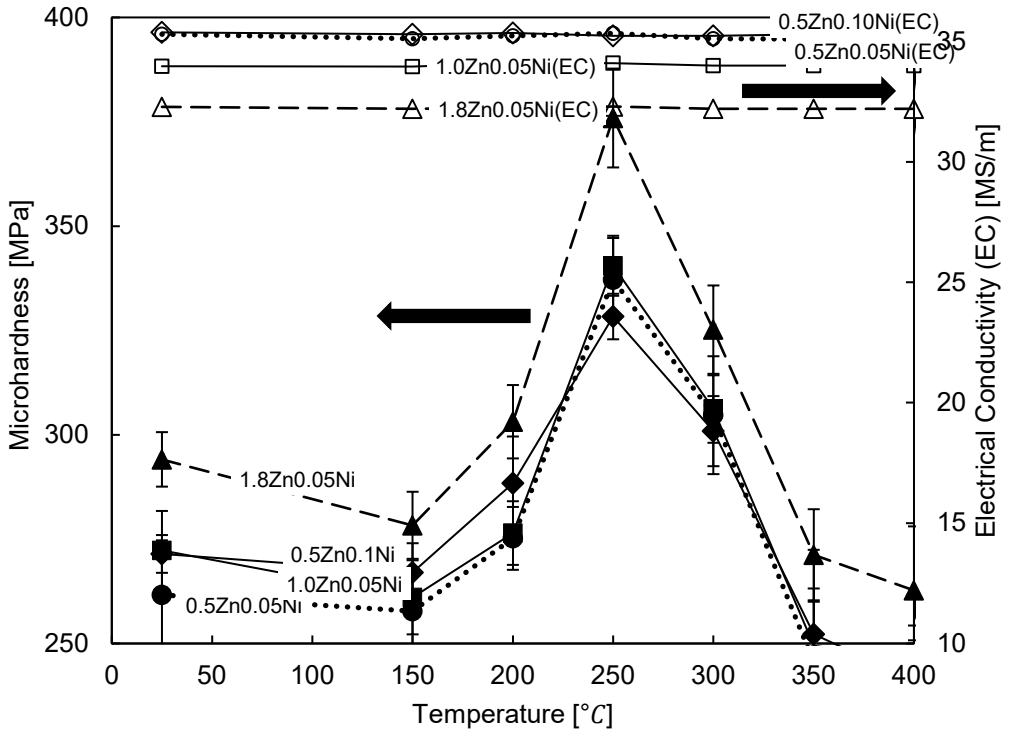

Figure 27. Conductivity and microhardness of Al-Zn-Ni as a function of aging temperature for a 3 h multi-step isochronal annealing with temperature increments of 50 °C.

4.4.2 Multi-step isochronal aging of Al-Zn-Zr

Results from isochronal aging of homogenized Al-Zn-Zr samples are shown in Figure 28. The purpose was to observe the peak microhardness, the aging temperature at which peak microhardness occurs, and the conductivity of the Al-Zn-Zr alloys; and to compare these values to those of the Al-Zn-Ni alloys. In this alloy system, peak microhardness occurs at 450 °C, which is 200 °C higher than that of Al-Zn-Ni. The increase in Zn composition increased the peak microhardness while reducing the electrical conductivity. The 1.0Zn0.07Zr and 1.7Zn0.07Zr systems have peak microhardness values of 441 and 458 MPa, while their conductivities are 31.8 MS/m and 30.1 MS/m, respectively. The similar microhardness difference between both alloys at as-cast (14 MPa) and peak-aged condition (17 MPa) indicates mostly solid solution strengthening from the excess Zn between them. Hence, increasing Zn composition does not increase precipitate volume fraction. The

microhardness values of Al-Zn-Zr are much higher than the equivalent composition of Al-Zn-Ni alloys. However, they have lower electrical conductivities than Al-Zn-Ni. For instance, 1.7Zn0.07Zr (Al–1.7 at.% Zn–0.06 at.% Zr) has a peak microhardness of 458 MPa and conductivity of 30.1 MS/m at approximately 450 °C (Figure 28), compared to 376 MPa and 32.2 MS/m in 1.8Zn0.05Ni (Al–1.8 at.% Zn–0.07 at.% Ni) at 250 °C (Figure 27). Even though 1.7Zn0.07Zr has similar at.% of Zn and Zr to the compositions of Zn and Ni in 1.8Zn0.05Ni. The peak conductivity occurred at ~475 °C due to the precipitation of solutes out of solution. The subsequent reduction in conductivity after the peak condition is due to the precipitate coarsening and dissolution as the aging temperature continued to increase. Similarly, over-aging leads to the strength reduction of Al-Zn-Zr alloys to their as-cast microhardness due to coarsening.

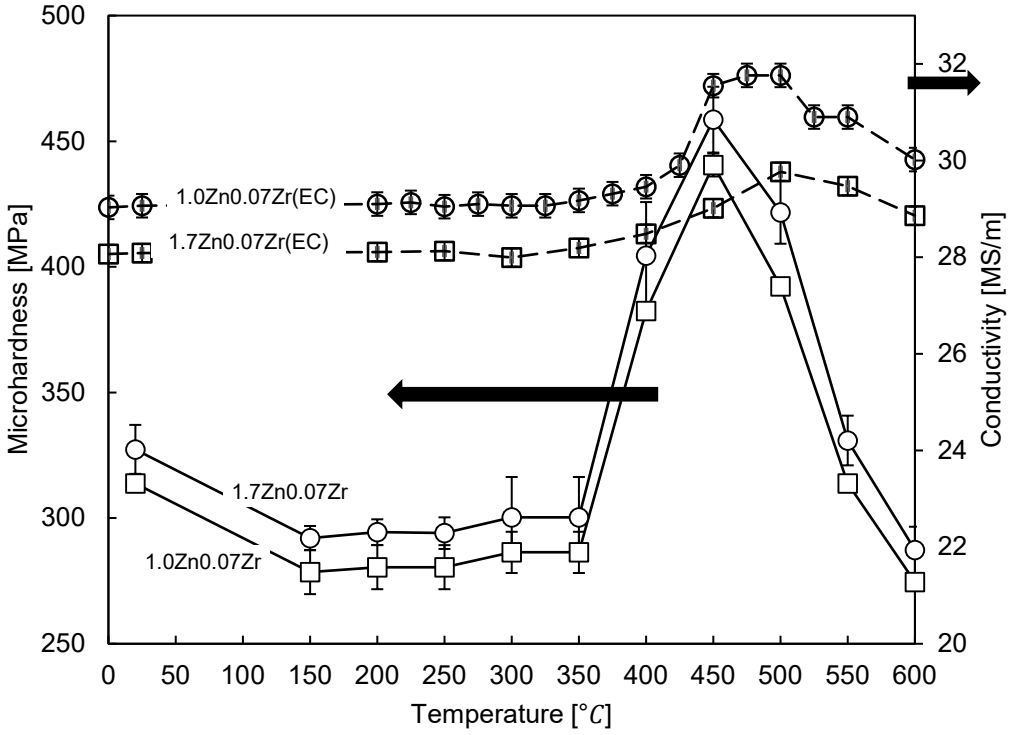

Figure 28. Conductivity and microhardness of Al-Zn-Zr as a function of aging temperature (3 h multi-step isochronal).

4.4.3 TEM study of Al-Zn-Ni

The small precipitates formed in 0.5Zn0.05Ni, 1.0Zn0.05Ni and 1.8Zn0.05Ni specimens after aging at 250 $°C$ have a mean size of $\leq 10\ nm$. The orientation of these uniformly distributed particles, present in 0.5Zn0.05Ni and 1.0Zn0.05Ni is along the longitudinal section (needle-like), Figure 29[a] & [b]. However, coherent spheroidal particles, (Figure 29[c]), were present in the 1.8Zn0.05Ni specimen, which has higher Zn solute. The precipitate/matrix coherency in 1.8Zn0.05Ni is indicated by the Ashby-Brown strain contrast. The diffraction patterns acquired from the Al-Zn-Ni specimens at 250 $°C$ showed no ordered superlattice spots that could be attributed to the precipitate phase. Only fcc planes were observed. Since the miscibility gap where 2-FCC phases coexists only occurs at $>$ 14 at.% Zn and $>$ 280°C in the Al-Zn binary phase diagram, the precipitates can not be said to have FCC structure. Hence, the reason for the invisible superlattice spots could be attributed to a combination of the small size and volume fraction of the precipitates. It was difficult to acquire the lattice image of the needle-like and spheroidal-like precipitates formed in Al-Zn-Ni at 250°C. Hence, the structure of the precipitates could also not be determined by observing the atomic positions and lattice parameter.

To increase the likelihood of detecting the precipitate phase structure from the diffraction pattern, the beam was converged on the large precipitate formed in the overaged specimens after aging at 400 $°C$. Specifically, needle-like precipitates were found in the 0.5Zn0.05Ni and 1.0Zn0.05Ni specimens (Figure 29[d] & [e]). The diffraction pattern along the z[100] indicates that these precipitates have a $D0_{11}$ structure, which is the typical crystal structure of Al_3Ni. Precipitates formed in 1.8Zn0.05Ni maintained spheroidal morphology at an overaged temperature, Figure 29[f], with a slightly visible line of no contrast. The $(00\bar{1})$ and $(01\bar{1})$ superlattice spots present in the SAED acquired along z[100] show that these spheroidal particles most likely have $L1_2$ precipitate structure. The precipitate volume fraction could be said to be responsible for the low intensity of the superlattice spot.

EDX chemical composition analysis indicates that the 0.5Zn0.05Ni and 1.0Zn0.05Ni specimens have no Zn species present in their precipitate phases, while the spheroidal particles in 1.8Zn0.05Ni are rich in Zn. When the electron beam was converged on just the

matrix region versus a single precipitate, the EDX data showed that all the Ni species were contained in the precipitate phase; no Ni was present in the matrix. Quantitatively, 0.5Zn0.05Ni and 1.0Zn0.05Ni alloys are likely to have a precipitate stoichiometry of Al_3Ni. However, since there was a measurable amount of Zn present in the precipitates formed in 1.8Zn0.05Ni, they are presumed to have the form $Al_{3-x}Zn_xNi$[34]. The composition of the precipitates and matrix of Al-Zn-Ni alloys are summarized in Table 3.

At 400 $°C$, the average length of the needlelike particles in 0.5Zn0.05Ni and 1.0Zn0.05Ni is between 60 and 250 nm, while the average interparticle spacing for both alloys varies from 80 to 400 nm, Figure 29[d] & [e]. From observation, increasing the composition of Zn from 0.5 to 1.0 at.% translated into bigger mean precipitate size in 1.0Zn0.05Ni relative to 0.5Zn0.05Ni. The overaged spheroidal precipitates formed in 1.8Zn0.05Ni have a mean particle diameter of 25 nm as shown in Figure 29[f].

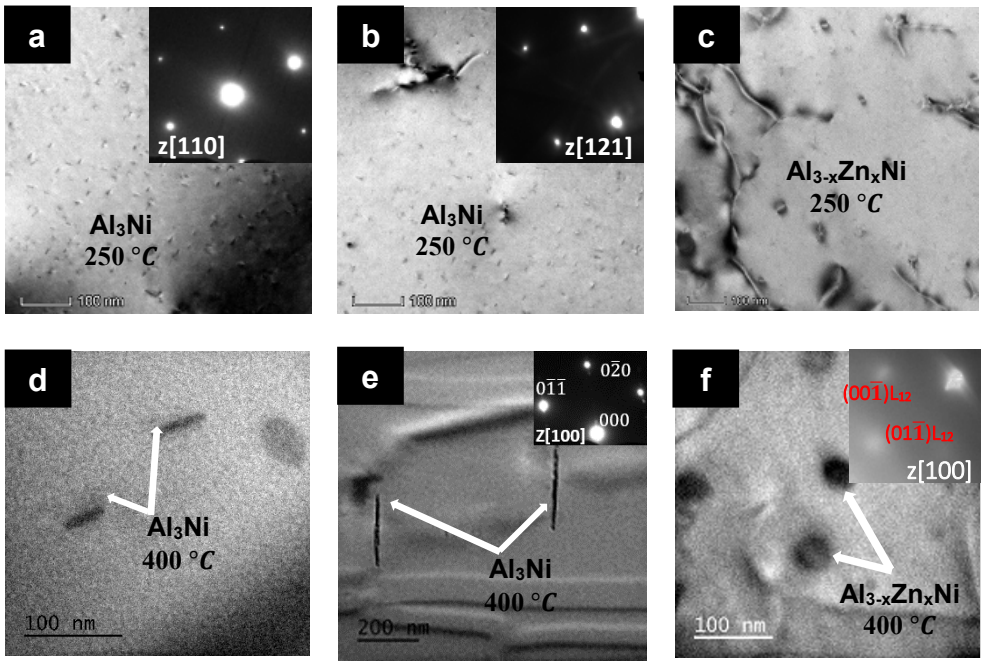

Figure 29. TEM images showing the microstructures of precipitates formed in Al-Zn-Ni alloy specimens at 250 and 400 $°C$, (a & d) 0.51 at. % Zn, (b & e) 1.02 at. % Zn and (c & f) 1.8 at.% Zn. TEM images of the overaged specimens were observed along the [100] zone axis. The observed phase structures of the precipitates are $D0_{11}$ for 0.5Zn0.05Ni and 1.0Zn0.05Ni, and possibly coherent $L1_2$ for 1.8Zn0.05Ni, however, the very low intensity of the superlattice spot due to precipitate volume fraction makes this inconclusive.

4.4.4 TEM study of Al-Zn-Zr

The microstructure and diffraction patterns (matrix and precipitate) of the 1.7Zn0.07Zr Al alloy isochronally peak-aged at 450 $°C$ were observed under TEM. Figure 30[a & b] shows a high and low number density of precipitates with spheroidal morphology dispersed in the dendritic center and interdendritic channel, respectively. There was a lateral gradient of precipitate sizes from the dendritic center toward the interdendritic channel of the specimen. A similar mean size gradient has been reported for Al-Zr alloys[30]. The particles present in the dendritic center have a mean diameter of $< 5\ nm$, while those in the interdendritic channels are bigger in size, with a mean diameter of ~17 nm and inter-particle spacing of 80 – 100 nm. The Ashby-Brown strain contrast in Figure 30[c] indicates precipitate/matrix coherency. From the SAED, it was observed that in addition to the

expected fcc planes such as $(\bar{2}20)$ and $(\bar{3}13)$, there are other smaller superlattice spots that are attributed to the presence of $L1_2$ – $\{110\}$ planes. These indicate that the precipitates formed in Al-Zn-Zr have $L1_2$ crystal structure. The TEM images of this specimen were collected along [332] zone axis. Other diffraction patterns along low index zone axes [111] and [110] (not included in this paper) were collected, further showing that the $Al_{3-x}Zn_xZr$ precipitate phase is $L1_2$.

EDX data obtained when the beam was converged on the matrix or spheroidal precipitate regions of the 1.7Zn0.07Zr system shows that there is a high concentration of Zr in the precipitates phase relative to the matrix. The compositions of the precipitates and matrix are summarized in Table 3. As with the Ni alloy, the matrix had no Zr atoms present.

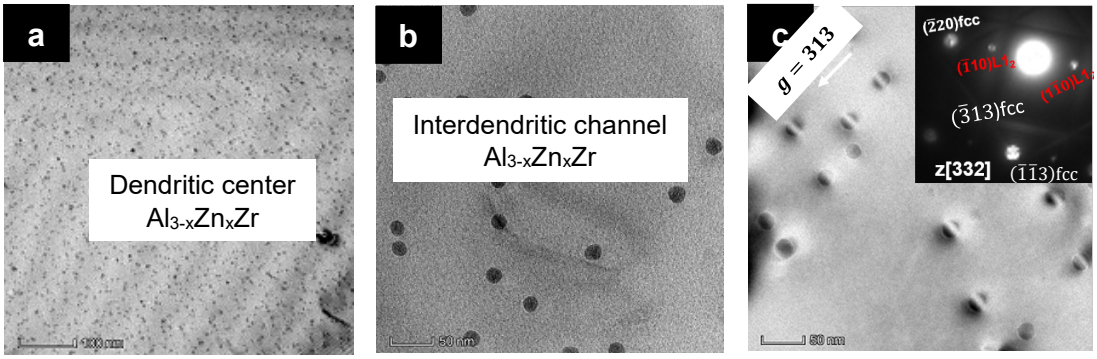

Figure 30. TEM images showing the microstructures and diffraction patterns of 1.7Zn0.07Zr alloys: (a) Small spheroidal $Al_{3-x}Zn_xZr$ precipitates of $< 5\,nm$ diameter formed at the center of the dendrites. (b) At the interdendritic channels, bigger $L1_2$-$Al_{3-x}Zn_xZr$ precipitates of 17 nm diameter were present. (c) Shows the corresponding Ashby-Brown strain contrast of the coherent $Al_{3-x}Zn_xZr$ precipitates within the same interdendritic channel, with the diffraction pattern obtained along [332] zone axis showing the $\{110\}$ plane. This indicates that the precipitate phase has an $L1_2$ ordered lattice structure.

Table 3. Summary of EDX data of Al-Zn-Ni and Al-Zn-Zr (at. %) at peak aged conditions

Specimens		Al	Zn	Ni	Zr
0.5Zn0.05Ni	Precipitate	75.1	-	24.9	-
	Matrix	99.5	0.5	-	-
1.0Z n0.05Ni	Precipitate	75.0	-	25.0	-
	Matrix	99.0	1.0	-	-
1.8Zn0.05Ni	Precipitate	69.3	5.9	24.8	-
	Matrix	98.3	1.7	-	-
1.7Z n0.07Zr	Precipitate	70.1	5.1	-	24.8
	Matrix	99.1	1.6	-	-

4.5 Discussion

4.5.1 Comparing microhardness of Al-Zn-Ni and Al-Zn-Zr

From Figure 27 and Figure 28, the first sign of nucleation occurs after $150\ and\ 350$ ℃ for Al-Zn-Ni and Al-Zn-Zr, respectively. This indicates that the presence of Ni in the Al-Zn-TM alloy decreased the incubation time for precipitate nucleation compared to Zr. As precipitates formed in Al-Zn-Ni nucleate at > 150 ℃, continued increase of aging temperature led to precipitate growth. At 250 ℃, a critical precipitate diameter was reached, and peak microhardness was observed. Between $150\ and\ 250$ ℃, there was no sign of nucleation in the Al-Zn-Zr alloy. The peak microhardness for this alloy was attained after aging up to 450 ℃. The lower peak microhardness temperature observed in Al-Zn-Ni relative to Al-Zn-Zr suggests that the precipitates formed in Al-Zn-Zr are more stable to higher temperatures compared to Al-Zn-Ni. The difference between their peak microhardness temperatures can be attributed to the higher diffusivity of Ni in Al relative to that of Zr in Al at every aging temperature, as shown in Table 4. Precipitation growth is controlled by the diffusion of solute atoms in the solvent at specific aging temperatures. At any particular aging temperature, the diffusivity of the solute atoms in the solvent has a direct influence on the distance covered by the solute from its supersaturated position to

the nearby nucleation site. The higher the diffusivity, the faster the precipitates grow. The diffusivity and diffusion distance of various elements (used in this study) at $250\ and\ 450$ ℃ were estimated by an Arhenius relationship, $D = D_o \exp(-Q/R_g T)$, using their respective activation enthalpy Q and pre-exponential D_o values[29, 33, 46, 47]. For precipitate growth to occur at specific aging temperatures, the solutes would require sufficient heat energy to migrate from their supersaturation position to a nearby nucleation site. In general, the distance traveled by the solutes should be reasonably close to the average interparticle spacing at that aging temperature.

Table 4. Diffusion and distance data for selected transition metal (3d and 4d) solutes in aluminum at 250 and 450 ºC[29].

	Pre-exponential D_o (m^2s^{-1})	Activation Enthalpy, Q (KJ/mol)	D at 250 ºC (m^2s^{-1})	Diffusion distance (nm) at 250 ºC after 3hrs	References
			Self-Diffusion		
Al	1.37×10^{-5}	124	5.64×10^{-18}	349	[48]
			3d and 4d-Transition metals		
Ni	4.4×10^{-4}	146	7.27×10^{-19}	125	[49]
Zn	2.59×10^{-5}	121	2.13×10^{-17}	678	[50]
Zr	7.28×10^{-2}	242	4.92×10^{-26}	0.0325	[47]
	Pre-exponential D_o (m^2s^{-1})	Activation Enthalpy, Q (KJ/mol)	D at 450 ºC (m^2s^{-1})	Diffusion distance (nm) at 450 ºC after 3hrs	References
Zr	7.28×10^{-2}	242	2.38×10^{-19}	72 nm	[47]

After aging at 250 ℃ for 3 h, only Al, Zn, and Ni solute species would cover distances $> 120\ nm$, while Zr would cover only 0.0325 nm. Considering that the average interparticle spacing for 1.8Zn0.05Ni is 80 – 200 nm, the Zn and Ni solutes have sufficient driving force to reach a nearby nucleation site, which leads to precipitate growth. The distance covered by Zr at this temperature makes it unlikely that any $Al_{3-x}Zn_xZr$ precipitate growth would

happen. It also explains why Zr alloys require a higher temperature for the formation and growth of its strengthening phase. Zr atoms move 72 nm after aging at 450 ºC for 3 h (Table 4), which is far enough to reach the nearby precipitate phase, since the interparticle spacing for 1.7Zn0.07Zr is between 10-15 nm (dendritic center) and 20-80 nm (interdendritic channel). Beyond the peak microhardness conditions for both alloys, the precipitates continue to grow and become bigger than the critical size, as more solutes migrate into the precipitate phase. As a result, the precipitates become harder, thereby, requiring more force for dislocations to shear instead of bowing through. The early stage of overaging, at approximately between 250 – 300 ºC (1.8Zn0.05Ni) and 450 – 500 ºC (1.7Zn0.07Zr), is controlled by dislocation bowing (Orowan strengthening). This is followed by precipitate coarsening and dissolution of solutes from the precipitate phase into the matrix at the latter stage of overaging. Here the bigger precipitates grow at the expense of smaller ones. The influence of precipitation on the microhardness of the alloys becomes insignificant at this stage as the hardness of the alloy mostly depends on solid solution strengthening from the dissolved solutes[23]. Hence, the microhardness values of the specimens return to the as-cast microhardness state at 400 and 600 ºC for 1.8Zn0.05Ni and 1.7Zn0.07Zr respectively.

4.5.2 Electrical conductivity

The heat treatment results presented in Figure 27 and Figure 28 also show a consistent reduction in conductivity as Zn composition increases. Since most of the Zn remains in solid solution, the trend of reduced conductivity is due to the increase in local electron scattering sites as a result of the presence of Zn solute atoms within the Al matrix. The increase in conductivity of the Al-Zn-Zr alloys (1.7Zn0.07Zr and 1.0Zn0.07Zr) observed at 475 ºC in Figure 28 is due to the precipitation of the solute atoms out of solution (especially Zr; Figure 18). When in solid solution, alloying elements contribute to the lattice distortion of the matrix and generation of local electron scattering sites, which reduce the mobility of free electrons in the system[51]. The creation of lattice distortion by the solutes in solid solution is driven by the dissimilar atomic radii of the solute and solvent atoms[51]. However, during precipitation, the solute atoms form a secondary phase with a different composition and structure from the matrix, thus reducing their contribution to the

lattice distortion and local electron scattering. Hence, the mobility of free electrons within the system is less hindered, leading to the increased conductivity observed. A similar increase in conductivity was not observed in Al-Zn-Ni alloys as shown in Figure 27. The lower electrical conductivity observed in Al-Zn-Zr (1.0Zn0.07Zr and 1.7Zn0.07Zr) relative to Al-Zn-Ni (1.0Zn0.05Ni and 1.8Zn0.05Ni) is due in large part to the role of Zr in electrical conductivity degradation relative to Ni (Figure 18). Unlike Zr, Zn and Ni do not have a severe impact on the electrical conductivity of aluminum alloy. The more damaging impact of Zr on the electrical conductivity of aluminum, relative to Zn and Ni, was already predicted by the DFT simulation results for Al-TM and Al-Zn-TM shown in Figure 20 and Figure 21.

4.5.3 Microstructure of Al-Zn-Ni and Al-Zn-Zr

For the precipitates of the aged Al-Zn-Ni alloys to transform into the $L1_2$ structure of spheroidal morphology, a critical quantity of Zn must be present in the precipitate phase according to DFT simulation results (Figure 25 and Figure 26). The needle-like morphology of the particles observed in 0.5Zn0.05Ni and 1.0Zn0.05Ni, Figure 29, represents the formation of an Al_3Ni intermetallic. This is supported by EDX chemical composition analysis, which shows that there is no Zn present in the precipitate phase of 0.5Zn0.05Ni and 1.0Zn0.05Ni. The diffraction patterns shown in Figure 29[d] and [e] confirm their precipitate structures as orthorhombic $D0_{11}$. Al_3Ni has a $D0_{11}$, Fe_3C-type cementite structure that has a needlelike particle shape, indicating an orthorhombic crystal structure[52, 53]. From the ternary phase diagram of Al-Zn-Ni, the maximum solubility limits of Zn in aluminum at room temperature and 250 ºC (peak aging) are 0.69 and 10 at.%, respectively[44]. Considering that 0.5Zn0.05Ni and 1.0Zn0.05Ni alloys have 0.51 and 1.02 at.% Zn respectively, these solubility limits are significantly high. Therefore, it is possible that most of the Zn remained in solution after quenching the alloys to room temperature and during subsequent aging. This could explain why the precipitate morphologies were non-$L1_2$ ($D0_{11}$) with no Zn present in the precipitate phase. It is also possible that the excess Zn that precipitated out of solution while aging 1.0Zn0.05Ni diffused into the precipitate phase but was insufficient to transform the precipitate structure

from $D0_{11}$ to coherent $L1_2$, Figure 25. The spheroidal particles shown in Figure 29[c] and [f] for 1.8Zn0.05Ni indicate that there is a sufficient amount of Zn atoms entering the precipitate phase from the saturated solid solution. The presence of these Zn atoms allows for the transformation of the precipitate morphology from Al_3Ni, which has the needlelike – orthorhombic $D0_{11}$ structure[29, 52-54] to $Al_{3-x}Zn_xNi$ (likely spheroidal $L1_2$ phase). However, the structure of $Al_{3-x}Zn_xNi$ present in 1.8Zn0.05Ni could not be confirmed as $L1_2$ by the diffraction pattern shown in Figure 29[c and f] inset, especially at 250°C[55], due to the invisible or low intensity superlattice spot.

As shown in Figure 30, there is a precipitate size gradient observed in 1.7Zn0.07Zr. This size gradient is as a result of the microsegregation of Zr solute in the alloy while solidifying during casting. The Zr solutes segregate into dendritic centers and interdendritic channels[30]. The high concentration of Zr in the dendritic center increases the chemical driving force for precipitate nucleation. Therefore, the critical mean radius for nucleation to occur is reduced and smaller precipitates are formed. For the interdendritic channels, Figure 30[b], the mean precipitate size is bigger due to low Zr solute concentration and lower chemical driving force for nucleation. Similar to the morphology of Al_3Zr precipitates reported in several studies[30, 31], $Al_{3-x}Zn_xZr$ precipitates have a spheroidal form with lines of no contrast perpendicular to $g = 313$ vector, Figure 30[c]. The SAED information obtained along the [332] zone axis shows additional weak {110} superlattice spots, which confirms that the $Al_{3-x}Zn_xZr$ precipitate has an ordered lattice structure corresponding to the $L1_2$ phase. This demonstrates that including Zn into the precipitate phase structure does not alter the metastable $L1_2$ phase structure previously reported for Al_3Zr. Therefore, while attempting to improve the alloy strength with Zn, the $L1_2$ precipitate phase structure and high electrical conductivity were maintained. According to EDX chemical composition analyses, Table 3, the absence of Zr in the matrix indicates that Zr solute atoms precipitated out of solid solution to form coherent $Al_{3-x}Zn_xZr$ precipitates. It also shows that a small fraction of Zn was used up in the precipitate phase.

4.5.4 Estimation of yield strength at peak conditions

According to Figure 27 and Figure 28, the observed maximum yield strength for 1.8Zn0.05Ni and 1.7Zn0.07Zr are ~125 (250 ℃) and ~156 MPa (450 ℃), respectively, using a conversion factor of $\frac{1}{3}$ between Vickers microhardness and yield strength[56]. These observed strengths are due to solid solution and precipitation strengthening mechanisms. Grain size reduction and strain hardening of the specimens were not considered since aging is not expected to have any significant effect on grain size and the specimens were not deformed. The yield strengths of the specimens have contributions from modulus mismatch, order, Orowan, and coherency strengthening mechanisms due to the spheroidal coherent precipitates formed during aging. The relative contributions of these mechanisms can be quantified as follows.

Modulus mismatch strengthening, $\Delta\sigma_{ms}$, results from the difference between the shear moduli of the precipitate and matrix phases. It can be estimated by using[33, 57]:

$$\Delta\sigma_{ms} = 0.0055M(\Delta G)^{3/2}(\frac{2\phi}{G_{Al}})^{1/2}(\frac{\langle R\rangle}{\mathrm{b}})^{3m/2-1} \qquad (14)$$

where the Taylor factor[58] $M = 3.06$ and ΔG is the difference in the shear modulus between the precipitate and matrix, which are approximated as 30.6 and 40 GPa for $Al_{3-x}Zn_xNi$ and $Al_{3-x}Zn_xZr$, respectively. The shear moduli of $L1_2$-type $Al_{3-x}Zn_xNi$, $Al_{3-x}Zn_xZr$ and the matrix are taken as $G_{\mathrm{Al3-xZnxNi}} = 56$ GPa (same as the value for Al_3Ni[59, 60]), $G_{\mathrm{Al3-xZnxZr}} = 67.4$ GPa (same as the value for Al_3Zr[61-63]), and $G_{Al} = 25.4\,GPa$, respectively. The volume fraction was approximated as $\phi \cong 0.003$ (estimated from the tie line of the Al_3Zr phase diagram) for $Al_{(3-x)}Zn_xZr$. Since the added Zn is assumed to replace the Al site, it is expected that Al_3Zr and $Al_{(3-x)}Zn_xZr$ have similar volume fractions[12]. This assumption is also confirmed by the heat treatment curves. Using the same approach, $\phi \cong 0.002$ for $Al_{(3-x)}Zn_xNi$. $\langle R\rangle$ is the average particle radius of the specimens. Due to their large number density and small interparticle spacing, most of the precipitation strengthening of 1.7Zn0.07Zr comes from the small size particles segregated in the dendritic centers. Hence, the values of $\langle R\rangle$ used for the yield strength estimates were

2.5 nm (dendrite core) and 4.0 nm for the precipitates present in 1.7Zn0.07Zr and 1.8Zn0.05Ni, respectively (Table 5). The Burgers vector magnitude of the matrix was[64, 65] $b = 0.286\ nm$, and m = 0.85 is a constant.

At peak strength, order strengthening $\Delta\sigma_{os}$ (which is due to the formation of antiphase boundaries (APBs) as matrix dislocations shear ordered particles) is given by[33, 57, 64]:

$$\Delta\sigma_{os} = 0.81M\frac{\gamma_{APB}}{2b}\left(\frac{3\pi\phi}{8}\right)^{1/2} \qquad (15)$$

where γ_{APB} ~0.48 and 0.445 Jm^{-2} are taken as the average APB energies for $Al_{3-x}Zn_xNi$ and $Al_{3-x}Zn_xZr$ alloys based on several reported values for Al_3Ni and Al_3Zr for the (111) plane[66-68]. APB energies are difficult to determine, and different methods tend to give varying values for the same intermetallic compound. Therefore, APB energies have only been reported for a limited number of compounds[69-71]. Recently, Rudy and Sauthoff reported a APB energy of ~0.4 Jm^{-2} for NiAl[72]. A study has already reported the APB energy for Ni_3Al ~0.195 Jm^{-2}[73].

During the over-aging, Orowan strengthening $\Delta\sigma_{or}$ is given by[33, 57, 64]:

$$\Delta\sigma_{or} = 0.4M\frac{G_{Al}b}{\pi\sqrt{(1-\nu)}}\frac{\ln\left(\frac{2R}{b}\right)}{\lambda_{e-e}} \qquad (16)$$

where the mean planar radius[64] is given by $R = \frac{\pi}{4}\langle R\rangle$, $\nu = 0.354$ is the Poisson's ratio for Al, and the inter-precipitate distance[64] $\lambda_{e-e} = \left(\sqrt{\frac{2\pi}{3\phi}} - \frac{\pi}{2}\right)\langle R\rangle$.

Coherency strengthening, $\Delta\sigma_{cs}$, can be estimated using[33, 57, 64]:

$$\Delta\sigma_{cs} = M\chi(\epsilon G_{Al})^{3/2}\left(\frac{\langle R\rangle\phi b}{\Gamma}\right)^{1/2} \qquad (17)$$

where $\chi = 2.6$ for fcc metals[64], ϵ is the mismatch parameter approximated by $\frac{2}{3}\delta$; $\delta =$ 1.23% and 0.75% is taken as the lattice parameter mismatch for the $Al_{3-x}Zn_xNi$ and $Al_{3-x}Zn_xZr$ precipitates estimated from the composition-dependent lattice parameter[30-32, 74], and $\Gamma = \frac{1}{2}G_{Al}b^2$ is the line tension of dislocations in Al.

Generally, precipitation hardening is governed by either the dislocation by-pass (Orowan-type) or dislocation shearing mechanisms. At peak strength, only the shearing mechanism was considered and the contributing factors in this mechanism are coherency strengthening ($\Delta\sigma_{cs}$), modulus mismatch strengthening ($\Delta\sigma_{ms}$), and order strengthening ($\Delta\sigma_{or}$)[33, 57]. Regardless of the unavailability of exact data and approximations made for some of the parameters used in the equations above, these models successfully predicted the maximum yield strength observed experimentally. Using equations 14-17 and the data in Table 5, the contribution of each strengthening mechanism to the yield strength of 1.7Zn0.07Zr, was estimated as $\Delta\sigma_{or} \approx 148\,MPa$, $\Delta\sigma_{os} \approx 114\,MPa$, $\Delta\sigma_{cs} \approx 18\,MPa$ and $\Delta\sigma_{ms} \approx 118\,MPa$ for Orowan, order, coherency strain, and modulus mismatch strengthening, respectively. The larger value between $\Delta\sigma_{cs} + \Delta\sigma_{ms}\ (\sim 136\,MPa)$ and $\Delta\sigma_{os}\ (\sim 114\,MPa)$ determines the resultant yield strength increment due to the shearing mechanism[33, 57]. As a result, the yield strength ($\Delta\sigma_{ppt}$) of 1.7Zn0.07Zr at 450 ℃, due to precipitation hardening was estimated as $136\,MPa$ from $\Delta\sigma_{cs} + \Delta\sigma_{ms}$ (ignoring Orowan strengthening). Therefore, the significant difference between the estimated and measured yield strength of 1.7Zn0.07Zr is 20 MPa, which could be attributed to the solid solution strengthening (not considered in the estimate) from the remaining Zn in the matrix. The difference between estimated and measured strength values could also be a result of some of the approximated parameters used in the estimation, due to a lack of exact theoretical or experimental data for the $Al_{3-x}Zn_xZr$ precipitate.

Table 5. Measured precipitate mean radii,$\langle R\rangle$, of $L1_2$ precipitates located at the dendritic centers of 1.8Zn0.05Ni and 1.7Zn0.07Zr, after isochronal aging at 250 and 450 ℃ respectively.

Specimen	Aging Temperature ℃	Mean precipitate radius $\langle R\rangle\ nm$	Number of counted precipitates
1.8Zn0.05Ni	250	4.0	285
1.7Zn0.07Zr	450	2.5	201

Similar to the estimation made for the 1.7Zn0.07Zr alloy, the yield strength due to precipitation ($\Delta\sigma_{ppt}$) of the 1.8Zn0.05Ni alloy at peak strength was estimated as 108 MPa from $\Delta\sigma_{cs} + \Delta\sigma_{ms}$. The measured peak strength for this specimen was 125 MPa. The observed difference between the estimated and measured strength values is 17 MPa, which could also be attributed to the solid solution strengthening due to the remaining Zn left in the matrix and the gross approximation made for some of the parameters used.

4.6 Summary and conclusions

When the solubility limits of the solutes in Al are not considered and all the solute atoms are assumed to remain in solid solution (no precipitation effect), the electrical conductivity predictions from DFT simulations agree well with experiment (expt-SS). According to Figure 22, the addition of Zn to binary Al-TM alloys only slightly reduced the electrical conductivity. This demonstrates that Zn has a minimal impact on electrical conductivity when in- and out-of solid solution. The experimental electrical conductivity data in Figure 27 and Figure 28 show that at equivalent atomic percentage of alloying elements, Al-Zn-Ni has a higher electrical conductivity than Al-Zn-Zr, as predicted by DFT.

Using enthalpy of formation, the predicted zero-temperature stabilities of Al-Zn-Ni and Al-Zn-Zr precipitate phase structures revealed the equilibrium crystal structures of Al_3Ni and Al_3Zr as $D0_{11}$ and $D0_{23}$, respectively. The step-by-step inclusion of Zn into the precipitate phase demonstrated that the resulting $Al_{3-x}Zn_xNi$ and $Al_{3-x}Zn_xZr$ precipitates have stable $L1_2$ structures, which was confirmed by experiment. These simulations were performed at 0 K, hence, the influence of temperature on the stability of the $L1_2$ structures was not computationally determined in this study.

Heat treatment experiments showed that the difference in peak microhardness temperatures of Al-Zn-Ni and Al-Zn-Zr alloys is due to the difference in nucleation and growth rates of Ni and Zr precipitates in aluminum. Peak microhardness values of both alloys increase with Zn loading, whereas conductivity drops slightly. This study also showed that increase in electrical conductivity of Al-Zn-Zr was achieved at peak strength due to precipitation of

the solute atoms from matrix, although this was not observed in the Al-Zn-Ni samples due to the much smaller impact of Ni on conductivity.

A microstructural study of Al-Zn-Ni revealed that for alloys with lower Zn composition (0.5Zn0.05Ni and 1.0Zn0.05Ni), the precipitates retained their orthorhombic $D0_{11}$-Al_3Ni structure, because there was insignificant amount of Zn atom in their precipitate phases. For higher Zn compositions, the precipitate morphology transformed to $Al_{3-x}Zn_xNi$ precipitate as shown in Figure 29[c] and [f]. This indicates that the inclusion of Zn is likely responsible for the possible $D0_{11} \rightarrow L1_2$ precipitate transformation. Since Al_3Zr already has a metastable $L1_2$ structure during aging, there was no precipitate transformation required at 450 ℃. The crystal structure of $Al_{3-x}Zn_xZr$ precipitates formed in 1.7Zn0.07Zr remained as $L1_2$. Hence, the addition of Zn into the Al_3Zr precipitate phase did not alter the $L1_2$ phase structure.

In summary, these alloys have demonstrated a good balance between electrical conductivity and microhardness, relative to several other electrical conductors used for high conducting applications. Examples of such alloys are 1350 aluminum alloy (AA) and Al-Mg-Si (AA6101) commonly used as electrical conductors for overhead power lines. The laboratory fabricated AA1350 has high electrical conductivity (35.7 MS/m) but very low ultimate tensile strength, while Al-Mg-Si (AA6101) has very high strength but lower electrical conductivity, depending on the amount of Mg_2Si solute present[75, 76].

Chapter 5: Microstructure and properties of precipitation-hardened Zr and Zn-Zr based aluminum alloys

Submitted for publication in Journal of Alloys and Compounds

5.1 Abstract and introduction

5.1.1 Abstract

New aluminum alloys with improved durability and thermal resistance are desired to improve the performance of high-voltage power transmission lines. These improvements must not significantly reduce the electrical conductivity of the Al alloys currently used for this application to maintain current levels of power transmission efficiency. Precipitation-hardened binary Al-Zr alloy has been shown to have promising electrical conductivity and strength. However, there is room for improving the alloy strength, while maintaining a relatively high electrical conductivity by controlled additions of Zn. The objective of this study is to experimentally examine the addition of Zn to Al-Zr alloys with subsequent heat treatment to improve mechanical properties via controlled precipitation hardening. Vickers microhardness measurements, scanning transmission electron microscopy, energy-dispersive X-ray spectroscopy, and selected area electron diffraction are used to measure the properties and determine the microstructure of Al-Zr-Zn alloys for a wide range of aging conditions. As expected, the results indicate that Al-Zr-Zn alloys have improved mechanical properties and slightly reduced electrical conductivity relative to Al alloys currently used for power transmission. However, it is determined that the addition of Zn is unable to improve the heat resistance of Al-Zr alloys.

5.1.2 Introduction

The development of new aluminum alloys with improved strength, electrical conductivity, and thermal resistance can improve the efficiency and durability of high-voltage power

transmission lines. Current aluminum alloys used for this application are nearly pure Al, which provides excellent electrical conductivity with relatively poor mechanical durability. Thus, the challenge is to develop new allows with improved strength and thermal resistance without significant degradation of the electrical conductivity.

Improved strengthening of Al alloys can be achieved with the formation of intermetallic precipitates[23, 77]. Precipitates formed from transition metals are particularly stable for long periods of exposure to elevated temperatures, because of low solubility and diffusivity in α-Al. Of all alloying transition elements, Zr offers one of the greatest potentials for forming Al alloys with high strength, creep resistance, and thermal resistance at elevated temperatures[30, 33]. The Zr solute, like many transition elements, is more effective in improving the yield strength of Al-Zr alloy, when out of solution (through the formation of Al_3Zr precipitates), relative to when in solid solution. These precipitates improve strengthening by impeding the movement of dislocations[23]. The observed increase in electrical conductivity during aging is also due to the precipitation Zr solute atoms out of solid solution. As solutes precipitate out of solution, the number density of electron scattering sites is reduced, leading to increase in conductivity[51].

Many intermetallic precipitates formed in Al alloys are non-cubic tri-aluminide compounds ($D0_{11}$, $D0_{22}$, and $D0_{23}$)[78]. The tri-aluminides of group IV and V (Ti, Hf, V etc.), crystallize in the tetragonal $D0_{22}$ or $D0_{23}$ form, which are incoherent with α-Al and promote precipitate coarsening. Of all Al_3TM (TM = transition metals) intermetallic compounds, only Al_3Sc has a thermodynamically stable cubic $L1_2$ structure. However, Al_3Zr forms metastable $L1_2$ precipitate structure at temperatures $\cong 475$ ℃, and transforms to its more stable $D0_{23}$ structure when exposed to higher temperature for several hours[30, 78]. Cubic $L1_2$ precipitate phase is desired because it provides better precipitate/α-Al matrix lattice coherency, creep resistance, and retention of strength at higher temperatures than the non-cubic phases[29, 33].

Several studies have focused on developing ternary alloys with improved strength and more stable $L1_2$ precipitate structures at elevated aging temperatures[30, 36, 78, 79]. Zero-temperature density functional theory (DFT) simulations predict that adding Zn to Al_3Zr

to form $Al_{(3-x)}Zn_xZr$, stabilizes the resulting $L1_2$ $Al_{(3-x)}Zn_xZr$ precipitates with respect to $D0_{23}$ through enthalpy of formation computations[12, 14, 34]. This prediction is made with the use of electronic structure calculations of competing fcc-based ordered structures. Ghosh et al. experimentally confirmed the enrichment of Zn in the resulting $Al_{(3-x)}Zn_xZr$ precipitate phase, by comparing the relative heights (intensity counts) of Zn-K or Zn-L peaks in the EDX spectra acquired from α-Al matrix and $L1_2$ precipitate[34]. Theoretically, Zn stabilizes the $L1_2$ structure by reducing the $^c/_a$ ratio (z – axis) or the number of d-shell electrons of $D0_{23}$ with respect to $L1_2$ phase[12, 35, 37].

There is no study that has been able to effectively demonstrate the prevention of $L1_2 \rightarrow D0_{23}$ precipitate transformation in binary Al-Zr or ternary Al-Zr-TM alloys at temperatures $> 500℃$. This work focuses on the role of Zn addition to Al-Zr in stabilizing the $L1_2$ phase relative to $D0_{23}$, at elevated temperatures $\geq 500℃$ (if any). It also examines how Zn impacts the mechanical properties, thermal resistance and electrical conductivity of Al-Zr at peak and overaged conditions.

5.2 Experimental procedure

5.2.1 Fabrication and specimen preparation

Additional 600 g ingots of 0.2Zr and 3.5Zn0.2Zr (wt.%) were fabricated from the aluminum, zinc and Al-5.0Zr master alloys in VIM. The alloys were melted in graphite crucible placed in the VIM chamber to form ingots; small buttons were cut from the ingots, mechanically polished and their compositions measured using the same procedure discussed in sub-section 4.3. The measured compositions of the alloys used in this study are listed in Table 6.

Table 6. Specimen labels and compositions in wt.% as measured by ICP-OES.

Specimen Label	Al	Actual Zn	Actual Zr
0.2Zr	Bal	0.0	0.20
3.5Zn0.2Zr	Bal	3.5	0.22

5.2.2 Heat treatment

A series of the polished button specimens cut from as-cast 0.2Zr and 3.6Zn0.2Zr ingots, fabricated with VIM were isochronally aged without prior solution heat treatment. The multi-step isochronal aging was carried out on both alloys from 150 to 450 ℃, 150 to 500 ℃ and 150 to 600 ℃ – at 50 ℃ temperature step. The duration at each temperature step was 3 h in the furnace before quenching in water. Finally, isochronal heat treatment from 150 to 600 ℃ – at 50 ℃ temperature step (3 h duration per temperature step) was performed on 3.6Zn0.2Zr button specimen, after prior homogenization at 620 ℃ (within the single-phase region of the phase diagram) for 24 h. This was done to observe the effect of prior solutionizing on peak microhardness.

5.2.3 Deformation and thermal aging

Two 76 mm long and 19 mm diameter as-cast rod specimens were cut out from the 0.2Zr and 3.5Zn0.2Zr ingots. One specimen of each alloy was isochronally heat treated from 150 to 450 ℃ (at 50 ℃ temperature step – each step lasting 3 h in the furnace) to attain peak strength, while the second specimen remained in as-cast state. All specimens were then swaged down to 9.5 mm rods before drawing to wires with a diameter of 4.6 mm for heat resistance and tensile testing. This stage was labelled as-wiredrawn, Figure 33. The diameter reduction of the rods from 19 – 4.6 mm represents 94 %CW (percent cold work).

Each heat treated – wiredrawn specimen was cut into several 102 mm long wire specimens for subsequent thermal aging experiment. Thermal aging experiment was performed on some of these 102 mm long wire specimens at 300 ℃ for 5 h and 15 h, while others were left in their as-wiredrawn state. According to the Arrhenius plot in the IEC international standard for “Thermal resistant aluminum alloy wire for overhead line conductor” (IEC 62004), the accelerated thermal aging of these alloys at 300 ℃ for 5 h corresponds to a continuous operation temperature for 40 years when used as power line conductors[80]. The purpose of thermal aging experiment was to observe the thermal resistance of the alloys. A thermally resistant alloy is defined as an alloy that has the ability to retain ~90 % of its strength after undergoing long-term exposure to high temperatures[80].

5.2.4 Measurements

Vickers microhardness measurements were taken from the mechanically polished surfaces of all specimens at every temperature step and time interval. A 100 g load was used with a dwell time of 15 s. A calibrated Sigmascope SMP10 probe was used to measure electrical conductivity (in MS/m) of the button specimens. The electrical conductivity values of all the drawn wires used in this study were measured by a Keithly setup, consisting of a 2182A nanovoltmeter, current source, and alligator clips. Tensile tests were performed on the as-drawn and heat aged wires with an Instron 8920. A Futek (Model # LCF455) device with maximum load capacity rating of 10,000 lbs attached to the crosshead, a two-inch gauge length, and a $2 \times 10^{-3}\ s^{-1}$ strain rate were used for the tensile tests.

5.2.5 Microstructural observation

For TEM analysis, thin sheets (~ 200 μm thickness) were cut out of isochronally aged 0.2Zr and 3.5Zn0.2Zr specimens (450, 500 and 600 ℃) using wire electrical discharge machining (EDM). These thin sheets were mechanically polished down to < 100 μm thickness and $\sim 3\ mm$ diameter foils were punched from the auto-polished sheets for TEM experiments. An FTS System Multicool chiller connected to the Jet Electropolisher was used to maintain the temperature of a mixture of 150 ml methanol and 60 ml nitric acid (electrolyte) at -35°C before electropolishing was performed on the foil specimens at 10 V (~ 70 mA). The TEM imaging used an FEI Titan Themis scanning transmission electron microscope (STEM) operating at 200 kV. Energy Dispersive X-ray Spectroscopy (EDX) analysis was performed after elemental mapping of the specimens in STEM mode. The electropolished TEM foils were examined using environmental scanning electron microscopy (ESEM), operated at 5 kV with a short working distance.

5.3 Results

The results from the microhardness tests, electrical conductivity tests, and tensile tests, and STEM/SEM microscopy are detailed in this section.

5.3.1 Vickers microhardness (Isochronal aging)

The microhardness values of 0.2Zr and 3.5Zn0.2Zr were measured to determine the influence of Zn addition on the peak microhardness of Al-Zr. The results shown in Figure 31 indicate that adding 3.5wt.% Zn to Al-Zr enhanced the peak microhardness attained from 403 to 459 MPa. During isochronal aging, 0.2Zr and 3.5Zn0.2Zr specimens gained 140 (amounting to 53% microhardness gain) and 132 MPa (40%), respectively, from precipitation strengthening. However, most of the observed difference in microhardness between 0.2Zr and 3.5Zn0.2Zr at as-cast ($\triangle$ microhardness $\cong$ 64 MPa) and peak-aged conditions ($\triangle$ microhardness $\cong$ 56 MPa) is likely due to solid solution strengthening from the added Zn.

The microhardness of the homogenized 3.5Zn0.2Zr specimen dropped instantly from 347 to 253 MPa due to annealing (release of residual stress accumulated during solidification while casting) from solution heat treatment, before isochronal aging (Figure 31). In addition, a much lower peak microhardness (324 MPa) was attained when the homogenized 3.5Zn0.2Zr was aged, because prior homogenization of the Al-Zr alloy first nucleated Al_3Zr precipitates. This reduced the amount of Zr solute left in solid solution for subsequent aging and led to a corresponding lower peak microhardness from precipitation hardening[33]. The subsequent percent increase in the microhardness due to aging of the homogenized 3.5Zn0.2Zr was 19%.

For all aging conditions used for 0.2Zr and 3.5Zn0.2Zr, the peak microhardness occurred at ~450℃. This shows that the addition of Zn to Al-Zr alloy did not cause any significant shift in the peak microhardness temperature during isochronal aging. The first sign of nucleation and precipitate growth was observed after 350 ℃ for both alloys. Hence, Zn did not have any significant impact on the incubation time for nucleation under the aging conditions studied.

Between 450−600℃, the microhardness values of 0.2Zr and 3.5Zn0.2Zr reversed and continued to decrease due to Orowan strengthening, subsequent precipitate coarsening and dissolution[81]. Clearly, there was a steeper decline in the microhardness of 3.5Zn0.2Zr

observed between 450 and 550 ℃, relative to 0.2Zr. The microhardness of 3.5Zn0.2Zr converged toward 0.2Zr as the two alloys overaged. Similar convergence was not observed between 1.0Zn0.07Zr and 1.7Zn0.07Zr (at. %) alloys in a previous study[12] when both alloys had Zn solute. This convergence could initially be due to the combined effect of enhanced precipitate coarsening rate of and/or dissolution of Zn from the $Al_{(3-x)}Zn_xZr$ precipitate phase. The dissolution of Zn from the precipitate phase is discussed in more detail below. The initially lost microhardness of 3.5Zn0.2Zr relative to 0.2Zr, due to its microhardness convergence between 450 and 550 ℃, was restored after isochronal aging at 600 ℃. This microhardness behavior is likely due to Zn addition and is discussed in detail below.

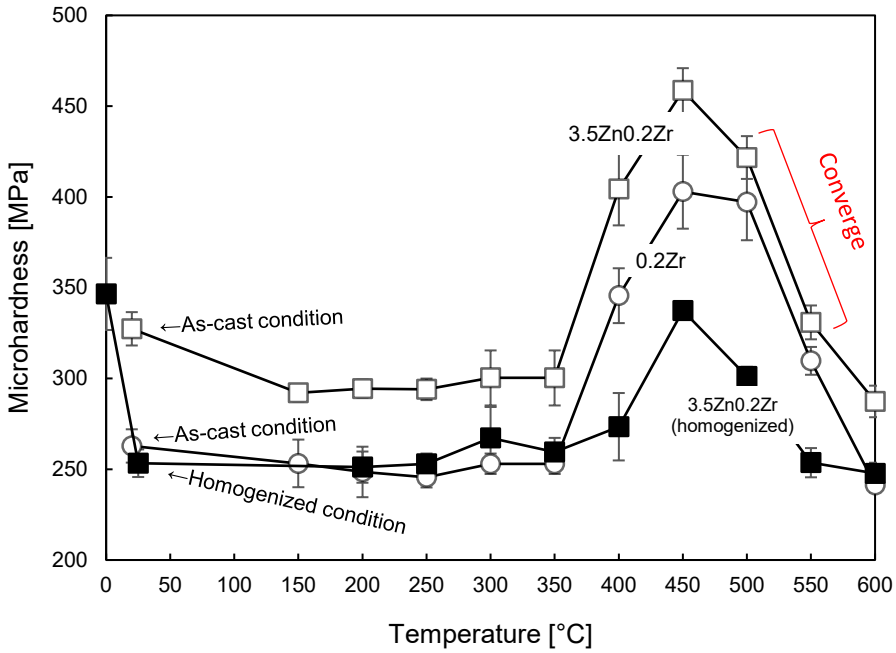

Figure 31. Evolution of Vickers microhardness during isochronal aging of as-cast 0.2Zr, 3.5Zn0.2Zr, and homogenized 3.5Zn0.2Zr specimens. During the early overage stage, the microhardness of 3.5Zn0.2Zr converges toward 0.2Zr as a result of the possible enhanced coarsening rate and Zn dissolution from the precipitate phase.

5.3.2 Electrical conductivity

The as-cast electrical conductivities of 0.2Zr and 3.5Zn0.2Zr were measured as 32.6 and 28.1 MS/m, respectively (Figure 32). The 3.5Zn0.2Zr alloy demonstrated a lower as-cast electrical conductivity compared to 0.2Zr due to a large amount of Zn in solid solution. Similar to the Vickers microhardness measurement (Figure 31), the first evidence of nucleation and growth of precipitates in the alloys was observed after 350 ℃, as the conductivity increased.

Upon continued aging, the peak strengthened specimens recorded maximum electrical conductivities at ~475 ℃; this is about the same temperature at which peak microhardness was attained in the specimens. This indicates that the presence of Zn in Al-Zr did not change the temperature of peak electrical conductivity during multistep isochronal aging, as demonstrated in Figure 32. The observed increase in electrical conductivity was as a result of the precipitation of the solute species out of the solid solution. There was a 1.9 MS/m increase in the electrical conductivity of 0.2Zr to 34.6 MS/m due to aging, while 3.5Zn0.2Zr increased by 1.7 MS/m (peak electrical conductivity is 29.8 MS/m).

The difference between the electrical conductivity values of 0.2Zr and 3.5Zn0.2Zr, at as-cast and peak aged conditions were similar, ~ 4.6 MS/m. This difference was mostly because of the quantity of Zn remaining in solid solution. Due to the high solid solubility of Zn in Al[13], most of the zinc remained in solid solution at the peak-aged condition. Beyond 500 ℃, their electrical conductivities began to drop until they almost reached their as-cast values. Throughout the as-cast, peak-aged, and overaged conditions, the electrical conductivity trend remained consistent. As expected, the electrical conductivity reduced with the addition of Zn at all aging temperatures.

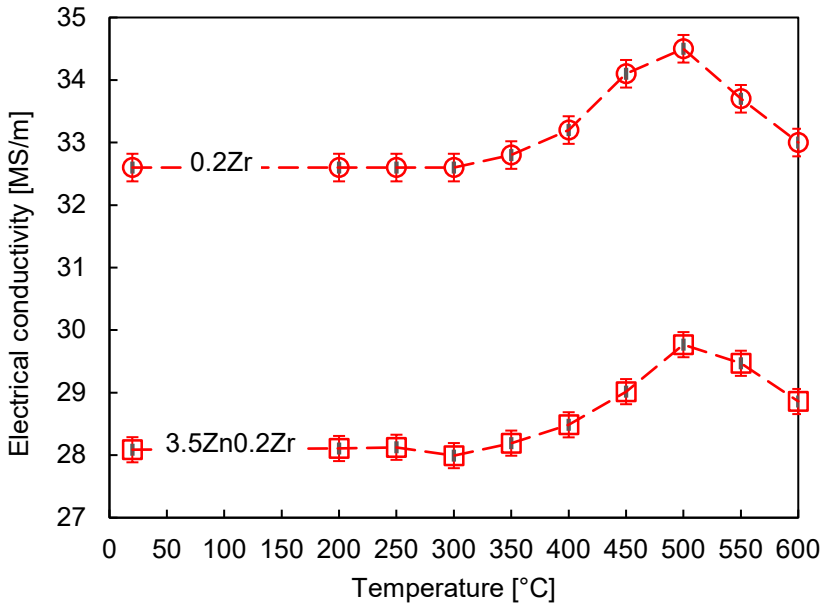

Figure 32. Electrical conductivity of isochronally aged Al-Zr and Al-Zn-Zr specimens. The as-cast and peak conductivities reduced as a result of the addition of Zn.

5.3.3 Thermal aging and tensile test

In Figure 33, "AA+CW" and "CW" denote 94 % CW of isochronally peak-aged and as-cast alloys (0.2Zr and 3.5Zn0.2Zr), respectively. Afterwards, thermal aging experiments were performed on the as-wiredrawn "AA+CW" and "CW" alloys at 300 ℃ for 5 and 15 h to compare the heat resistance of the alloys.

For CW (as-wiredrawn), the tensile strengths of 0.2Zr and 3.5Zn0.2Zr were determined to be 122 and 148 MPa, respectively – not represented on the Figure 33(a). According to this plot, the tensile strengths of the alloys were 192 and 233 MPa for 0.2Zr and 3.5Zn0.2Zr, respectively, at the AA+CW (as-wiredrawn) condition. This means that 0.2Zr gained 70 MPa from prior isochronal peak aging of the cast rods before wiredrawing, while 3.5Zn0.2Zr gained 85 MPa. The difference between the tensile strengths of 0.2Zr and 3.5Zn0.2Zr wires at as-wiredrawn state, before thermal aging, was 26 MPa for CW, compared to 41 MPa for AA+CW condition. This indicates an excess of 15 MPa strength difference was gained in 3.5Zn0.2Zr relative to 0.2Zr from prior heat treatment – AA+CW.

The difference between the tensile strengths of the alloys in the CW condition is mostly due to solid solution strengthening from the added Zn solute.

Because Zn addition is not expected to change the precipitate volume fraction, the excess strength difference of 15 MPa observed between 0.2Zr and 3.5Zn0.2Zr wires, as a result of prior heat treatment of the alloy rods before cold work, could be attributed to the higher strengthening potential of $Al_{(3-x)}Zn_xZr$ relative to Al_3Zr. Assuming the number density of dislocations generated from cold work is approximately the same in both alloys, having gone through similar deformation processes. This would indicate that the strengthening magnitude from dislocation–$Al_{(3-x)}Zn_xZr$ precipitate interaction is slightly higher than that of dislocation–Al_3Zr interaction. This could be as a result of the higher precipitate/matrix lattice mismatch and corresponding coherency strain fields generated by $Al_{(3-x)}Zn_xZr$ precipitates.

After thermal aging of AA+CW wires at 300 ℃ for 5 h, 95% of the as-wiredrawn tensile strength of 0.2Zr specimen was retained, while 3.5Zn0.2Zr retained 84% of its as-wiredrawn strength. The rapid decline of tensile strength after thermal aging for 5 h was mostly due to the recovery process (reduction in the number density of dislocations at elevated temperature due to atomic diffusion). During this process, some of the stored internal strain energies were released by virtue of dislocation motion as a result of enhanced atomic diffusion motion at elevated temperature. It is worth noting that 3.5Zn0.2Zr experienced 16% softening, which is more than the 5% softening for 0.2Zr. This is just a reflection of both alloys losing some of the strengthening potential from their respective dislocation–precipitate and dislocation–solid solution interactions due to the recovery process. Since, the strengthening magnitude derived from the dislocation–precipitate interaction is higher for 3.5Zn0.2Zr relative to 0.2Zr, a greater softening was observed after the dislocation density significantly reduced.

After 15 h of thermal aging, 0.2Zr and 3.5Zn0.2Zr retained 94 and 83% of their as-wiredrawn tensile strengths (similar strength retention to 5 h thermal aging), respectively. The insignificant softening difference between the 5 and 15 h annealed wires showed that

the recovery process was complete in ≤ 5 h. Thus, the inclusion of Zn increased the tensile strength and slightly reduced the thermal resistance of the alloy.

The electrical conductivities of the AA+CW wires before and after thermal aging for 5 and 15 h were measured (Figure 3(b)). The data indicates that there was a slight increase in electrical conductivities of the wires as a result of annealing for 5 and 15 h. After 5 h of thermal aging, the electrical conductivity of 0.2Zr increased from 34.9 to 35.3 MS/m (35.7 MS/m after 15 h), while 3.5Zn0.2Zr increased from 29 to 29.5 MS/m (30 MS/m after 15 h). The observed increase in electrical conductivity after annealing (recovery process) was due to annihilation of dislocations.

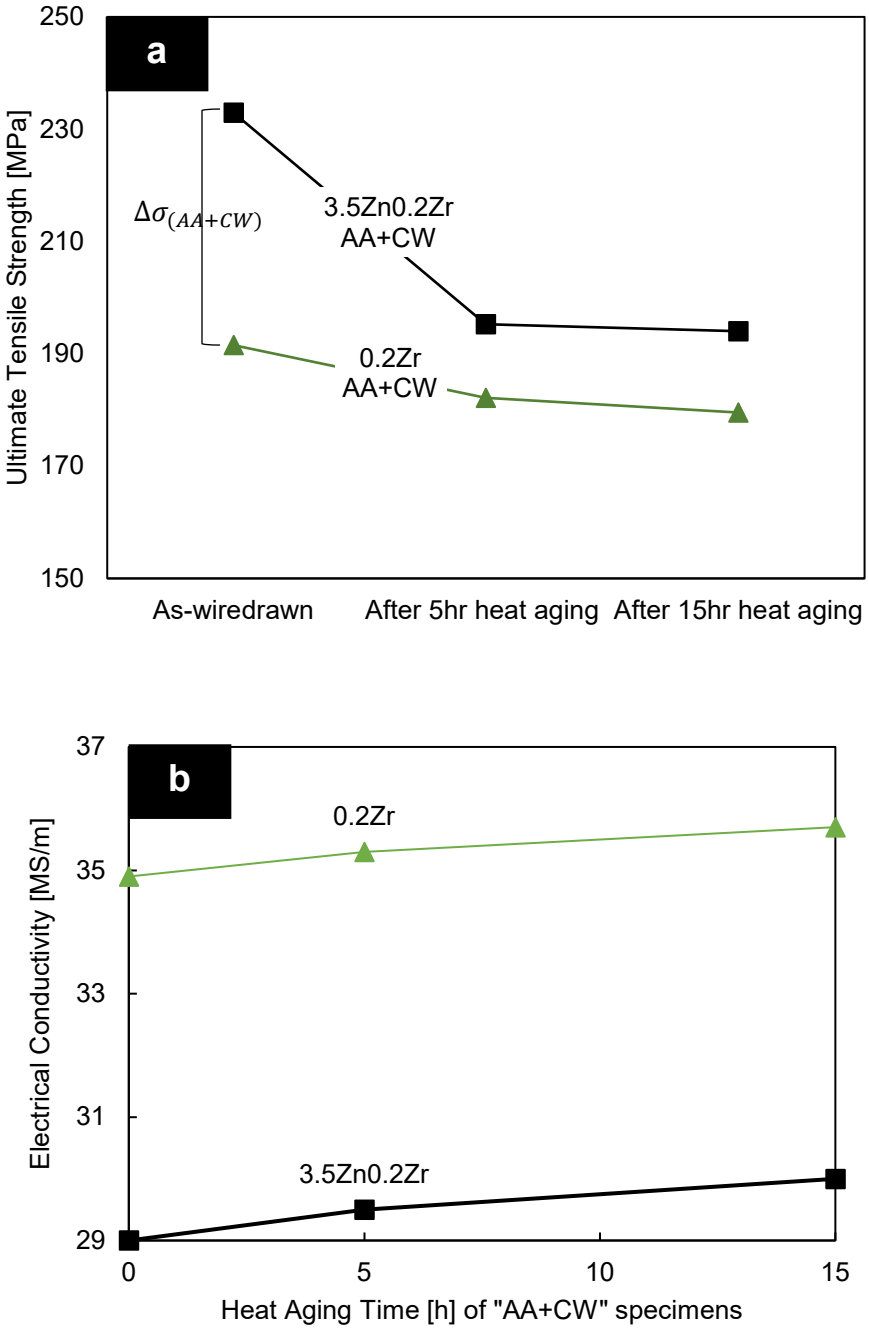

Figure 33. Results of thermal aging test performed on post peak aged – cold worked (AA+CW) 0.2Zr and 3.5Zn0.2Zr at 300 ℃ for 5 and 15 h. (a) The tensile strengths of both specimens were measured before and after thermal aging. (b) The corresponding electrical conductivity measurements.

5.3.4 Dendritic/interdendritic microstructure

Several studies have shown that during casting, some peritectic Al-Zr and Al-Zr-TM alloys form dendritic/interdendritic microstructures as they solidify. Smaller precipitates occupy the precipitate-rich dendritic center, whereas the interdendritic channels are occupied by low number densities of larger precipitates[30, 31]. The larger precipitates in the interdendritic channels are possible because they can nucleate and grow before their diffusion fields begin to overlap[30]. Figure 34 reveals the precipitate gradient across the 3.5Zn0.2Zr specimen. From observation, the dendritic center was characterized by a high number density of smaller precipitates (mean radius $\langle R \rangle = 2.45\ nm$) compared to those present in the interdendritic channel, $\langle R \rangle = 6.5\ nm$, Figure 34(a) and (c).

The high concentration of segregated Zr solute (due to solidification during alloy casting) in the dendritic center was responsible for the high number density and small size of the precipitates during aging, because the chemical driving force for nucleation increases with supersaturation of Zr solutes. As a result, the critical mean radius required for nucleation to occur was reduced and smaller precipitates were formed (Figure 34(c)). From previous study, the mean precipitate size of aged Al-Zr or Al-Zr-TM alloy increases progressively along a lateral position from the dendritic center toward the interdendritic channel[30, 31]. This is because the supersaturation of Zr solute decays along this direction[30, 31]. In the interdendritic channels, Zr solute was depleted as the chemical driving force for nucleation was reduced. The critical mean radius for nucleation increased, causing a low volume fraction of bigger precipitates to be formed (Figure 34(a)). One disadvantage of the interdendritic channels is that they are usually weaker and more susceptible to failure relative to other regions because of the fewer and bigger precipitates present. This leads to deleterious effects on the mechanical properties[30, 31, 82].

Precipitate-rich dendritic edges that boarder the interdendritic channel were characterized by precipitate free zones (Figure 34(b)) which were about 0.5 μm wide[30, 31]. The bigger precipitates were located within the interdendritic channels, after crossing over the precipitate free zone (PFZ). Because Zr has a very low diffusivity in α-Al, it is almost impossible to homogenize Al-Zr or Al-Zn-Zr alloys, except alloys that are solutionized at

high temperatures below the liquidus line but within the single-phase region ~ 620 ℃ for an extensively long time[12, 44]. This is why the dendritic/interdendritic microconstituents observed in (Al,TM)-Zr alloys are difficult to eliminate. Table 7 summarizes the sizes of the precipitates positioned in the interdendritic channels.

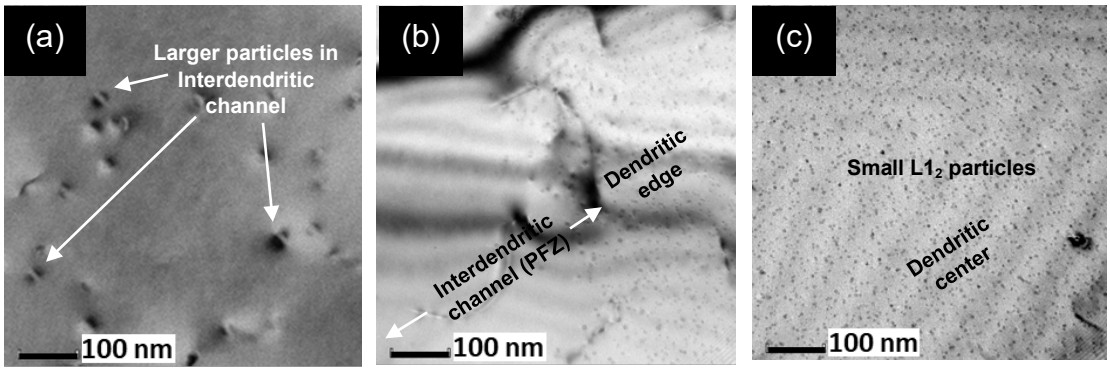

Figure 34. Distribution and mean sizes of precipitates in the dendritic center, edge, and interdendritic channel corresponding to the microsegregation of Zr solute in the 3.5Zn0.2Zr specimen. (a) Precipitates formed in interdendritic channels have a bigger mean size but smaller number density, (b) precipitate free zone (PFZ) along the boundary between a dendritic edge/interdendritic channel, (c) Dendritic center with smaller-size precipitates.

5.3.5 Precipitate structure and size

It is expected that the precipitates formed when as-cast Al-Zr is peak aged have metastable $L1_2$-Al_3Zr phases that are coherent with α-Al matrix. The precipitate/matrix coherency is confirmed by the precipitates' Ashby-brown strain contrast reported in several studies[12, 30, 31, 34, 79]. Similar Ashby-brown strain contrasts were also observed for coherent $Al_{(3-x)}Zn_xZr$ precipitates formed in the interdendritic channels of 3.5Zn0.2Zr system (Figure 35(b)) after isochronal aging at 450 ℃. Comparison of precipitates revealed that the mean precipitate size of $Al_{(3-x)}Zn_xZr$ is slightly bigger than that of Al_3Zr. The mean radii of these precipitates formed in the interdendritic channels are $6.5 \pm 1.2\ nm$ for $Al_{(3-x)}Zn_xZr$ (Figure

35(a)) and approximately $5.5 \pm 1.5\ nm$ for Al_3Zr (Figure 35(c)). This indicates that adding Zn increased the average precipitate growth.

After isochronal aging at 600 ℃, some of the precipitates formed in the alloys remained in the $L1_2$ structure. Pronounced coarsening of the precipitates led to significant increases of their mean radii, as summarized in Table 7. The $Al_{(3-x)}Zn_xZr$ interdendritic precipitate mean size increased significantly to $\langle R \rangle \cong 30\ nm$ from $6.5\ nm$ (Figure 36). On the other hand, Al_3Zr increased from $\langle R \rangle \cong 5.5\ nm$ to $23\ nm$. Thus, $L1_2$-Al_3Zr and $Al_{(3-x)}Zn_xZr$ precipitate mean sizes increased by a factor of four after aging from 450 to 600 ℃. The gain in precipitate size of $Al_{(3-x)}Zn_xZr$ ($\sim 23.5\ nm$) is larger relative to Al_3Zr ($\sim 17.5\ nm$). This observation indicates that the inclusion of Zn increased the precipitate coarsening rate. This is in part due to the higher diffusivity of Zn in Al relative to that of Zr.

At 600 ℃, the transformation of some of the heterogeneously nucleated particles in 0.2Zr and 3.5Zn0.2Zr from $L1_2$ to $D0_{23}$ was observed along the interdendritic channels and on dislocations (Figure 36 (c), (e) & (f)). The $D0_{23}$ disk-like precipitates in the alloys are $\sim 400 - 500$ nm in length. During overaging, the $L1_2$ to $D0_{23}$ transition is not direct; rather, it occurs in two stages[30, 31]: Dissolution of solutes from metastable $L1_2$ phase and formation of new equilibrium $D0_{23}$ by re-precipitation from the dissolved solutes.

TEM images acquired from the peak-aged specimens (Figure 35) were collected along a low index [111] zone axis. Their selected area electron diffraction (SAED) patterns show cubic {101} superlattice spots forming hexagonal patterns around each fcc spot (Figure 35(a) & (c)). These indicate the presence of an ordered lattice structure attributed to the $L1_2$ phase. Therefore, the structures of coherent Al_3Zr and $Al_{(3-x)}Zn_xZr$ precipitates were confirmed as $L1_2$ at a 450 ℃ aging temperature.

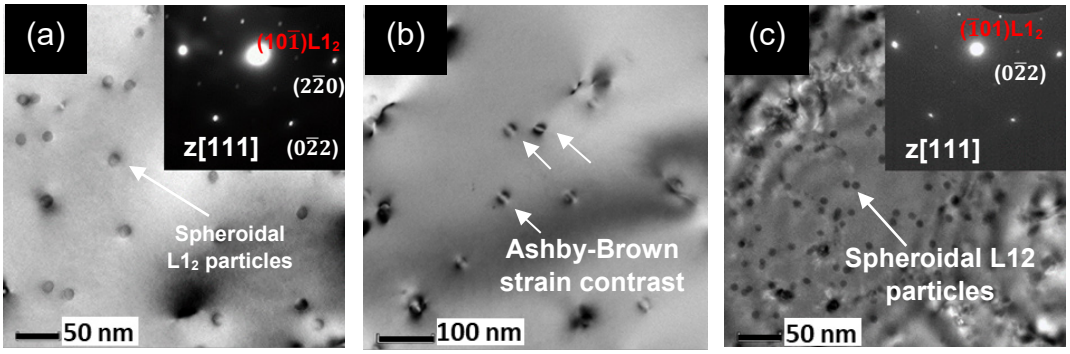

Figure 35. Coherent $L1_2$ precipitates formed in 0.2Zr and 3.5Zn0.2Zr at 450 ℃, as indicated by the line of no contrast and {110} superlattice spots in the diffraction patterns (inset), (a) Spheroidal-$L1_2$ $Al_{(3-x)}Zn_xZr$ precipitates, which are coherent with the matrix as evident by their Ashby-Brown strain contrasts, shown in (b), (c) Coherent $L1_2$ Al_3Zr spherical particles were also formed in 0.2Zr.

Table 7. Measured precipitate mean radii,$\langle R \rangle$, of $L1_2$ precipitates located in the interdendritic channels of 0.2Zr and 3.5Zn0.2Zr, after isochronal aging at 450, 500, and 600 ℃.

Specimen	Aging Temperature ℃	Mean precipitate radius $\langle R \rangle$ nm	Number of counted precipitates
3.5Zn0.2Zr	450	6.5	152
	500	10.0	56
	600	30.0	84
0.2Zr	450	5.5	92
	500	8.5	124
	600	23.0	134

The diffraction pattern of the overaged spheroidal $Al_{(3-x)}Zn_xZr$ showed {100} and {110} superlattice spots along [110] zone axis, which corresponds to the $L1_2$ structure (Figure 36(a)). There were planar faults parallel to (001)-$L1_2$. High-resolution TEM (HREM), Figure 36(b) inset, confirms that the planar faults is parallel to {100} planes of the $L1_2$-$Al_{(3-x)}Zn_xZr$ phase, with $d_{100} = 0.41$ nm. The planar faults are always parallel to the {100}

planes in the $L1_2$ phase (Figure 36(b)) and are identified as antiphase boundaries (APB) with a dislocation vector $^{a_p}/_2\langle 110\rangle$ in the {100} plane, where a_p is the lattice parameter of the $L1_2$ unit cell. Generally, the formation of these planar faults is the first step in the transformation to stable tetragonal $D0_{22}$ or $D0_{23}$ structures[83]. Similar planar faults were also detected in Al-Zr, Al-Ti-V-Zr, and Al-Ti-Zr alloys using TEM (Tsau & Chen, 2002)[83, 84]. There were also disk-like $Al_{(3-x)}Zn_xZr$ precipitates identified by SAED patterns as fully transformed $D0_{23}$ (Figure 36(c)). Therefore, spheroidal $L1_2$ and disk-like $D0_{23}$ precipitate structures were confirmed in the 3.5Zn0.2Zr alloy at 600 ℃. As expected, spheroidal $L1_2$ and disk-like $D0_{23}$ precipitates were also present in 0.2Zr (Figure 36(d–f)).

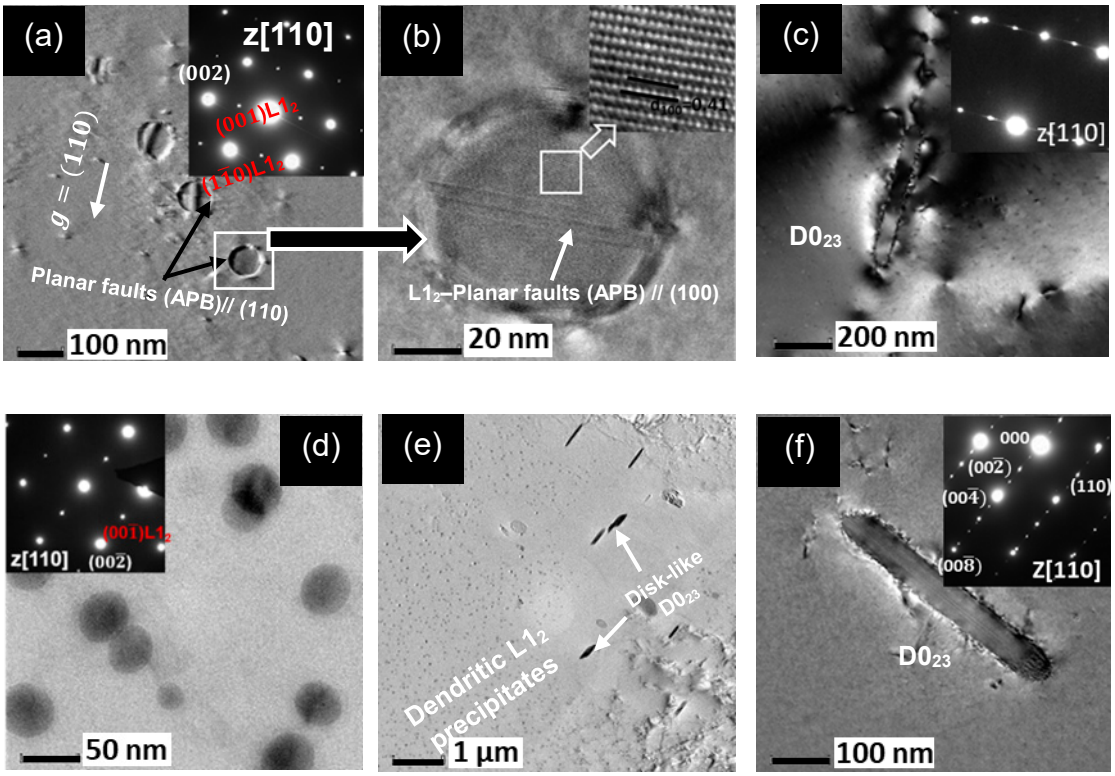

Figure 36. Coarsened interdendritic Al_3Zr and $Al_{(3-x)}Zn_xZr$ precipitates aged at 600 ℃. The precipitate mean size increased significantly to $\langle R \rangle = 23\ nm$ and $30\ nm$ for spheroidal Al_3Zr and $Al_{(3-x)}Zn_xZr$, respectively. (a) The planar faults observed when the beam was tilted along the [110] zone axis showed that the $L1_2$-$Al_{(3-x)}Zn_xZr$ precipitates were semi-coherent with the matrix. (001) and (1$\bar{1}$0) superlattice spots indicate the $L1_2$ structure for the $Al_{(3-x)}Zn_xZr$ phase, (b) HREM image of the spheroidal $L1_2$-$Al_{(3-x)}Zn_xZr$ particle highlighted in 6(a), showed planar faults parallel to the (100) lattice plane, (c) Completely transformed disk-like $D0_{23}$-$Al_{(3-x)}Zn_xZr$, (d) Some Al_3Zr precipitates maintained their $L1_2$ form, (e and f) Disk-like $D0_{23}$-Al_3Zr precipitates were formed heterogeneously on dislocations and along the interdendritic channel at 600 ℃.

In order to examine the broader distribution and number density of the $D0_{23}$ precipitate phase, low magnification SEM images were taken from isochronally aged 0.2Zr and 3.5Zn0.2Zr specimens after aging at 600 ℃. Due to the combination of the smaller precipitate sizes and the SEM resolution, the overaged $L1_2$ precipitates are barely

noticeable in the images. Figure 37 shows that both specimens have very similar number densities of transformed $D0_{23}$ precipitates. In summary, the inclusion of Zn into the Al_3Zr precipitate phase did not prevent the eventual $L1_2 \rightarrow D0_{23}$ transformation from taking place at 600 ℃. Hence, the stability of the $L1_2$ precipitate phase with Zn addition was not established in this study.

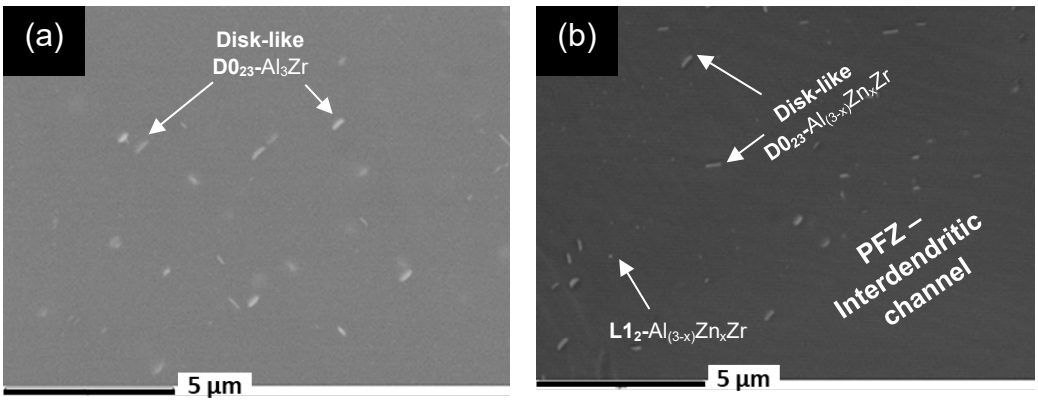

Figure 37. SEM images showing the distribution of $L1_2$ and $D0_{23}$ precipitates across both specimens after isochronal aging at *600* ℃, (a) 0.2Zr and (b) 3.5Zn0.2Zr.

5.3.6 Solute segregation in aged specimen

In order to observe the nanoscale distribution of Zn and Zr solutes in isochronally aged 3.5Zn0.2Zr specimens, elemental maps of the matrix and precipitates were obtained in aberration-corrected STEM. High-angle annular dark field (HAADF) and STEM map images were acquired under magnification of 1300 KX and high voltage: 200kV. After isochronal aging at 450 ℃, the particles examined by EDX mapping had a mean particle radius $\langle R \rangle = 6.0\, nm$, interparticle spacing of 15 – 20 nm and were located in the interdendritic channel (Figure 38 (a)). As seen in Figure 38 (b and c), Al is the matrix, while Zn is uniformly distributed in the matrix. However, EDX data showed a very slight Zn enrichment of the precipitate phase. Almost all the Zr species were concentrated in the $Al_{(3-x)}Zn_xZr$ precipitates (Figure 38 (d)). This concentration of Zr solute in the precipitate phase is also reflected in Table 8 and indicates that Zr solutes migrated from their

supersaturated position in the dendritic region or depleted interdendritic channel into nearby precipitate phases, leaving the surrounding matrix with no Zr.

Similar Zr solute concentrations were observed in coarsened $L1_2$- and $D0_{23}$- Al_3Zr precipitate phases after isochronally aging 0.2Zr at 600 ℃ (Figure 39). This observed concentration of Zr solute in the precipitate phase is confirmed by the chemical composition data shown in Table 8. The coarsened spheroidal-Al_3Zr precipitate observed, $\langle R \rangle \cong 30.0$ nm, shows planar faults signaling a potential $L1_2 \rightarrow D0_{23}$ transformation. The $D0_{23}$ precipitate had a length of $\cong 480.0$ nm.

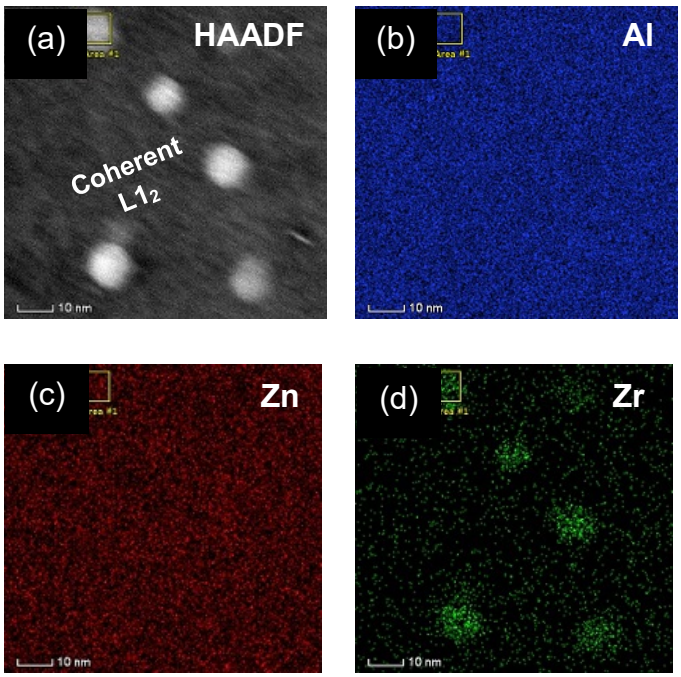

Figure 38. HAADF STEM mapping of Al, Zn and Zr in 3.5Zn0.2Zr at peak aged temperature, including the $Al_{(3-x)}Zn_xZr$ precipitates located at the interdendritic channel. (a) The particles separated by ~15-20 nm spacing were mapped in order to observe the distribution of the elements, (b and c) Al (blue) and Zn (red) were uniformly distributed across the specimen, although EDX data showed slight enrichment of Zn in the precipitate phase relative to the matrix, (d) Zr atoms (green) were concentrated inside the $L1_2$ precipitate phase, while the surrounding matrix region was deficient in Zr solute.

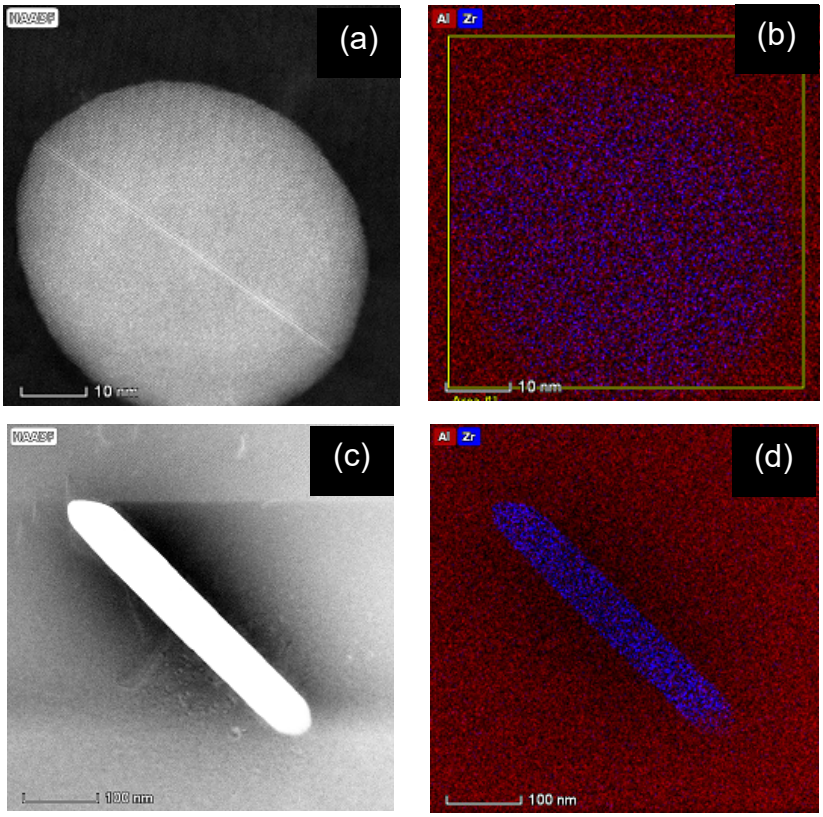

Figure 39. HAADF STEM mapping of Al and Zr in 0.2Zr after overaging at 600 ℃. The interdendritic particles have significantly coarsened, (a & c) HAADF of $L1_2$-Al_3Zr (spheroidal) and $D0_{23}$-Al_3Zr (disk-like) precipitates. Planar faults are seen in the $L1_2$ precipitate before complete transformation into $D0_{23}$. Their corresponding mappings are also shown in (b and d) Al (red) is the matrix, while Zr (blue) is concentrated in the precipitate phase.

5.3.7 Dissolution of Zn from precipitate phase at 600 ℃

As the 3.5Zn0.2Zr specimen overaged at 600 ℃, its particles increased in size (Figure 40(a)), as Zn gradually dissolved from the $Al_{(3-x)}Zn_xZr$ precipitates back into the matrix phase. This explains why the $Al_{(3-x)}Zn_xZr$ precipitate phase had a higher Zn composition of 8.0 wt.% at 450 ℃ than 5.5 wt.% at 600 ℃. The dissolved Zn formed several solid solution clusters within the matrix, as shown in Figure 40 (b) and (c). These Zn cluster features were not found in 3.5Zn0.2Zr at 450 ℃. They appear on the micrograph as small pseudo-

particles $\langle R \rangle < 3\,nm$, with no particular morphologic form (HAADF: white contrast in Figure 40 (c)). However, SAED collected from this region along the [110] zone did not reveal superlattice spots that could be associated with any precipitate ordered lattice structure (Figure 40(b)). Only fcc plane spots were present.

EDX data summarized in Table 8 shows that these particle-like features only contained Al and Zn, with no Zr present. Based on the diffraction pattern and the inability of Al and Zn to form an intermetallic compound[13] (Al-Zn binary phase diagram), the particle-like features were determined to be solid solution clusters of Zn within the α-Al matrix and not actual precipitates. EDX chemical composition analysis performed on the Zn clusters identified as A, B and C in the figure revealed that the composition of Zn in the clusters are inconsistent; as A, B and C have 65.4, 35.5 and 72.3 at% Zn, respectively. The Zn:Al wt.% ratio is the highest in the Zn cluster feature $(0.6 - 2.6)$ compared to the α-Al matrix and precipitate phase (0.13) at 600 ℃.

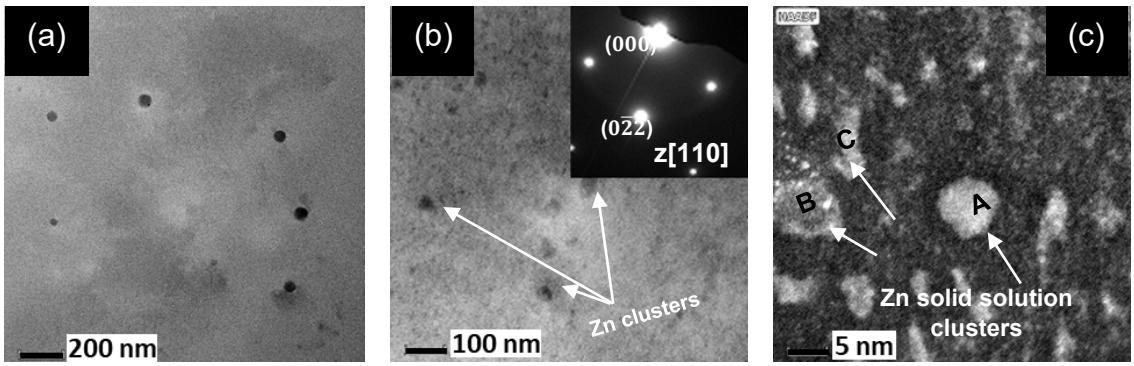

Figure 40. Overaged $Al_{(3-x)}Zn_xZr$ precipitates and Zn clusters formed in 3.5Zn0.2Zr at 600 ℃. (a) The $L1_2$–$Al_{(3-x)}Zn_xZr$ precipitates observed were coarsened with a mean particle radius of ~ 30 nm (b) Particle-like Zn clusters formed within the matrix, (c) HAADF image of Zn clusters (white contrast) with no specific form, distributed across the matrix. Cluster A, B and C have varying Zn composition.

Table 8. EDX of isochronally aged 0.2Zn and 3.5Zn0.2Zr (wt.%) at 450, 500 and 600 ℃

Specimen name	Aging temperature ℃	Surrounding Matrix			Precipitate			Zn in precipitate
		Al	Zn	Zr	Al	Zn	Zr	Zn:Al
3.5Zn0.2Zr	450	96.5	3.5	0.0	41.5	8.0	50.5	0.20
	500	96.6	3.5	0.0	42.2	7.0	50.8	0.17
	600	96.6	3.4	0.0	43.2	5.5	51.3	0.13
0.2Zr	450	100	-	0.0	47.0	-	53.0	-
	500	100	-	0.0	47.0	-	53.0	-
	600	100	-	0.0	47.0	-	53.0	-
Features in 3.5Zn0.2Zr	Aging temperature ℃	Surrounding Matrix			Zn cluster			Fraction of Zn in cluster
		Al	Zn	Zr	Al	Zn	Zr	Zn:Al
Zn cluster A	600	96.4	3.6	0.0	34.6	65.4	0.0	1.9
Zn cluster B	600	96.4	3.6	0.0	64.5	35.5	0.0	0.6
Zn cluster C	600	95.7	4.3	0.0	27.7	72.3	0.0	2.6

Additionally, ternary phase diagram was used to determine whether the dissolution of Zn observed in the 3.5Zn0.2Zr at 600°C was due to formation of liquid phase from melting. From Figure 41 (top), it is clear that for 3.5Zn0.2Zr alloy, no liquid phase from melting occurs at temperature ≤ 630℃. According to the isothermal ternary phase diagram, at 630℃, the first liquid phase starts forming at ~ 8 wt.%Zn, if the amount of Zr is kept at 0.2 wt.%. To melt 3.5Zn0.2Zr, the aging temperature has to be increased to 650 ℃, as shown in Figure 41 (bottom). Therefore, since the maximum temperature attained during the heat treatment experiment was 600°C, Zn must have dissolved from the precipitates to form solid solution cluster at this temperature.

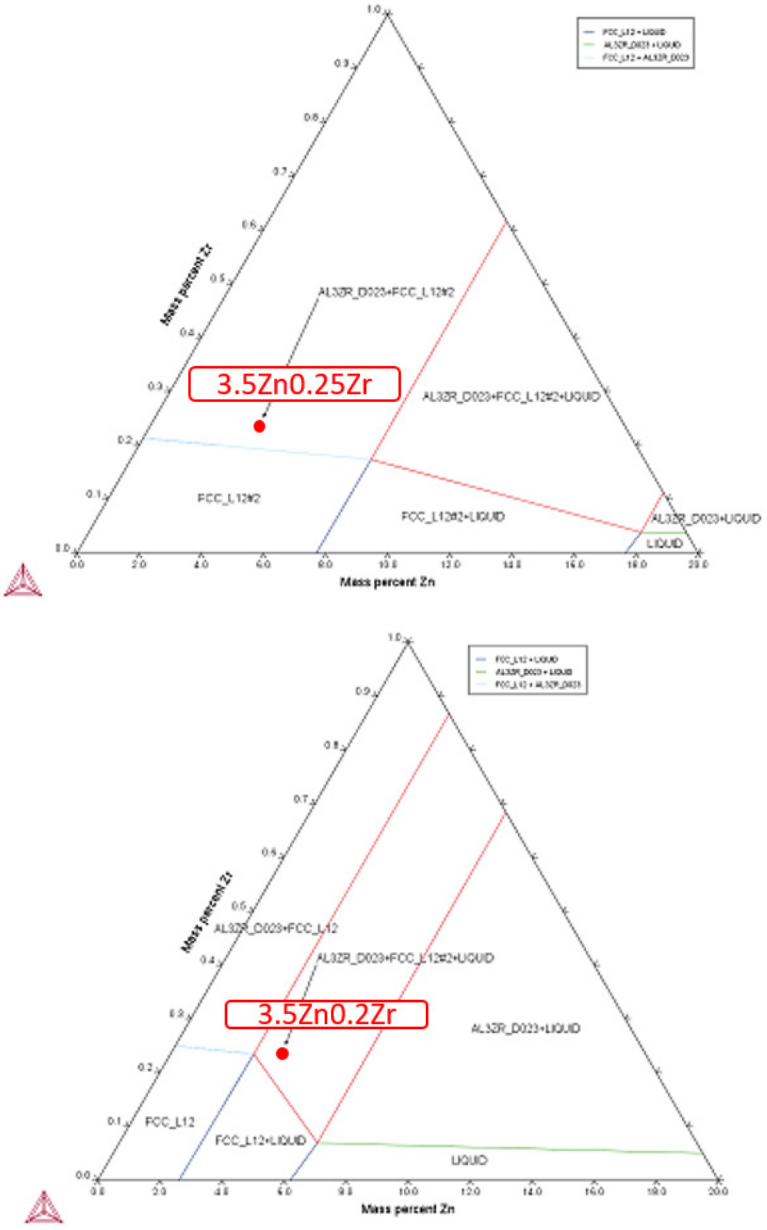

Figure 41. Isothermal ternary phase diagram of Al-Zn-Zr at 630°C (top) and 650°C (bottom), shows that liquid phase does not form for 3.6Zn0.2Zr at temperatures $\leq$ 630°C. At the same composition, liquid phase is present at 650°C.

5.4 Discussion

Based on the results presented above, this section discusses the effect of Zn on strengthening, $L1_2$ stability, precipitate growth, and electrical conductivity.

5.4.1 Effect of Zn addition on strengthening

The addition of Zn to Al-Zr alloy improved the microhardness by two main mechanisms: solid solution and precipitation strengthening. Of all elements, Zn has the highest solubility in Al, showing a maximum of 67 at. % at 381 ℃ in binary Al-Zn alloys[85]. Therefore, only a very small fraction of Zn goes into the precipitate phase during aging, while the remaining stays in solid solution[12, 13]. The role of Zn addition in improving the Al-Zr strength was investigated by:

(1) Observing the microhardness difference between 0.2Zr and 3.5Zn0.2Zr in as-cast and peak-aged conditions. Since the maximum increase in microhardness attainable from precipitation hardening is dependent on the root square of volume fraction, ϕ, the similarity in microhardness values gained between as-cast and peak-aged ($\Delta MH = MH_{peak-aged} - MH_{as-cast}$) conditions of 3.5Zn0.2Zr ($132\ MPa$) and 0.2Zr ($140\ MPa$) alloys indicates that the addition of zinc to Al-Zr did not significantly increase the volume fraction of the precipitates formed. This is also supported by the similar microhardness difference between 0.2Zr and 3.5Zn0.2Zr at as-cast (64 MPa) and peak aged (56 MPa) conditions (Figure 31). Therefore, as long as the ϕ values of precipitates formed in both alloys are similar, the difference between the microhardness of 0.2Zr and 3.5Zn0.2Zr at maximum strength was mostly due to solid solution strengthening from the Zn solute present in the α-Al matrix.

(2) Estimating the precipitate mean size based on multiple TEM micrographs. The size of the precipitates influenced the magnitude of modulus mismatch, coherency, and Orowan strengthening.

(3) Estimating how the effect of Zn on the parameters used in the various precipitation strengthening equations affected their magnitudes. This estimation was used to determine how the strengthening potential of Al_3Zr differs from $Al_{(3-x)}Zn_xZr$.

(4) Comparing Zn composition in precipitate and matrix phases, based on EDX chemical composition analysis. This confirmed the enrichment of Zn in the precipitate phase, leading to the formation of $Al_{(3-x)}Zn_xZr$.

At various stages of aging temperatures ≤ 450 ℃, precipitation hardening is generally governed by dislocation shearing. The contributing factors to this mechanism are modulus mismatch, order, and coherency strengthening[12, 33]:

Modulus mismatch strengthening $\Delta\sigma_{ms}$, is as a result of the difference between the shear moduli of precipitates and matrix phases, and it is estimated by[57]:

$$\Delta\sigma_{ms} = 0.0055M(\Delta G)^{3/2}\left(\frac{2\phi}{G_{Al}}\right)^{1/2}\left(\frac{\langle R\rangle}{b}\right)^{3m/2-1} \qquad (18)$$

where $\langle R\rangle$ is the average particle radius of the specimens, the Burgers vector magnitude of the Al matrix[64, 65] $b = 0.286\,nm$, m = 0.85. the Taylor factor[58] $M = 3.06$, and ΔG is the difference in the shear modulus between the precipitate and matrix. The $L1_2$ shear moduli of Al_3Zr, $Al_{(3-x)}Zn_xZr$, and the Al matrix are taken as $G_{Al3Zr} = G_{Al3-xZnxZr} \cong 68.3\ GPa$[26, 62] and $G_{Al} = 25.4\ GPa$, respectively. First principle predictions by Zhenyi Wei et al. determined the shear modulus of Al_2ZnZr (which has 25 at.% Zn present in the precipitate phase) as $G_{Al2ZnZr} = 83.4\ GPa$[63]. However, they did not confirm this experimentally. Since, according to EDX data in Table 8, the fraction of Zn present in the $Al_{(3-x)}Zn_xZr$ precipitate phase was ~5.5 at. % at 450℃, the true shear modulus of $G_{Al3-xZnxZr}$ would be between the shear modulus of Al_3Zr and Al_2ZnZr, $68.3\ GPa \leq x \leq 83.4\ GPa$. Moreover, it would be expected to be much closer to $68.3\ GPa$. The volume fraction $\phi = 0.003$ (estimated from the tie line of Al_3Zr phase diagram) for both precipitate compositions, because it is expected that Al_3Zr and $Al_{(3-x)}Zn_xZr$ have similar volume fractions based on the microhardness and electrical conductivity results.

Order strengthening, $\Delta\sigma_{os}$, is due to the formation of APB as dislocations cut through ordered particles. It is maximum when the particles are completely sheared, yielding peak microhardness, and it is given by[57, 74]:

$$\Delta\sigma_{os} = 0.81M\frac{\gamma_{APB}}{2b}\left(\frac{3\pi\phi}{8}\right)^{1/2} \qquad (19)$$

where γ_{APB} ~$0.445\ Jm^{-2}$ is taken as the average APB energy for $Al_{(3-x)}Zn_xZr$ alloys based on several reported values for the (111) plane of Al_3Zr[67, 68].

Coherency strengthening, $\Delta\sigma_{cs}$, is estimated by using[57, 74]:

$$\Delta\sigma_{cs} = M\chi(\epsilon G_{Al})^{3/2}\left(\frac{\langle R\rangle\phi b}{\Gamma}\right)^{1/2} \qquad (20)$$

where $\chi = 2.6$ for fcc metals, ϵ is the mismatch parameter approximated by $\frac{2}{3}\delta$; δ is the lattice mismatch and $\Gamma = \frac{1}{2}G_{Al}b^2$ is the line tension of dislocations in Al.

At temperatures > 450 ℃, the particles begin to overage as the strengthening is governed by Orowan strengthening, $\Delta\sigma_{or}$, which is given by[57, 74]:

$$\Delta\sigma_{or} = M\frac{0.4G_{Al}b}{\pi\sqrt{(1-\nu)}}\frac{\ln(\frac{2R}{b})}{\lambda_{e-e}} \qquad (21)$$

where the mean planar radius[86] R = $\frac{\pi}{4}\langle R\rangle$, $\nu = 0.354$ is the Poisson's ratio for Al[58], and the inter-precipitate distance[86] is $\lambda_{e-e} = \left(\sqrt{\frac{2\pi}{3\phi}} - \frac{\pi}{2}\right)\langle R\rangle$.

From all the parameters required in the strengthening equations listed above, only the ΔG, ϵ, and $\langle R\rangle$ terms are significantly affected by the conversion of the precipitate phase from Al_3Zr to $Al_{(3-x)}Zn_xZr$. The following parameters: $M, G_{Al}, b, m, \pi, \Gamma, \nu\ and\ \chi$ are constants, while λ_{e-e} (depends on volume fraction), γ, and ϕ remain approximately similar for both precipitate phases. Below is a description of how increasing ΔG, ϵ, and $\langle R\rangle$ independently influenced the precipitation strengthening derived from $Al_{(3-x)}Zn_xZr$ relative to Al_3Zr.

(a) ΔG: Since $Al_{(3-x)}Zn_xZr$ precipitates have about ~5.5 at. %, the shear modulus $G_{\mathrm{Al3-xZnxZr}}$ could be assumed to be relatively low, 68.3 GPa, which is the value for G_{Al3Zr} rather than the higher value of $G_{\mathrm{Al2ZnZr}} = 83.4\ GPa$, corresponding to

25 at.% Zn. Therefore, only a slight increase in the corresponding $\Delta\sigma_{ms}$ is expected as a result of the change in precipitate phase from Al_3Zr to $Al_{(3-x)}Zn_x$.

(b) ϵ: Given that the lattice parameters of α-Al and $L1_2$-Al_3Zr are a =0.40496 and a_p =0.408 nm respectively at room temperature, the lattice mismatch of coherent $L1_2$-Al_3Zr with α-Al is $\delta = +0.75\%$[31, 68]. There are no consistent experimental or theoretical data for a_p of $Al_{(3-x)}Zn_xZr$ intermetallic compounds. Zhenyi Wei et al. reported the lattice parameter of $L1_2$-Al_2ZnZr as 0.4099 nm[63] at 0K from the quasi-harmonic approximation method, but did not provide the value for $L1_2$-Al_3Zr. Comparison of their reported value to that of Knipling or Lefebvre for $L1_2$-Al_3Zr (a =0.408 nm)[31, 68] reveals that the addition of Zn to the precipitate phase increased the precipitate/matrix lattice mismatch from $+0.75\%$ for Al_3Zr to $+1.22\%$ for Al_2ZnZr. Therefore, using the same logic, the a_p of $Al_{(3-x)}Zn_xZr$ is $0.408 < a_p < 0.4099\ nm$, depending on the atomic fraction of Zn present in the precipitate phase (where $x \ll 1$). This suggests that adding Zn slightly increased the lattice mismatch of $Al_{(3-x)}Zn_xZr$/α-Al to $+0.75 < \delta < +1.22$. Hence, the $Al_{(3-x)}Zn_xZr$ precipitate phase yielded a higher ϵ and corresponding coherency strengthening than Al_3Zr.

(c) $\langle R \rangle$: According to Table 7, the precipitate mean radius of $Al_{(3-x)}Zn_xZr$ is slightly higher than that of Al_3Zr, which certainly enhanced $\Delta\sigma_{ms}$, $\Delta\sigma_{cs}$, and $\Delta\sigma_{or}$.

In summary, the very small fraction of Zn present in the precipitate phase increased ΔG, ϵ, $\langle R \rangle$, and the corresponding $\Delta\sigma_{ms}$, $\Delta\sigma_{cs}$, and $\Delta\sigma_{or}$ strengthening mechanisms. However, based on the heat treatment curve in Figure 31, the additional precipitation strengthening gained from $Al_{(3-x)}Zn_xZr$ relative to the Al_3Zr must be minimal. Zn solute remaining in solid solution was responsible for the majority of the microhardness difference between both specimens, through solid solution strengthening. With this understanding, the microhardness behavior of 3.5Zn0.2Zr relative to 0.2Zr, Figure 31, due to Zn addition was qualitatively interpreted in three (3) stages: Pre-peak, overage, and dissolution, Table 9.

At the pre-peak stage (between as-cast and peak age conditions), both alloys maintained a uniform microhardness difference. Their microhardness values followed parallel paths

from as-cast to 450 ℃. This indicates that most of the microhardness difference came from solid solution strengthening, as a result of adding Zn. As the precipitates grew in 3.5Zn0.2Zr, very few Zn atoms migrated into the precipitate phase as indicated in Table 8. Naturally, the solid solution strengthening from the remaining Zn solute in solution slightly reduced. This lost strength was compensated for by the slightly increased precipitation strengthening from the $Al_{(3-x)}Zn_xZr$ precipitates relative to Al_3Zr. Thereby maintaining a fairly constant microhardness difference between 3.5Zn0.2Zr and 0.2Zr from as-cast to peak age temperatures.

During the overage stage, some of the Zn dissolved from the precipitate phase back into the matrix as a result of increasing diffusivity and solid solubility of Zn in Al. This is confirmed by the lower Zn concentration in the precipitate phase at 500 and 600℃ relative to 450℃ (Table 8). The gradual dissolution of Zn from the precipitate phase directly led to a reduced ϵ, ΔG, and corresponding precipitation strengthening from the $Al_{(3-x)}Zn_xZr$ precipitate relative to Al_3Zr. Therefore, the microhardness of 3.5Zn0.2Zr converged towards 0.2Zr. This could explain why a steeper microhardness drop was observed for 3.5Zn0.2Zr immediately after the peak age condition. Hence, in addition to the gradual Zn dissolution, the higher coarsening rate of precipitates formed in 3.5Zn0.2Zr relative to 0.2Zr could be simultaneously responsible for the faster strength reduction observed during the early overaging convergence stage.

At the later stage of heat treatment (significant dissolution), the precipitates had experienced pronounced coarsening. At this stage, the magnitude of microhardness derived from precipitation is expected to be insignificant, as most of the microhardness of the alloys depended on solid solution, similar to the as-cast condition. Therefore, the microhardness difference between 3.5Zn0.2Zr and 0.2Zr was gradually restored due to solid solution strengthening from the Zn already dissolved into the matrix. These stages are summarized in Table 9.

Table 9. Qualitative interpretation of the influence of Zn addition on the isochronal aging behavior of 3.5Zn0.2Zr with respect to 0.2Zr.

Aging stage	Zn in solid solution	Solid solution strength	ϵ and ΔG	Precipitation strength	Dominant mechanism	Behavior relative to Al_3Zr
Pre-peak	↓	↓	↑	↑	Solid solution	Uniform
Early overage	↑	↑	↓	↓	Precipitation	Converge
Dissolution	↑	↑	↓	↓ (Insignificant)	Solid solution	Diverge

↑: Increasing trend of composition or magnitude; ↓: Decreasing trend of composition or magnitude

Theoretically, it can be confirmed that majority of the microhardness gained from Zn addition to Al-Zr alloy comes from solid solution strengthening. Using equations (1-4), we estimated the microhardness of 3.5Zn0.2Zr derived from solid solution strengthening, as a result of adding 3.5 wt.% Zn to Al-Zr alloy as 71.4 MPa. This is slightly higher than the observed microhardness difference between as-cast 0.2Zr and 3.5Zn0.2Zr, 64MPa. The values used in this estimation are, $G_{Al\ matrix} = 25.4\ GPa$, $G_{Zn\ solute} = 39.5\ GPa$, $c_{Zn\ solute} = 1.5\ at.\%$, $a_{Al\ matrix} = 0.572\ nm$ and $a_{Zn\ solute} = 0.495\ nm$. Because, both atoms have similar closed packed structures, the (111) and z-axis lattice constant of Al and Zn were used, respectively. It is however important to note that the estimate could vary over a large range based on minor changes in the values of the parameters used, especially $G_{Zn\ solute}$ and $a_{Zn\ solute}$. This makes this approach less reliable.

5.4.2 Stability of $L1_2$ precipitates with Zn addition

As expected, equilibrium $D0_{23}$ precipitates were not observed in the specimens after isochronal aging at 450 ℃ (Figure 35). Such transitions usually take place at higher temperatures[30, 31]. However, other factors, including aging time and dislocation density present in the specimen, could also impact the temperature of transformation and kinetics. Zedalis and Fine[87] observed the $L1_2 \rightarrow D0_{23}$ transformation in 95 %CW Al-0.24Zr (at. %) after aging at 450 ℃. The relatively lower transformation temperature at which they

observed this transformation was due to the high dislocation density from initial cold rolling, which served as heterogeneous sites for such transformation to take place more easily.

At 600 ℃, significant precipitate coarsening and overaging occurred in 0.2Zr and 3.5Zn0.2Zr specimens as represented by the Vickers microhardness results shown in Figure 31. The specimens were examined under the SEM and TEM microscope to study the influence of Zn on stabilizing the $L1_2$ precipitate structure at higher aging temperatures. At this temperature, the $L1_2 \rightarrow D0_{23}$ transformation observed in overaged 0.2Zr was extensive along the dendritic border, interdendritic channels, and on dislocation sites, as shown in Figure 36(e) and Figure 37(a). However, many precipitates maintained their $L1_2$ structure, especially in the dendritic center (Figure 36(e)). A similar transformation was observed for $Al_{(3-x)}Zn_xZr$ in the 3.5Zn0.2Zr alloy after undergoing the same aging procedure, Figure 36(c) and Figure 37(b). This confirms that the presence of Zn in the precipitate phase did not prevent the eventual transformation from occurring.

The specimens were examined after an intermediate overaging temperature (500℃) to determine if Zn addition has any influence on delaying the isochronal aging temperature of the $L1_2 \rightarrow D0_{23}$ transition. Few disk-like $D0_{23}$ precipitates were spotted in both specimens after thorough examination. Therefore, Zn did not delay the precipitate phase transformation. The only minor claim that can be made is that the presence of Zn in the precipitate phase reduced the number of visible disk-like $D0_{23}$ precipitates present after aging at 500℃. This was evident because after examining three 0.2Zr specimens, the average number of $D0_{23}$-Al_3Zr precipitates found was 13, which is about 3 times as much as the four (4) $D0_{23}$- $Al_{(3-x)}Zn_xZr$ found in 3.5Zn0.2Zr specimens.

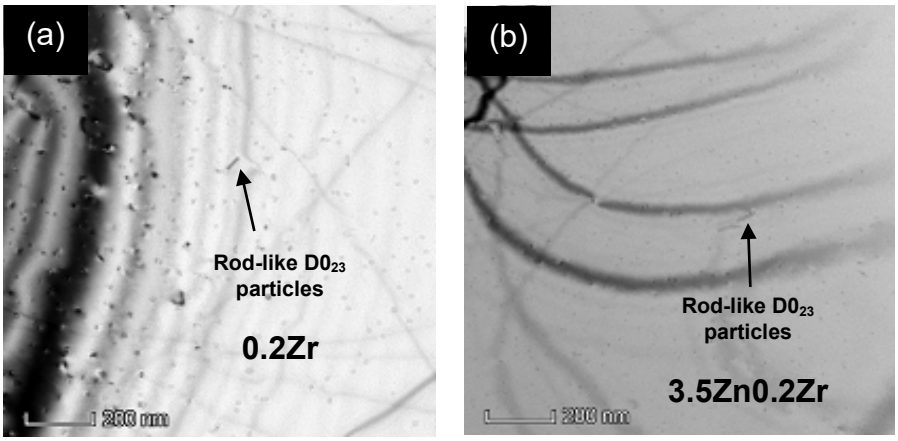

Figure 42. TEM showing some of the few spotted $D0_{23}$ precipitates embedded in the midst of several $L1_2$ phases, after isochronal aging at 500 ℃, (a) 0.2Zr and (b) 3.5Zn0.2Zr.

5.4.3 Effect of Zn on nucleation, growth, coarsening

In both specimens, the first sign of nucleation occurred after isochronal aging at 350℃. This implies that the inclusion of Zn did not have any influence on the incubation time required for nucleation under this aging condition. This is probably because Zr solute first precipitated out of solid solution before Zn, due to its much lower solid solubility in Al. Hence, Zr served as heterogeneous sites for nucleation to occur. Similar to 0.2Zr, the 3.5Zn0.2Zr alloy reached peak microhardness at ~450℃, after undergoing the same isochronal aging procedure. Therefore, the addition of Zn into the precipitate phase did not cause any significant shift in the peak microhardness temperature.

The particle growth occurred by long-range solute atomic diffusion through the matrix phase across the phase boundary and into the nucleus. The diffusivities of Zn and Zr in Al are estimated by an Arhenius relationship, $D = D_o \exp(-Q/R_g T)$, where $Q = 121$ and 242 kJ mol^{-1} and $D_o = 2.59 \times 10^{-5}$ and 7.28×10^{-2} m^2 s^{-1} for Zn and Zr, respectively[12, 29, 46, 47]. At 450 ℃, where peak microhardness occurred for both alloys, the diffusivities of Zn and Zr in α-Al are 4.69×10^{-11} and 2.38×10^{-19} m^2/s, respectively. Clearly, since Zn has a higher diffusivity in α-Al than Zr, it would be expected that precipitates in 3.5Zn0.2Zr would grow and coarsen at a much faster rate than 0.2Zr. From observation, the average precipitate size of $Al_{(3-x)}Zn_xZr$ was slightly bigger than

Al_3Zr at the various aging temperature levels examined. At $450℃$, the mean size $\langle R \rangle$ of $Al_{(3-x)}Zn_xZr$ precipitates located in the interdendritic channel and dendritic centers were $2.45\,nm$ and $6.5\,nm$, while those of Al_3Zr were approximately $2.2\,nm$ and $5.5\,nm$, respectively. The $Al_{(3-x)}Zn_xZr$ precipitates present in the interdendritic channels have a mean size of $10.0\,nm$ and $30.0\,nm$ at $500℃$ and $600℃$, respectively, while Al_3Zr increased to $8.5\,nm$ and $23.0\,nm$, respectively. These precipitate sizes show that the inclusion of Zn in the Al_3Zr precipitate phase slightly increased the precipitate growth and coarsening rate.

5.4.4 Electrical conductivity

The solute atoms (Zr and/or Zn) within the matrix distort the lattice parameter of α-Al and serve as local electron scattering lattice sites[51]. The source of distortion is the difference between the atomic radii of Al and the solute species (Zn and Zr). Lattice distortion hinders the motion of electrons carrying current when an electric field is passed through the specimen. Due to its high solid solubility in Al, only a small at. % of Zn (together with majority of Zr atoms) precipitated out of solid solution during aging. The remaining Zn in solid solution is responsible for the electrical conductivity difference (+4.6 MS/m) between 0.2Zr and 3.5Zn0.2Zr. At the peak-aged condition, the contribution of the remaining Zn solute to the lattice distortion and number of local electron scattering sites within the matrix is slightly reduced (but still significant), since only a few Zn atoms migrated into the precipitate phase.

At temperatures $\geq 500℃$, the steady decrease of electrical conductivity was due to overaging and the subsequent dissolution of the precipitate phase back into the matrix. The electrical conductivities gained as a result of precipitation hardening are similar; +1.9 MS/m for 0.2Zr and +1.7 MS/m for 3.5Zn0.2Zr. This suggests that similar volume fractions of precipitates were formed in both alloys. In summary, the addition of Zn to Al-Zr did not increase the precipitate volume fraction. The uniform conductivity difference between 0.2Zr and 3.5Zn0.2Zr at as-cast and peak-aged states also supports this suggestion.

5.5 Summary and conclusions

This study focused on the effect of Zn on electrical conductivity, mechanical properties, and potential $L1_2$ phase stability of Al-Zr alloy by comparing precipitation of Al_3Zr in 0.2Zr to $Al_{(3-x)}Zn_xZr$ in 3.5Zn0.2Zr after isochronal aging from 150 – 600 ℃.

The addition of 3.5 wt.% of Zn to Al-Zr has been shown to increase the peak microhardness of the alloy. However, the majority of the gained microhardness is due to solid solution strengthening from the remaining Zn in the matrix. The conversion of the precipitate phase from Al_3Zr to $Al_{(3-x)}Zn_xZr$ by Zn inclusion also increased the magnitude of the change in shear modulus, ΔG, and mismatch parameter, ϵ, between the precipitate and matrix, thus increasing the contribution of modulus mismatch and coherency strengthening to the peak strength of the alloy. The steep microhardness decline of 3.5Zn0.2Zr relative to 0.2Zr, observed during overaging (isochronal aging) was due to the combination of enhanced precipitate coarsening and dissolution of Zn from precipitate phase after long exposure to high temperature.

Results from electrical conductivity and microhardness measurements show that adding Zn to the Al-Zr alloy had no significant impact on the volume fraction of the precipitates formed. This conclusion was made because both alloys displayed similar increases in electrical conductivity (mean value ~ +1.8 MS/m) and microhardness (mean value ~ +138 MPa) from as-cast to peak-aged conditions.

The tensile strengths of “AA+CW” and “CW” specimens come from dislocation-precipitate and dislocation-solute interactions, because coherent precipitates and solutes generate strain fields that obstruct the movement of dislocations. The strength difference between 0.2Zr and 3.5Zn0.2Zr wire specimens in the “CW” condition was 26 MPa. This difference was possibly due to dislocation-Zn solute interaction in 3.5Zn0.2Zr, which is non-existent in 0.2Zr. In the case of “AA+CW”, the tensile strength of 3.5Zn0.2Zr was 41 MPa more than 0.2Zr. Which is an additional 15 MPa increase from the “CW” condition. This indicates that prior aging was slightly more effective in improving the strength of 3.5Zn0.2Zr relative to 0.2Zr. Since it is now established that the addition of Zn to Al-Zr

does not increase precipitate volume fraction, it could therefore be concluded that $Al_{(3-x)}Zn_xZr$ generated an improved dislocation-precipitate interaction due to its increased precipitate/matrix lattice mismatch and coherency strengthening relative to Al_3Zr. After thermal aging at 600 ℃ for 5 h, 0.2Zr retained 95 % of its as-wiredrawn strength, while 3.5Zn0.2Zr retained 84 %. The strength of the specimens remained almost constant after thermal aging for 15 h. Thus, the initial softening observed was due to dislocation annihilation.

The microstructures of 0.2Zr and 3.5Zn0.2Zr specimens were characterized by microsegregation of the Zr solute species after solidification. This led to regions of varying number density of precipitates formed as well as precipitate size gradients across the specimen. This segregation caused the formation of dendritic core/interdendritic channels in the microstructure[30]. At 450℃, the larger $L1_2$ precipitates were formed in the interdendritic channels while smaller ones were situated in the rich dendritic region. Previous studies of Al-Zr alloy have shown that some of the $L1_2$ precipitates transform to $D0_{23}$ during isochronal and isothermal aging at temperatures > 475℃. This transformation was observed in 0.2Zr and 3.5Zn0.2Zr at 500 and 600℃. EDX data shows that the Zn composition in the $Al_{(3-x)}Zn_xZr$ particles was higher at 450 ℃ relative to 500 and 600 ℃. This confirms the dissolution of Zn between these temperatures, which partly explains why a steeper microhardness reduction was observed in 3.5Zn0.2Zr with respect to 0.2Zr.

Chapter 6: Influence of Zn on ductility and creep rate of precipitation hardened Al alloys

6.1 Abstract and Introduction

6.1.1 Abstract

Generally, the enhancement of alloy strength leads to reduced ductility. However, the addition of Zn to Al-Zr is shown to have the potential to increase the ductility of the alloy before and after thermal aging experiments. This is determined from percent elongation (%EL) data of Al-Zr and Al-Zn-Zr, when the alloy specimens are cold worked after aging (AA+CW) and as-cast (CW). The cold worked alloys are annealed at 300°C for 5 and 15h. Finally, %EL results from the thermally aged alloys also show similar enhanced ductility due to Zn addition. However, Zn reduces the creep resistance of Al-Zr alloy.

6.1.2 Introduction

Aluminum alloys are most widely used for aircrafts and automobiles due to their low mass and density. Though, these alloys are known to have lower strength relative to steel, which limits their applications in the transportation industry. Due to low strength, mechanism such as precipitation and work hardening have been employed to make them stronger. Zr solute offers one of the highest strengthening potential in precipitation strengthened Al-Zr relative to other transition metals.

The strength of the precipitation-strengthened alloy improves as solute concentration is increased, making the alloy more brittle. The enhanced strength is due to increased dislocation retardation from higher precipitate volume fraction. Hence, the process of increasing the strength of Al-Zr results in reduced ductility. The reduced ductility of the precipitation-strengthened alloy make it less reliable for transportation and minor structural applications. Thus, the challenge is to develop an alloy with simultaneous improvement of strength and ductility.

Several studies have shown that enhanced ductility of Al alloys can be achieved through Zn addition. Hu et al. reported that increasing the Zn content from 0 – 15 wt.%, can effectively enhance tensile elongation of the alloy from 10 to 30%. This was due to increased rate of work hardening and the presence of several fine slip bands[88].

The objective of this study is to investigate the influence of Zn addition to Al-Zr on the ductility and creep resistance.

6.2 Experimental design for %EL

The %EL experiment was performed in conjunction with the tensile test experiment, using the Instron tensile test instrument and Futek maximum load capacity of 10,000 lbs, as detailed in sub-sections 3.4.3 and 5.2. In this study, ductility measurements were taken on the CW and AA+CW alloy specimens simultaneously while performing tensile test. During the tensile tests experiment described in section 5.2, a 25.4 mm (1-inch) Epsilon extensometer with sharp knife-edge contact was clamped to the 38.1 mm gage length of each alloy tensile specimen (design B tensile bar). The diameter of the gage length region of the specimens is 3.8 mm. The extensometer readings represent stain to failure. Using a uniform diameter tensile bar led to inconsistent ductility measurements, hence, the need to use design B tensile bar specimens.

Creep test was performed on 203 mm (8 inches) long, as-wiredrawn-AA+CW (0.2Zr and 3.5Zn0.2Zr) specimens, before and after thermal aging (at 300°C for 5 h), using an Instron screw-driven tensile testing frame. For all creep experiments, a gage length, constant stress, constant temperature and duration of 101.6 mm (4 inches), 40 MPa, 250°C and 2.5 h were used.

6.3 Results and discussion

Comparing the %EL of 0.2Zr and 3.5Zn0.2Zr specimens in CW to their corresponding AA+CW condition (as-wiredrawn) indicates that heat treatment of the alloys before cold work makes them slightly less ductile, Figure 43(a). For instance, at as-wiredrawn condition, 0.2Zr and 3.5Zn0.2Zr specimens have ductility of 4.7 and 6.3 %EL after CW, respectively. After AA+CW, these values reduced to 3.5 and 5.5 %EL respectively. This

result also indicates that the addition of Zn enhanced the ductility of Al-Zr at as-wiredrawn condition. The addition of 3.5 wt.% Zn enhanced the %EL of 0.2Zr from 4.7 and 3.5 %EL to 6.3 and 5.5 %EL for 3.5Zn0.2Zr at CW and AA+CW respectively.

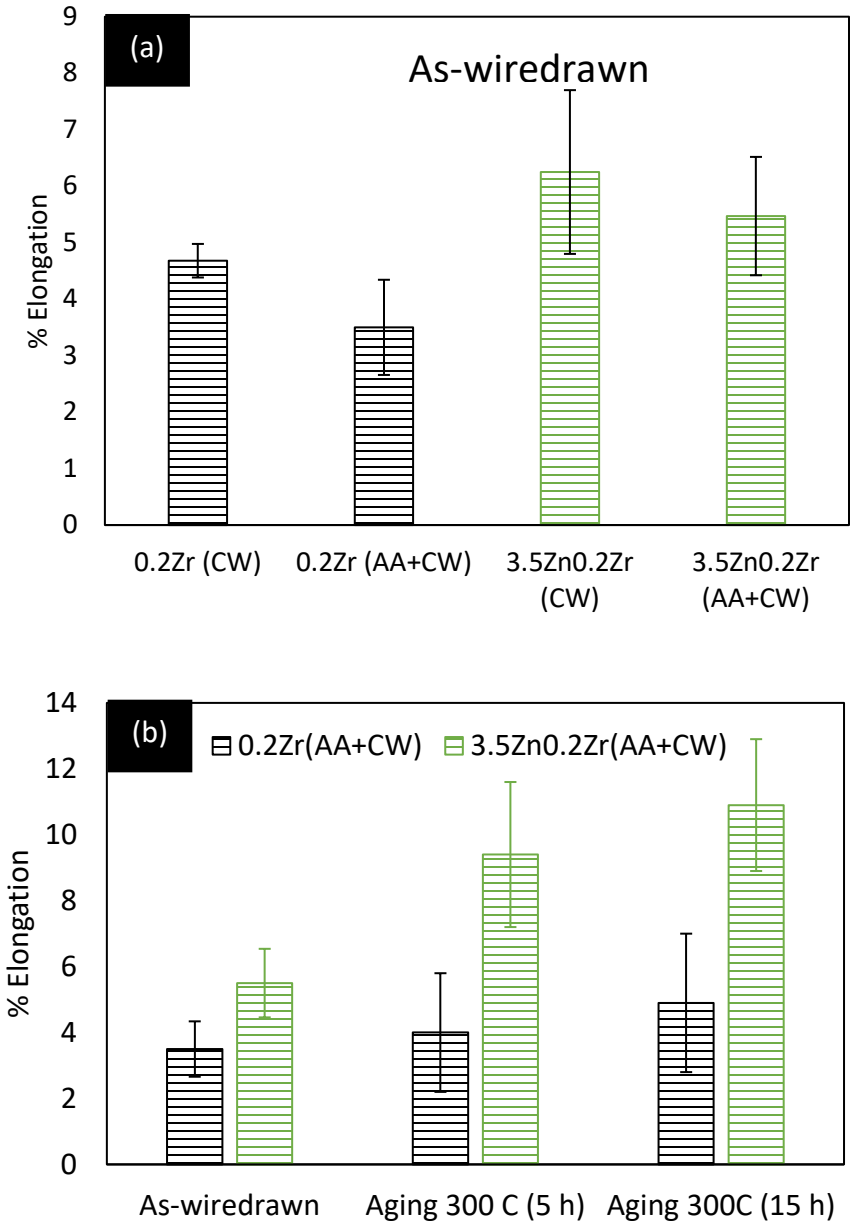

Figure 43. % Elongation measurement of 0.2Zr and 3.5Zn0.2Zr at CW and AA+CW conditions, (a) as-wiredrawn (b) After thermal aging experiment at 300°C for 5 and 15 h.

According to Figure 43(b), annealing the AA+CW alloys during thermal aging, widens the difference in %EL between 0.2Zr and 3.5Zn0.2Zr. The difference in strain to failure ($^{\%EL}/_{100}$), between both AA+CW alloys increased from 0.02 (as-wiredrawn) to 0.054 and 0.06 after thermal aging for 5 and 15 h, respectively.

Creep test was performed on 0.2Zr and 3.5Zn0.2Zr before and after thermal aging, to determine the impact of adding Zn on the creep rate of Al-Zr alloy. According to the data in Table 10 and Figure 44, the inclusion of 3.5 wt.% Zn to 0.2Zr increased the creep rate in as-wiredrawn condition, from 2.9×10^{-6} to 5.4×10^{-6}. The annealed wires increased from 1.7×10^{-6} in 0.2Zr to 5.1×10^{-6} in 3.5Zn0.2Zr.

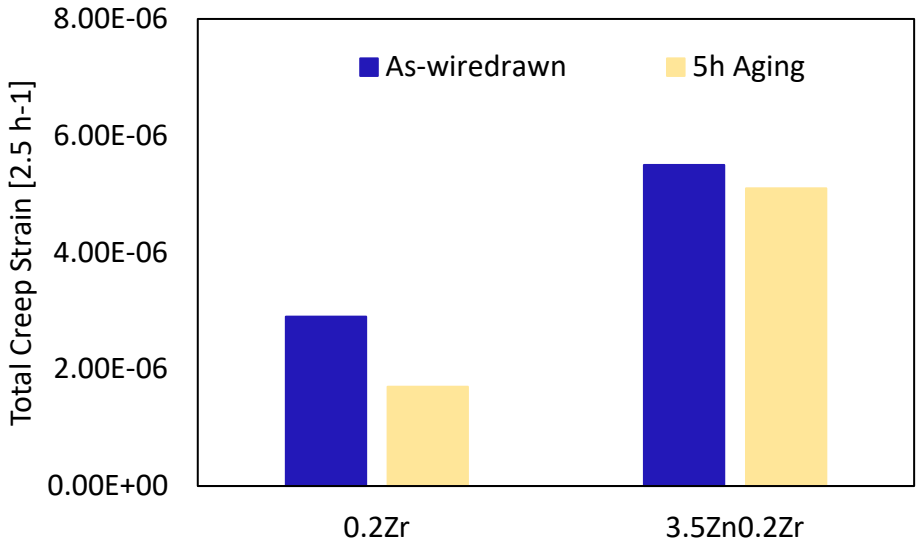

Figure 44. Total creep strain of 0.2Zr and 3.5Zn0.2Zr at as-wiredrawn and after 5 h thermal aging. The creep test was performed at constant stress, temperature and duration of 40 MPa, 250°C and 2.5 h.

Table 10. Creep strain rate of 0.2Zr and 3.5Zn0.2Zr alloys

	Creep strain rate s^{-1} (40 MPa, 250 ℃)	
	As-wiredrawn	After 5 h aging
0.2Zr	2.9×10^{-6}	1.7×10^{-6}
3.5Zn0.2Zr	5.4×10^{-6}	5.1×10^{-6}

02Zr, at overaging temperature, > 450 ℃. However, significant deformation of the alloys could have led to coarsening at a much lower temperature (250 ℃), during the creep test experiment, especially in 3.5Zn0.02Zr, because of the high diffusivity of Zn in Al.

6.4 Summary and conclusions

Comparing CW and AA+CW alloys showed that aging the alloys before cold work raised the tensile strength of 0.2Zr and 3.5Zn0.2Zr. The increased strength from precipitation led to reduced ductility of the alloys.

3.5Zn0.2Zr experienced slightly higher ductility than 0.2Zr after as-wiredrawn and thermal aging conditions, even though it has a better strength. This indicates that the addition of Zn could be responsible for the enhanced ductility as a result of reduced stacking fault energy of the alloy.

A higher total creep strain was observed in 3.5Zn0.2Zr relative to 0.2Zr. This could be attributed to enhanced precipitate coarsening in 3.5Zn0.2Zr compared to 0.2Zr, at such low temperature, 250 ℃. The high diffusivity of Zn in Al could be responsible for the enhanced coarsening in 3.5Zn0.2Zr relative to 0.2Zr.

Chapter 7: Performance summary of Al-Zn-Zr and Al-Zn-Ni and AA1350

7.1 Introduction

The electrical conductivity of Al alloy 1350 (AA1350) currently used for power transmission is between 34.9 (extra hard H-19) and 35.7 MS/m (annealed), which is very close to that of pure Al (36.9 MS/m). This leaves little room for developing an Al alloy with improved electrical conductivity, while subsequently increasing strength. Al-Zn-Zr is an alternate Al alloy with excellent thermal resistance, creep and strength but a lower electrical conductivity relative to Al-Zn-Ni and AA1350. Al-Zn-Ni has a slightly better strength and thermal resistance than AA1350 but similar electrical conductivity. In this chapter the performance of the two new alloys are compared to AA1350.

To make direct comparison between the potential of the new alloys and AA1350, some of the 25 lbs commercial AA1350 rods received from General Cable were cut, re-casted and prepared using similar melting, polishing and cold work procedures used for Al-Zn-Zr and Al-Zn-Ni alloys (detailed in chapter 4 and 5). Therefore, the AA1350 detailed in this chapter is not considered extra hard-H19 alloy. Where available, data for AA1350-H19 and AA1350-O were also included in the plot for comparison with currently used electrical conductors.

7.2 Mechanical and electrical properties

7.2.1 Microhardness and eddy current

According to Figure 45, the microhardness of AA1350 is 248 MPa at as-cast. It gradually reduced during isochronal aging to 235 and 221 MPa at 250 and 450 °C, respectively. This shows that AA1350 does not form any strengthening phase hence no precipitation hardening was observed. Henceforth, most of its strength was derived from solid solution

strengthening via impurities and cold work. The microhardness of 0.2Zr (403 MPa), 3.5Zn0.1Ni (356 MPa) and 3.5Zn0.2Zr (459 MPa) were much higher at their respective peak strength. Both alloys are capable of forming secondary strengthening phases responsible for the enhanced microhardness during aging. As expected, there are no microhardness data for as-cast AA1350-H19 and AA1350-O alloys, since these alloys are cold worked wires.

Similarly, increased eddy current conductivity was observed for all the alloys in this study at their respective peak condition. Though, only a slight increase was observed for 3.5Zn0.1Zr. As expected, these eddy current conductivity values were much lesser than AA1350. For instance, at peak condition, 0.2Zr, 2.5Zn0.2Zr, 3.5Zn0.2Zr and 3.5Zn0.1Ni experienced a peak eddy current conductivity of 34, 32, 30 and 33 MS/m, respectively, relative to 36 MS/m for AA1350. The slight increase in eddy current conductivity of AA1350 was due to annealing and not precipitation.

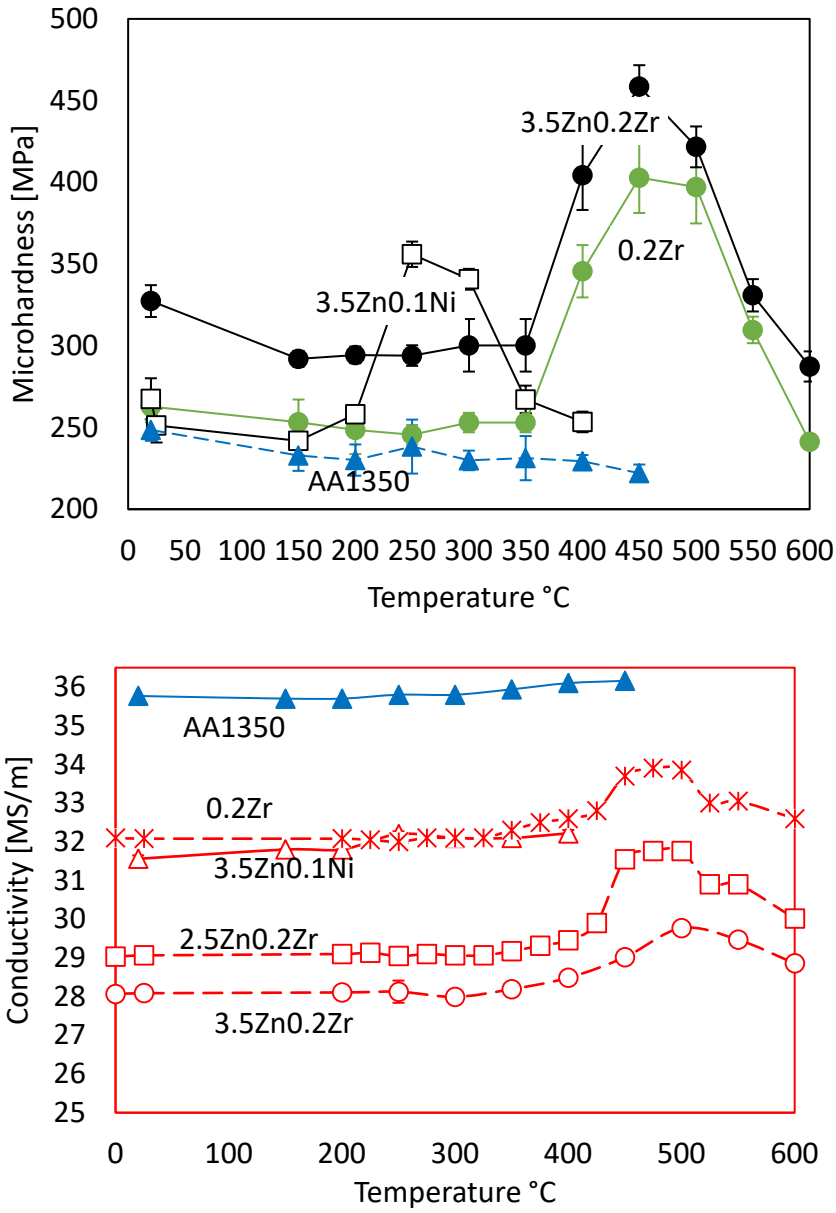

Figure 45. Microhardness and conductivity comparison of Al-Zn-Ni and Al-Zn-Zr to AA1350. Highest peak strength was observed for Al-Zn-Zr, followed by Al-Zn-Ni and AA1350. No peak strength was observed for AA1350 due to lack of strengthening phase formation during aging. As predicted by DFT, Al-Zn-Zr alloy experiences the lowest conductivity.

7.2.2 Tensile strength and conductivity

The tensile strengths and electrical conductivities of several compositions of Al-Zn-Ni and Al-Zn-Zr alloy wires were plotted together with AA1350 (re-casted in the laboratory) to observe how the strength gained compares to electrical conductivity lost by each alloy. The alloy composition of Al-Zn-Ni were varied from 0.5 – 3.5 wt.% Zn, while Ni composition was kept constant at 0.1 wt.%. The 0.2Zr and 3.5Zn0.2Zr alloys were fabricated for Al-Zn-Zr alloys. Online data for currently used AA1350-H19 and -O alloys was also included in the plot, to show that additional increased strength can be achieved for the new alloys if they were extra hardened.

From Figure 46, the Al-Zn-Ni alloys have better strengthening potential but slightly lower electrical conductivity relative to AA1350. However, the percent tensile strength gained is more than 3 × the percent electrical conductivity lost, relative to AA1350. For instance, the tensile strengths of 0.5Zn0.1Ni, 2.5Zn0.1Ni and 3.5Zn0.1Ni are 6, 13 and 27% higher than AA1350, respectively. The electrical conductivity of AA1350 is 0, 3, 6% higher than that of 0.5Zn0.1Ni, 2.5Zn0.1Ni and 3.5Zn0.1Ni. This confirms DFT data which indicates that Zn and Ni have very minimal effect on electrical conductivity of Al, Figure 18.

Figure 46 shows that Zr has a better precipitation strengthening potential relative to Ni. However, due to the greater negative impact of Zr on electrical conductivity, higher electrical conductivity was lost relative to AA1350. The tensile strength and electrical conductivity of 3.5Zn0.2Zr is 62% higher and 14% lower than AA1350. The percent tensile strength gained is more than 4 × the percent electrical conductivity lost, relative to AA1350.

By comparing AA1350-H19, AA1350-O to the AA1350 re-casted in the laboratory, it can be shown that extra hardening of the AA1350 would yield additional tensile strength of 35 MPa with only ~0.4 MS/m electrical conductivity lost. This indicates that if the new Al-Zn-Zr and Al-Zn-Ni alloys were extra hardened, higher strength would have been recorded. It will however be expected that great reduction in the existing %EL would occur. On the

other hand, AA1350-O has a much lower tensile strength relative to AA1350-H19 and AA1350, due to annealing.

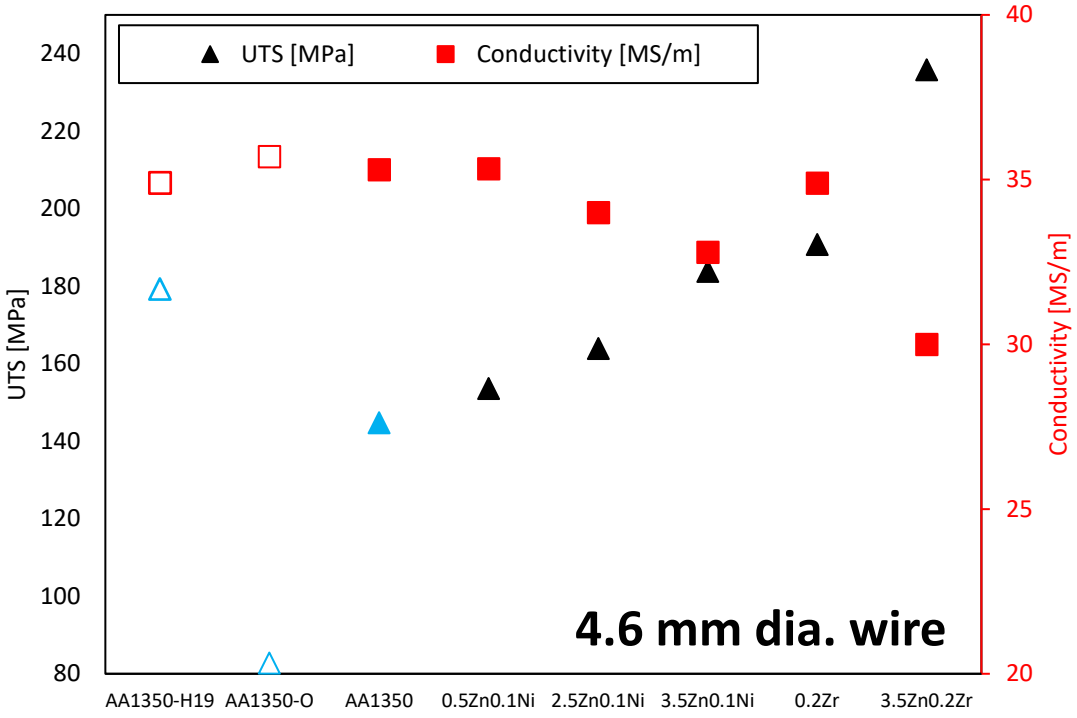

Figure 46. Tensile strength and electrical conductivity plot comparison. Al-Zn-Zr containing alloys show greater strengthening potential relative to Al-Zn-Ni and AA1350 alloys but lower electrical conductivity. The data also shows that the new alloys have improved strength relative to AA1350 and currently used AA1350-H19 and -O.

7.3 Summary and conclusions

Unlike Al-Zn-Ni and Al-Zn-Zr, AA1350 does not respond to aging, because it does not form any strengthening phase. Fe is the major impurity composition (~0.4 wt.%) present in AA1350 and it does not form secondary phase in Al.

The additional strengthening achieved in Al-Zn-Ni and Al-Zn-Zr is 3 × and 4 × electrical conductivity lost, relative to AA1350.

References

1. *Aluminum to replace copper as a conductor in on-board power systems*. 2011 Retrieved October 29, 2018; Available from: www.sciencedaily.com/releases/2011/02/110207124035.htm.

2. Djukanovic, G. *Copper vs Aluminium – substitution slows but continues*. 2016 Retrieved October 29, 2018; Available from: https://aluminiuminsider.com/copper-vs-aluminium-substitution-slows-but-continues/.

3. Hasnip, P.J., et al., *Density functional theory in the solid state.* Royal Society Publishing, 2014.

4. Shi, D., et al., *First-principles studies of Al–Ni intermetallic compounds.* Journal of solid state chemistry, 2009. 182(10): p. 2664-2669.

5. *Aluminum Conductor Steel Supported (ACSS)*. Retrieved October 29, 2018; Available from: https://www.southwire.com/ProductCatalog/proddetail.jsp?htmlpreview=true&token=29&desc=A.

6. K.E. Kniplng, D.C.D., D.N. Seidman, *Precipitation evolution in Al-Zr and Al-Zr-Ti alloys during aging at 450 ℃ compared to 600 ℃.* Acta Materialia, 2008. 58: p. 1182–1195.

7. K.E. Knipling, D.C.D., D.N.Seidman *Precipitation evolution in Al-Zr and Al-Zr-Ti alloys during isothermal aging at 375 – 425 ℃.* Acta Materialia, 2008. 56: p. 114 – 127.

8. K.E. Knipling, R.A.K., C.P. Lee, D.C. Dunand, D.N. Seidman, *Precipitation evolution in Al-0.1Sc, Al-0.1Zr and Al-0.1Sc-0.1Zr (at. %) alloy during isochronal aging.* Acta Materialia, 2010. 58: p. 5184–5195.

9. K.E. Knipling, D.C.D.a.D.N.S., *Nucleation and Precipitation Strengthening in Dilute Al-Ti and Al-Zr Alloys.* The Minerals, Metals and Materials Society and ASM International, 2007. 38A: p. 2552 – 2563.

10. K. Knipling, D.D., D. Seidman, *Criteria for developing castable creep resistant aluminum-based alloys.* 2006: p. 246-265.

11. *Chemicool Periodic Table*. 2012 Retrieved October 30, 2018; Available from: https://www.chemicool.com/elements.

12. Fadayomi, O., et al., *Investigation of Al-Zn-Zr and Al-Zn-Ni alloys for high electrical conductivity and strength application.* Materials Science and Engineering A, 2019. 743: p. 785-797.

13. Hatch, J.E., *Aluminum: Properties and Physical Metallurgy.* American Society for Metals, 1984.

14. G. Ghosh, A.v.d.W., M. Astra, *First principles phase stability calculations of L12, D022 and D023 structures in Al-TM (=Ti,Zr,Hf)-Zn systems.* Proceedings of an International Conference on Solid-Solid Phase Transformation in Inorganic Materials, 2005.

15. G. Ghosh, A.v.d.W., M. Astra, *First principles phase stability calculations of pseudobinary alloys of (Al,Zn)3Ti with L12, D022 and D023 structures.*

16. Greenwood, D., *The Boltzmann equation in the theory of electrical conduction in metals.* Proceedings of the Physical Society, 1958. 71(4): p. 585.

17. Kubo, R., *Statistical-mechanical theory of irreversible processes. I. General theory and simple applications to magnetic and conduction problems.* Journal of the Physical Society of Japan, 1957. 12(6): p. 570-586.

18. Ghosh, G., A. Van De Walle, and M. Asta, *First-Principles Phase Stability Calculations of Pseudobinary Alloys of (Al, Zn) 3 Ti with L1 2, D0 22, and D0 23 Structures.* Journal of phase equilibria diffusion, 2007. 28(1): p. 9-22.

19. Sholl, D. and J.A. Steckel, *Density functional theory: a practical introduction*. 2011: John Wiley & Sons.

20. Pelleg, J., *Mechanical properties of materials*. Vol. 190. 2012: Springer Science & Business Media.

21. Lu, L., et al., *Ultrahigh strength and high electrical conductivity in copper.* Science, 2004. 304(5669): p. 422-426.

22. Gladman, T., *Precipitation hardening in metals.* Materials Science and Technology, 1999. 15(1): p. 30-36.

23. Gladman, T., *Precipitation hardening in metals.* Materials Science Technology, 1999. 15(1): p. 30-36.

24. Allison, J., *Integrated computational materials engineering: A perspective on progress and future steps.* JOM, 2011. 63(4): p. 15-18.

25. Ghosh, G. and M. Asta, *First-principles calculation of structural energetics of Al–TM (TM= Ti, Zr, Hf) intermetallics.* Acta Materialia, 2005. 53(11): p. 3225-3252.

26. Wang, J., et al., *First-principles calculations of binary Al compounds: Enthalpies of formation and elastic properties.* Calphad, 2011. 35(4): p. 562-573.

27. Chrifi-Alaoui, F., et al., *Enthalpies of formation of the Al–Ni intermetallic compounds.* Journal of Alloys Compounds, 2004. 364(1-2): p. 121-126.

28. Yuan, X.-L., et al., *The first-principles calculations for the elastic properties of Zr2Al under compression.* Journal of Alloys Compounds

2011. 509(3): p. 769-774.

29. Knipling, K.E., D.C. Dunand, and D.N. Seidman, *Criteria for developing castable, creep-resistant aluminum-based alloys–A review.* Zeitschrift für Metallkunde, 2006. 97(3): p. 246-265.

30. Knipling, K.E., D.C. Dunand, and D.N. Seidman, *Precipitation evolution in Al–Zr and Al–Zr–Ti alloys during aging at 450–600 C.* Acta Materialia, 2008. 56(6): p. 1182-1195.

31. Knipling, K.E., D.C. Dunand, and D.N. Seidman, *Precipitation evolution in Al–Zr and Al–Zr–Ti alloys during isothermal aging at 375–425 C.* Acta Materialia, 2008. 56(1): p. 114-127.

32. Cubiotti, G., et al., *The electronic structure of Al3Ni.* Journal of Physics: Condensed Matter, 1995. 7(25): p. 4865.

33. Knipling, K.E., et al., *Precipitation evolution in Al–0.1 Sc, Al–0.1 Zr and Al–0.1 Sc–0.1 Zr (at.%) alloys during isochronal aging.* Acta Materialia, 2010. 58(15): p. 5184-5195.

34. Fine, M.E., et al., *Alloy Design of Nanoscale Precipitation Strengthened Alloys: Design of a Heat Treatable Aluminum Alloy Useful to 400C*, in *Final Report for Department of Energy Grant No. DE-FG02-02ER45997,"* 2006, Northwestern University.

35. Fleischer, R. *High Temperature Ordered Intermetallic Alloys III, CT Liu, AI Taub, NS Stoloff, and CC Koch, eds*. in *Materials Research Society Symposia Proceedings, Materials Research Society*. 1989. Pittsburgh, PA.

36. Zhang, S., J. Nic, and D. Mikkola, *New cubic phases formed by alloying Al3Ti with Mn and Cr.* Scripta Metallurgica et Materialia, 1990. 24(1): p. 57-62.

37. Carlsson, A. and P. Meschter, *Relative stability of LI 2, DO 22, and DO 23 structures in MAl 3 compounds.* Journal of Materials Research, 1989. 4(5): p. 1060-1063.

38. Kresse, G., M. Marsman, and J. Furthmüller, *Vienna Ab initio Simulation Package (VASP), the guide Computational Materials Physics.* Faculty of Physics, Universität Wien, Vienna, Austria, 2014.

39. Madsen, G.K. and D.J. Singh, *BoltzTraP. A code for calculating band-structure dependent quantities.* Computer Physics Communications, 2006. 175(1): p. 67-71.

40. Reshak, A. and S. Auluck, *Thermoelectric properties of Nowotny–Juza NaZnX (X= P, As and Sb) compounds.* Computational Materials Science, 2015. 96: p. 90-95.

41. Reshak, A., S.A. Khan, and S. Auluck, *Thermoelectric properties of a single graphene sheet and its derivatives.* Journal of Materials Chemistry C, 2014. 2(13): p. 2346-2352.

42. Reshak, A.H., *Fe 2 MnSi x Ge 1− x: influence thermoelectric properties of varying the germanium content.* RSC Advances, 2014. 4(74): p. 39565-39571.

43. Shojaei, A.R., *Electrical conductivity plus probability of superconductivity in α-cuse/klockmannite; bulk and nano-layers.* Journal of Alloys Compounds, 2015. 632: p. 568-574.

44. *Thermo-Calc Software TCAL5: Al-Alloys v5.0 database*. 2017b 16 January, 2018.

45. Pal, H., S.K. Pradhan, and M. De, *Microstructure and mechanical property of α-Al–Zn–Cu alloys aged at room temperature.* Materials Transactions, JIM, 1995. 36(4): p. 490-495.

46. Fujikawa, S.-I. *Impurity diffusion of scandium in aluminium*. in *Defect and Diffusion Forum*. 1997. Trans Tech Publ.

47. Marumo, T., S. Fujikawa, and K.-i. Hirano, *Diffusion of zirconium in aluminum.* J. Jap. Inst. Light Met., 1973. 23(1): p. 17-25.

48. S. Dias, R.M., A. Seeger, Mater. Sci. Forum, 1987. 15 – 18: p. 419.

49. Erdelyi, G., et al., *Determination of diffusion coefficients of Zn, Co and Ni in aluminium by a resistometric method.* Philosophical Magazine B, 1978. 38(5): p. 445-462.

50. Peterson, N. and S. Rothman, *Impurity diffusion in aluminum.* Physical Review B, 1970. 1(8): p. 3264.

51. Prabhu, T.R., *Effects of ageing time on the mechanical and conductivity properties for various round bar diameters of AA 2219 Al alloy.* Engineering Science Technology, an International Journal, 2017. 20(1): p. 133-142.

52. Raghavan, V., *Al-C-Co (Aluminum-Carbon-Cobalt).* Journal of Phase Equilibria Diffusion, 2008. 29(1): p. 46-48.

53. Wadhwa, A.S. and E.H.S. Dhaliwal, *A Textbook of Engineering Material and Metallurgy*. 2008: Firewall Media.

54. Wang, C., et al., *Phase alignment and crystal orientation of Al3Ni in Al–Ni alloy by imposition of a uniform high magnetic field.* Journal of Crystal Growth, 2008. 310(6): p. 1256-1263.

55. Marquis, E.A., D.N. Seidman, and D.C. Dunand, *Precipitation strengthening at ambient and elevated temperatures of heat-treatable Al (Sc) alloys [Acta Materialia 50 (16), pp. 4021–4035].* Acta Materialia, 2003. 51(1): p. 285.

56. Tabor, D., *The physical meaning of indentation and scratch hardness.* British Journal of Applied Physics, 1956. 7(5): p. 159.

57. Wang, Z., et al., *Effect of coherent L12 nanoprecipitates on the tensile behavior of a fcc-based high-entropy alloy.* Materials Science Engineering: A, 2017. 696: p. 503-510.

58. Meyers, M.A. and K.K. Chawla, *Mechanical metallurgy: principles and applications*. Vol. 761. 1984: Prentice-Hall Englewood Cliffs, NJ.

59. Gaillac, R., P. Pullumbi, and F.-X. Coudert, *ELATE: an open-source online application for analysis and visualization of elastic tensors.* Journal of Physics: Condensed Matter, 2016. 28(27): p. 275201.

60. Shi, D., et al., *First-principles studies of Al–Ni intermetallic compounds.* Journal of solid state chemistry, 2009. 182(10): p. 2664-2669.

61. Bi-Yu, W.N.a.T., *Structural, elastic and electronic properties of L12 aluminum phases from first principles calculation.* Acta Phys. Sin., 2009. 58: p. 230–234.

62. Fu, L., et al., *Mechanical properties of L12 type Al3X (X= Mg, Sc, Zr) from first-principles study.* physica status solidi, 2012. 249(8): p. 1510-1516.

63. Z. Wei, S.T., B. Wu, K. Bai, *First principles investigation of crystal lattice structure, thermodynamics and mechanical properties in ZnZrAl2 intermetallic compound.* Solid State Communications, 2016. 247: p. 82–87.

64. Ardell, A.J., *Ch 12: Intermetallics as precipitates and dispersoids in high-strength alloys*, in *Intermetallic compounds: principles and practice*, F.R. Westbrook JH, Editor. 1994, Chichester: John Wiley & Sons. p. 257.

65. H.J. Frost, M.F.A., *Deformation-mechanism maps: the plasticity and creep of metals and ceramics*. 1982: New York: Pergamon Press.

66. Makhlouf, Y.F.a.M.M., *The Al-Al3Ni Eutectic Reaction: Crystallography and Mechanism of Formation.* Metallurgical and Materials Transactions A, 2015. 46A: p. 3808–3812.

67. P.H.L. Souza, C.A.S.d.O., J.M.V. Quaresma, *Precipitation hardening in dilute Al-Zr alloys.* J Mater Res Technol. , 2018. 7(1): p. 66–72.

68. W. Lefebvre, e.a., *Tracking the path of dislocations across ordered Al3Zr nano-precipitates in three dimensions.* Scripta Materialia, 2014. 70: p. 43- 46.

69. R. Hyland, e.a., *Al (fcc): Al3Sc (L12) interphase boundary energy calculations.* Acta materialia, 1998. 46(10): p. 3667-3678.

70. X. Gao, J.W., X. Wu, R. Wang and Z. Jia, *Effects of Alloying Atoms on Antiphase Boundary Energy and Yield Stress Anomaly of L12 Intermetallics : First-Principles Study.* Crystals, 2018. 8: p. 96.

71. M.A. Phillips, B.M.C., and W.D. Nix, *A model for dislocation behavior during deformation of Al/Al3Sc (fcc/L12) metallic multilayers.* Acta Materialia, 2003. 51(11): p. 3157-3170.

72. Freeman, T.H.a.A.J., *Effect of antiphase boundaries on the electronic structure and bonding character of intermetallic systems: NiAl.* Physical Review B, 1991. 43: p. 8.

73. O. I. Gorbatov, e.a., *Effect of composition on antiphase boundary energy in Ni3Al based alloys: Ab initio calculations.* Physical Review B, 2016. 93: p. 224106.

74. C.B. Fuller, D.N.S.a.D.C.D., *Mechanical properties of Al(Sc,Zr) alloys at ambient and elevated temperatures.* Acta Materialia, 2003. 51: p. 4803–4814.

75. X. Sauvage, E.V.B., M. Yu.Murashkin, Y. Nasedkina, N.A. Enikeev, R.Z. Valiev, *Optimization of electrical conductivity and strength combination by structure design at the nanoscale in Al–Mg–Si alloys.* Acta Materialia, 2015. 98: p. 355-366.

76. A.K. Guptaa, D.J.L., S.A. Court, *Precipitation hardening in Al–Mg–Si alloys with and without excess Si.* Materials Science and Engineering: A, 2001. 316: p. 11-17.

77. Guo, Z. and W. Sha, *Quantification of precipitation hardening and evolution of precipitates.* Materials Transaction, 2002. 43(6): p. 1273-1282.

78. Desch, P., R. Schwarz, and P. Nash, *Formation of metastable L12 phases in Al3Zr and Al-12.5% X-25% Zr (X≡ Li, Cr, Fe, Ni, Cu).* Journal of the Less Common Metals, 1991. 168(1): p. 69-80.

79. Virk, I. and R. Varin, *Structure of as cast L12 compounds in Al3Zr—Base alloys containing Cu and Mn.* Scripta metallurgica et materialia, 1991. 25(1): p. 85-88.

80. Commission, I.E., *Thermal-resistant Aluminium Alloy Wire for Overhead Line Conductor IEC 62004*. 2007: IEC.

81. Knipling, K.E., D.N. Seidman, and D.C. Dunand, *Ambient-and high-temperature mechanical properties of isochronally aged Al–0.06 Sc, Al–0.06 Zr and Al–0.06 Sc–0.06 Zr (at.%) alloys.* Acta Materialia, 2011. 59(3): p. 943-954.

82. Souza, P.H.L., J.M.d.V. Quaresma, and C.A.S. Oliveira, *Precipitation Evolution and Modeling of Growth Kinetics of L12-structured Al3Zr Particles in Al-0.22 Zr and Al-0.32 Zr (wt.) Alloys Isothermally Aged.* Materials Research, 2017(AHEAD): p. 0-0.

83. Litynska, L., et al., *TEM and HREM study of Al3Zr precipitates in an Al-Mg-Si-Zr alloy.* Journal of Microscopy, 2006. 223(3): p. 182-184.

84. Tsau, C.-H. and Y.-C. Chen, *The coarsening of the precipitates in melt-spun Al–Ti–Zr ribbons.* Materials Chemistry Physics, 2002. 73(2-3): p. 111-117.

85. Skoko, Ž., S. Popović, and G. Štefanić, *Microstructure of Al-Zn and Zn-Al Alloys.* Croatica chemica acta, 2009. 82(2): p. 405-420.

86. Ardell, A., *Precipitation hardening.* Metallurgical Transactions A, 1985. 16(12): p. 2131-2165.

87. Zedalis, M. and M. Fine, *Precipitation and ostwald ripening in dilute AI Base-Zr-V alloys.* Metallurgical Transactions A, 1986. 17(12): p. 2187-2198.

88. Hu, C.M., et al., *Enhanced tensile plasticity in ultrafine-grained metallic composite fabricated by friction stir process.* Scripta Materialia, 2008. 59: p. 1163–1166.

Appendix A

A.1 VASP-DFT input files

A.1.1 INCAR

INCAR file contains the codes utilized for running each simulation. It is the central input file. The INCAR files used for this study were similar since all the alloys included Al and transition metals. Most of these parameters also have default values that were not necessary to change. The sample of a typical INCAR file used for the cluster and disperse alloy systems follows the format below:

```
SYSTEM = Al107Zn crystal
LPLANE = .TRUE. #Reduces the amount of communication needed
LSCALU = .FALSE.
NSIM = 4
NPAR = 4
LOPTICS = .TRUE. #VASP calculates the frequency dependent dielectric matrix
ISIF = 3        #Allows the cell and ions to fully relax
ISMEAR = 1      #Methfessel-Paxton scheme for partial occupancies
SIGMA = 0.2     #Smearing width in eV
PREC = high     #Precision high
EDIFF = 1E-06   #SCF convergence criteria
EDIFFG = -0.0001
LREAL = Auto    #Uses reciprocal projection operators
NSW  = 5        #Number of ionic steps
IBRION =  1     #RMM-DIIS algorithm for ion relaxation
ENCUT = 550     #Energy cut-off
NELMIN = 4
```

A.1.2 POSCAR

This file is used to develop the alloy crystal lattice geometry. Here the atom positions in direct (fractional) coordinates and lattice vectors are detailed.

```
Al107Zn
1.0
      12.0000000000        0.0000000000        0.0000000000
       0.0000000000       12.0000000000        0.0000000000
       0.0000000000        0.0000000000       12.0000000000
  Al   Zn
  107   1
Direct
    0.000000000        0.000000000        0.333333343
    0.000000000        0.000000000        0.666666687
    0.000000000        0.333333343        0.000000000
    0.000000000        0.333333343        0.333333343
    0.000000000        0.333333343        0.666666687
    0.000000000        0.666666687        0.000000000
    0.000000000        0.666666687        0.333333343
    0.000000000        0.666666687        0.666666687
    0.333333343        0.000000000        0.000000000
    0.333333343        0.000000000        0.333333343
    0.333333343        0.000000000        0.666666687
    0.333333343        0.333333343        0.000000000
    0.333333343        0.333333343        0.333333343
    0.333333343        0.333333343        0.666666687
    0.333333343        0.666666687        0.000000000
    0.333333343        0.666666687        0.333333343
```

0.333333343	0.666666687	0.666666687
0.666666687	0.000000000	0.000000000
0.666666687	0.000000000	0.333333343
0.666666687	0.333333343	0.000000000
0.666666687	0.333333343	0.666666687
0.666666687	0.666666687	0.000000000
0.666666687	0.666666687	0.333333343
0.666666687	0.000000000	0.666666687
0.166666672	0.000000000	0.166666672
0.166666672	0.000000000	0.500000000
0.166666672	0.000000000	0.833333313
0.166666672	0.333333343	0.166666672
0.166666672	0.333333343	0.500000000
0.166666672	0.333333343	0.833333313
0.166666672	0.666666687	0.166666672
0.166666672	0.666666687	0.500000000
0.166666672	0.666666687	0.833333313
0.500000000	0.000000000	0.166666672
0.500000000	0.000000000	0.500000000
0.500000000	0.000000000	0.833333313
0.500000000	0.333333343	0.166666672
0.500000000	0.333333343	0.500000000
0.500000000	0.333333343	0.833333313
0.500000000	0.666666687	0.166666672
0.500000000	0.666666687	0.500000000
0.500000000	0.666666687	0.833333313
0.833333313	0.000000000	0.166666672
0.833333313	0.000000000	0.500000000

0.833333313	0.000000000	0.833333313
0.833333313	0.333333343	0.166666672
0.833333313	0.333333343	0.500000000
0.833333313	0.333333343	0.833333313
0.833333313	0.666666687	0.166666672
0.833333313	0.666666687	0.500000000
0.833333313	0.666666687	0.833333313
0.166666672	0.166666672	0.000000000
0.166666672	0.166666672	0.333333343
0.166666672	0.166666672	0.666666687
0.166666672	0.500000000	0.000000000
0.166666672	0.500000000	0.333333343
0.166666672	0.500000000	0.666666687
0.166666672	0.833333313	0.000000000
0.166666672	0.833333313	0.333333343
0.166666672	0.833333313	0.666666687
0.500000000	0.166666672	0.000000000
0.500000000	0.166666672	0.333333343
0.500000000	0.166666672	0.666666687
0.500000000	0.500000000	0.000000000
0.500000000	0.500000000	0.333333343
0.500000000	0.500000000	0.666666687
0.500000000	0.833333313	0.000000000
0.500000000	0.833333313	0.333333343
0.500000000	0.833333313	0.666666687
0.833333313	0.166666672	0.000000000
0.833333313	0.166666672	0.333333343
0.833333313	0.166666672	0.666666687

0.833333313	0.500000000	0.000000000
0.833333313	0.500000000	0.333333343
0.833333313	0.500000000	0.666666687
0.833333313	0.833333313	0.000000000
0.833333313	0.833333313	0.333333343
0.000000000	0.166666672	0.166666672
0.000000000	0.166666672	0.500000000
0.000000000	0.166666672	0.833333313
0.000000000	0.500000000	0.166666672
0.000000000	0.500000000	0.500000000
0.000000000	0.500000000	0.833333313
0.000000000	0.833333313	0.166666672
0.000000000	0.833333313	0.500000000
0.000000000	0.833333313	0.833333313
0.333333343	0.166666672	0.166666672
0.333333343	0.166666672	0.500000000
0.333333343	0.166666672	0.833333313
0.333333343	0.500000000	0.166666672
0.333333343	0.500000000	0.500000000
0.333333343	0.500000000	0.833333313
0.333333343	0.833333313	0.166666672
0.333333343	0.833333313	0.500000000
0.333333343	0.833333313	0.833333313
0.666666687	0.166666672	0.166666672
0.666666687	0.166666672	0.500000000
0.666666687	0.166666672	0.833333313
0.666666687	0.500000000	0.166666672
0.666666687	0.500000000	0.500000000

0.666666687	0.500000000	0.833333313
0.666666687	0.833333313	0.166666672
0.666666687	0.833333313	0.500000000
0.666666687	0.833333313	0.833333313
0.833333313	0.833333313	0.666666687
0.666666687	0.666666687	0.666666687
0.666666687	0.333333343	0.333333343
0.000000000	0.000000000	0.000000000

A.1.3 POTCAR

It contains the pseudopotential for each atom present in a system used in the computation. If the number of atoms in an alloy system is more than one, their pseudopotentials POTCAR files were simply concatenated into one single file using BASH script. A typical pseudopotential file is too long to be included here. Several POTCAR files are available online for download. There are also various categories of POTCAR for each element. Therefore, it is important to first test each of them to see which category works best for the system. In this study most of the POTCAR files used were selected from PAW-PBE_52 category. The beginning section of a typical POTCAR file is detailed below for Al.

```
PAW Al_sv_GW 2Feb2008
   11.0000000000000
 parameters from PSCTR are:
   VRHFIN =Al: s2p1
   LEXCH  = PE
   EATOM  =  2216.7599 eV,  162.9273 Ry

   TITEL  = PAW Al_sv_GW 2Feb2008
   LULTRA =        F    use ultrasoft PP ?
   IUNSCR =        0    unscreen: 0-lin 1-nonlin 2-no
   RPACOR =    0.000    partial core radius
```

POMASS = 26.982; ZVAL = 11.000 mass and valenz

RCORE = 1.700 outmost cutoff radius

RWIGS = 2.480; RWIGS = 1.312 wigner-seitz radius (au A)

ENMAX = 411.109; ENMIN = 308.331 eV

ICORE = 3 local potential

LCOR = T correct aug charges

LPAW = T paw PP

EAUG = 707.732

RMAX = 1.734 core radius for proj-oper

RAUG = 1.300 factor for augmentation sphere

RDEP = 1.730 radius for radial grids

RDEPT = 1.600 core radius for aug-charge

Atomic configuration

9 entries

n	l	j	E	occ.
1	0	0.50	-1511.1048	2.0000
2	0	0.50	-108.1629	2.0000
2	0	0.50	-106.1254	0.0000
3	0	0.50	-7.7528	2.0000
2	1	1.50	-69.6402	6.0000
2	1	1.50	-68.0291	0.0000
3	1	1.50	-2.7121	1.0000
3	2	2.50	-2.7212	0.0000
4	3	2.50	-2.7212	0.0000

Description

l	E	TYP	RCUT	TYP	RCUT
0	-108.1629450	23	1.300		
0	-106.1254428	23	1.300		
0	-7.7528455	23	1.700		

```
   1    -69.6401625     23  1.600
   1    -68.0291300     23  1.600
   1     -2.7120682     23  1.700
   2     -5.4423304     23  1.700
   2     81.6349560     23  1.700
   3     13.6058260     23  1.700
  Error from kinetic energy argument (eV)
  NDATA  =     100
  STEP   =  20.000   1.050
 172.     171.     171.     170.     169.     168.     167.     166.
 164.     163.     162.     160.     158.     156.     154.     152.
 150.     147.     145.     141.     138.     135.     131.     128.
 125.     120.     115.     112.     107.     102.     96.7     91.6
 86.6     81.6     76.7     71.9     65.7     61.2     55.4     51.2
 45.9     41.0     36.3     32.0     28.1     24.5     21.2     17.5
 15.0     12.1     9.74     8.10     6.35     4.91     3.54     2.64
 1.94     1.31     0.859    0.548    0.342    0.210    0.132    0.829E-01
0.632E-01 0.539E-01 0.510E-01 0.494E-01 0.463E-01 0.419E-01 0.354E-01 0.283E-01
0.216E-01 0.160E-01 0.113E-01 0.845E-02 0.648E-02 0.536E-02 0.464E-02 0.415E-02
0.362E-02 0.307E-02 0.254E-02 0.203E-02 0.164E-02 0.137E-02 0.116E-02 0.964E-03
0.787E-03 0.628E-03 0.492E-03 0.411E-03 0.362E-03 0.335E-03 0.302E-03 0.253E-03
0.192E-03 0.144E-03 0.113E-03 0.104E-03
END of PSCTR-controll parameters
 local part
   109.604107337578
 0.54237223E+02  0.54226690E+02  0.54200652E+02  0.54157311E+02
0.54096753E+02
 0.54019091E+02  0.53924471E+02  0.53813066E+02  0.53685074E+02
0.53540717E+02
```

0.53380238E+02 0.53203905E+02 0.53012002E+02 0.52804836E+02
0.52582732E+02
0.52346036E+02 0.52095112E+02 0.51830343E+02 0.51552129E+02
0.51260887E+02
0.50957049E+02 0.50641058E+02 0.50313372E+02 0.49974454E+02
0.49624779E+02
0.49264823E+02 0.48895069E+02 0.48516002E+02 0.48128108E+02
0.47731871E+02
0.47327776E+02 0.46916306E+02 0.46497937E+02 0.46073144E+02
0.45642393E+02
0.45206143E+02 0.44764845E+02 0.44318939E+02 0.43868855E+02
0.43415011E+02
0.42957811E+02 0.42497645E+02 0.42034893E+02 0.41569915E+02
0.41103060E+02
0.40634661E+02 0.40165035E+02 0.39694484E+02 0.39223295E+02
0.38751738E+02
0.38280067E+02 0.37808522E+02 0.37337326E+02 0.36866687E+02
0.36396800E+02
0.35927842E+02 0.35459980E+02 0.34993367E+02 0.34528141E+02
0.34064431E+02
0.33602354E+02 0.33142017E+02 0.32683517E+02 0.32226942E+02
0.31772372E+02
0.31319879E+02 0.30869530E+02 0.30421384E+02 0.29975499E+02

A large part of the POTCAR file is not included.

A.1.4 KPOINTS

It contains the k-point coordinates and mesh size for creating the k-point grid. These k-points could be entered explicitly or the automatic k-mesh generation could be used. In this study the automatic k-mesh was used.

Automatic mesh

0 ! automatic generation scheme

Auto ! fully automatic

70 ! length (l)

A.2 VASP-DFT output files

There are many files the VAST-DFT outputs for a single simulation, though, only a few of the most important files are detailed in this study. They include the OSZICAR, CONTCAR and OUTCAR files.

A.2.1 CONTCAR

This file is very similar to the POSCAR file. The only difference is the CONTCAR file represents the final (lowest energy) crystal lattice geometry of the alloy system after all the atoms/ions and crystal cell have been relaxed. It contains the atomic positions of the last ionic step of the relaxation until convergence occurs. A typical CONTCAR file for Al unit cell is detailed below.

Al

1.00000000000000

4.0187845410749867 0.0000000000000000 -0.0000000000000000

0.0000000000000000 4.0187845410749867 0.0000000000000000

0.0000000000000000 0.0000000000000000 4.0187845410749867

Al

4

Direct

0.0000000000000000 0.0000000000000000 -0.0000000000000000

0.5000000000000000 -0.0000000000000000 0.5000000000000000

0.5000000000000000 0.5000000000000000 0.0000000000000000

0.0000000000000000 0.5000000000000000 0.5000000000000000

0.00000000E+00 0.00000000E+00 0.00000000E+00

0.00000000E+00 0.00000000E+00 0.00000000E+00

0.00000000E+00 0.00000000E+00 0.00000000E+00

0.00000000E+00 0.00000000E+00 0.00000000E+00

A.2.2 OSZICAR

This includes the free energy for each electronic step, where N is the number of electronic steps, E is the current free energy, dE is change in free energy between the last and current free energy. 5 F represents the final free energy after convergence occurs for the fifth ionic step . The last section of an OSZICAR file is detailed below.

N E dE d eps ncg rms rms(c)

DAV: 1 -0.401502795801E+03 0.17239E-02 -0.18031E-02 53672 0.255E+00 0.221E-01

DAV: 2 -0.401504383900E+03 -0.15881E-02 -0.17568E-02 47608 0.375E-01 0.127E-01

DAV: 3 -0.401504657332E+03 -0.27343E-03 -0.22635E-03 51000 0.237E-01 0.115E-01

DAV: 4 -0.401504698951E+03 -0.41619E-04 -0.39631E-04 52792 0.104E-01 0.978E-02

DAV: 5 -0.401504689634E+03 0.93170E-05 -0.65127E-05 49192 0.429E-02 0.100E-01

DAV: 6 -0.401504682709E+03 0.69251E-05 -0.16285E-05 38272 0.179E-02 0.102E-01

DAV: 7 -0.401504673349E+03 0.93598E-05 -0.19199E-06 18312 0.946E-03 0.981E-02

DAV: 8 -0.401504552759E+03 0.12059E-03 -0.22889E-06 18512 0.499E-02 0.375E-02

DAV: 9 -0.401504173158E+03 0.37960E-03 -0.71947E-05 46256 0.108E-01 0.246E-01

DAV: 10 -0.401504192861E+03 -0.19703E-04 -0.50227E-05 51176 0.304E-02
0.253E-01
DAV: 11 -0.401504198040E+03 -0.51791E-05 -0.37283E-06 20928 0.872E-03
0.249E-01
DAV: 12 -0.401504223205E+03 -0.25165E-04 -0.31809E-07 15280 0.662E-03
0.235E-01
DAV: 13 -0.401504308492E+03 -0.85286E-04 -0.49261E-07 15696 0.214E-02
0.195E-01
DAV: 14 -0.401504345387E+03 -0.36896E-04 -0.16512E-06 16544 0.442E-02
0.202E-01
DAV: 15 -0.401504332576E+03 0.12811E-04 -0.78803E-06 31408 0.515E-02
0.255E-01
DAV: 16 -0.401504382106E+03 -0.49530E-04 -0.15681E-05 44472 0.181E-02
0.236E-01
DAV: 17 -0.401504357514E+03 0.24592E-04 -0.21255E-06 17272 0.165E-02
0.240E-01
DAV: 18 -0.401504364701E+03 -0.71878E-05 -0.46060E-07 14976 0.124E-02
0.226E-01
DAV: 19 -0.401504481088E+03 -0.11639E-03 -0.29493E-05 46040 0.896E-02
0.733E-02
DAV: 20 -0.401504522386E+03 -0.41299E-04 -0.24834E-05 41808 0.915E-02
0.174E-02
DAV: 21 -0.401504526024E+03 -0.36376E-05 -0.19927E-05 40072 0.318E-02
0.138E-02
DAV: 22 -0.401504521701E+03 0.43235E-05 -0.26492E-06 17768 0.866E-03
0.158E-02
DAV: 23 -0.401504531226E+03 -0.95253E-05 -0.55396E-07 15008 0.114E-02
0.137E-02
DAV: 24 -0.401504529763E+03 0.14633E-05 -0.62587E-07 14976 0.316E-03
0.140E-02

DAV: 25 -0.401504533246E+03 -0.34831E-05 -0.20371E-07 14976 0.901E-03 0.141E-02

DAV: 26 -0.401504540646E+03 -0.74006E-05 -0.23519E-07 14928 0.371E-02 0.172E-02

DAV: 27 -0.401504576367E+03 -0.35721E-04 -0.30987E-06 20976 0.109E-01 0.274E-02

DAV: 28 -0.401504560871E+03 0.15496E-04 -0.62616E-07 15080 0.268E-02 0.134E-02

DAV: 29 -0.401504557892E+03 0.29794E-05 -0.77154E-07 15064 0.555E-03 0.103E-02

DAV: 30 -0.401504557468E+03 0.42396E-06 -0.37330E-07 14968 0.336E-03

5 F= -.40150456E+03 E0= -.40150361E+03 d E =-.369697E-04

imaginary and real dielectric function

A.2.3 OUTCAR

This is the most important output file in this study, because it contains a detail of all the computational output. A typical OUTCAR file is too long to be included in this paper, however a few important sections are detailed below.

COMPUTATION PARAMETERS SUMMARY

vasp.5.3.5 31Mar14 (build May 10 2014 09:33:21) complex

executed on HPConROCKSatMTU date 2015.10.23 10:58:00

running on 32 total cores

distrk: each k-point on 32 cores, 1 groups

distr: one band on NCORES_PER_BAND= 8 cores, 4 groups

```
 INCAR:
 POTCAR:    PAW Al_sv_GW 2Feb2008
 POTCAR:    PAW Zn_sv_GW 01Dec2010
 POTCAR:    PAW Al_sv_GW 2Feb2008
   VRHFIN =Al: s2p1
   LEXCH  = PE
   EATOM  =  2216.7599 eV,  162.9273 Ry

   TITEL  = PAW Al_sv_GW 2Feb2008
   LULTRA =       F    use ultrasoft PP ?
   IUNSCR =       0    unscreen: 0-lin 1-nonlin 2-no
   RPACOR =    0.000    partial core radius
   POMASS =   26.982; ZVAL   =   11.000    mass and valenz
   RCORE  =    1.700    outmost cutoff radius
   RWIGS  =    2.480; RWIGS  =    1.312    wigner-seitz radius (au A)
   ENMAX  =  411.109; ENMIN  =  308.331 eV
   ICORE  =       3    local potential
   LCOR   =       T    correct aug charges
   LPAW   =       T    paw PP
   EAUG   =  707.732
   RMAX   =    1.734    core radius for proj-oper
   RAUG   =    1.300    factor for augmentation sphere
   RDEP   =    1.730    radius for radial grids
   RDEPT  =    1.600    core radius for aug-charge

 VOLUME and BASIS-vectors are now :
 -----------------------------------------------------------------------------
  energy-cutoff  :      550.00
  volume of cell :     1753.55
     direct lattice vectors                 reciprocal lattice vectors
```

12.058864943 -0.000000000 -0.000000000 0.082926544 0.000000000 0.000000000

-0.000000000 12.058864943 -0.000000000 0.000000000 0.082926544 -0.000000000

-0.000000000 0.000000000 12.058864943 0.000000000 0.000000000 0.082926544

length of vectors

12.058864943 12.058864943 12.058864943 0.082926544 0.082926544 0.082926544

ELECTRICAL CONDUCTIVITY

electrical conductivity sigma (Mega S m-1) (frequency dependency in vasprun.xml)

0.177 0.000 0.000

0.000 0.177 0.000

0.000 0.000 0.177

VASP COMPUTATION COST, TIME AND MEMORY

OPTICS: CPU time 202.38: Wall time 232.70

4ORBIT: CPU time 0.00: Wall time 0.00

total amount of memory used by VASP on root node 469708. kBytes

==========

base : 30000. kBytes
nonlr-proj: 11669. kBytes
fftplans : 18522. kBytes
grid : 24772. kBytes
one-center: 1129. kBytes
wavefun : 383616. kBytes

General timing and accounting informations for this job:
==========

Total CPU time used (sec): 68395.719
User time (sec): 65783.439
System time (sec): 2612.280
Elapsed time (sec): 94499.464

Maximum memory used (kb): 1594244.
Average memory used (kb): 0.

Minor page faults: 128220
Major page faults: 5
Voluntary context switches: 275599073

Appendix B

B.1 Automated bash submission (ABS) scripts

This script was written to dynamically submit multiple simulation files with one code. It checks all the folders containing the input files to see if the POTCAR files requires concatenation and performs concatenation before submitting using the qgenscript. It is useful for single, binary and ternary alloy systems; it can be expanded to access more than ternary systems. For this code to function properly a few guidelines must be followed:

- For multiple element alloy system, label the non-concatenated POTCAR files of each element as AlPOTCAR and POTCARTM (replace TM with the specific element e.g Zn, Zr, Ni).
- Each alloy system folder must include all input files with the appropriately.
- The qgenscript and this ABS script must be in the same folder containing all alloy system folders.

The ABS script is detailed below

```
#!/bin/bash

 # Variable for number of files in folder
 # imax is the max number of directories
 # EDITABLE

 imax=0

 # Arrange all directories into an array
 shopt -s nullglob
 array=(*)
```

```
shopt -u nullglob

#echo ${array[i]}
#echo ${#array[@]}

# Start loop all through all directories present
# EDITABLE
for (( i=0; i<=imax; i++ ));
do

 # Assign current array element to a
 a=( "${array[i]}" )
 echo $a

 # Open current working folder path and copy vasp_535p.sh into it
 # Enter into current working folder
 # EDITABLE
 cp vasp_535p.sh /home/otfadayo/research/$a
 cd /home/otfadayo/research/$a

 # if to check if POTCAR files need concatenation into one file then removes pieces
 # if POTCAR file existing is already concartenated it submits
 if [ -f AlPOTCAR ] && [ -f POTCARZn ] && [ -f POTCARTM ]
 then
  cat AlPOTCAR POTCARZn POTCARTM > POTCAR
  rm -rf AlPOTCAR POTCARZn POTCARTM
  qsub vasp_535p.sh
 elif [ -f AlPOTCAR ] && [ -f POTCARTM ]
 then
  cat AlPOTCAR POTCARTM > POTCAR
```

```
    rm -rf AlPOTCAR POTCARTM
    qsub vasp_535p.sh
  else
    qsub vasp_535p.sh
  fi
cd ..
done
```

B.2 VASP submission scripts

Submission scripts for VASP simulations are generated using qgenscript, an in-house utility developed at and unique to Michigan Tech University. Its typical submission script is detailed below. Though, technical aspects of the scripts can occasionally change to reflect the changes in queuing system configuration. As such, users are strongly encouraged to not edit the script and generate a new one for each simulation. Furthermore, users can consult the HPC administrator to generate such scripts in bulk, whenever necessary to save time.

```
#! /bin/bash
#
#$ -cwd
#$ -j y
#$ -S /bin/bash
# No notification
#$ -m abes
#$ -pe mpich_unstaged 32
#$ -q long.q
#$ -hard -l mem_free=2G
#$ -hard -l vasp_lic=.0312500000
#$ -notify
```

```
# Necessary variables
source /share/apps/bin/bashrc
module load intel/2013.0.028
module load vasp/5.3.3
module list

# Input/Output files
export INPUT_FOLDER="${PWD}"
export ARRAY_JOB=""

# Run VASP 5.3.3 (standard; parallel)
mpirun -n ${NSLOTS} -machine ${TMP}/machines ${VASP}/vasp

# Unload modules
module unload vasp/5.3.3
module unload intel/2013.0.028
module list
```

B.3 Computational cost

Below is a summary of the computation cost for the various project types worked on.

Project type:	Binary $Al_{107}TM$
Number of ionic steps (NSW)	5
Number of simulations:	100
Average total cores per simulation:	32
NPAR	4
Average CPU time per simulation (s):	261
Average wall time (s):	276

Project type:	Cluster ternary $Al_{106}ZnTM$
Number of ionic steps (NSW)	5
Number of simulations:	25
Average total cores per simulation:	64
NPAR	4
Average CPU time per simulation (s):	553
Average wall time (s):	556

Project type:	Disperse ternary $Al_{106}ZnTM$
Number of ionic steps (NSW)	5
Number of simulations:	25
Average total cores per simulation:	64
NPAR	4
Average CPU time per simulation (s):	765
Average wall time (s):	768

Appendix C: Reprint copyright permission

Copyright Clearance Center RightsLink®

Home | Create Account | Help

Title: Investigation of Al-Zn-Zr and Al-Zn-Ni alloys for high electrical conductivity and strength application

Author: Oladeji Fadayomi,Rachel Clark,Violet Thole,Paul G. Sanders,Gregory M. Odegard

Publication: Materials Science and Engineering: A

Publisher: Elsevier

Date: 16 January 2019

© 2018 Elsevier B.V. All rights reserved.

LOGIN

If you're a copyright.com user, you can login to RightsLink using your copyright.com credentials.

Already a RightsLink user or want to learn more?

Please note that, as the author of this Elsevier article, you retain the right to include it in a thesis or dissertation, provided it is not published commercially. Permission is not required, but please ensure that you reference the journal as the original source. For more information on this and on your other retained rights, please visit: https://www.elsevier.com/about/our-business/policies/copyright#Author-rights

BACK | CLOSE WINDOW

Copyright © 2018 Copyright Clearance Center, Inc. All Rights Reserved. Privacy statement. Terms and Conditions.
Comments? We would like to hear from you. E-mail us at customercare@copyright.com